Probabilistic Analysis of the Material and Shape Properties for Human Liver

Yuan-Chiao Lu

Dissertation submitted to the faculty of the Virginia Polytechnic Institute and State University in partial fulfillment of the requirements for the degree of

Doctor of Philosophy
In
Biomedical Engineering

Costin D. Untaroiu, Chair
Philippe D. Beillas
F. Scott Gayzik
Warren N. Hardy
Andrew R. Kemper

July 2nd, 2014
Blacksburg, Virginia

Keywords: Injury Biomechanics, Human Liver, Statistical Shape Analysis, Tensile Testing, Ogden Material Model, Probabilistic Analysis, Finite Element Analysis

Probabilistic Analysis of the Material and Shape Properties for Human Liver

Yuan-Chiao Lu

ABSTRACT

Realistic assessments of liver injury risk for the entire occupant population require incorporating inter-subject variations into numerical human models. The main objective of this study was to quantify the variations in shape and material properties of the human liver. Statistical shape analysis was applied to analyze the geometrical variation using a surface set of 15 adult human livers recorded in an occupant posture. Principal component analysis was then utilized to obtain the modes of variation, the mean model, and a set of 95% statistical boundary shape models. Specimen-specific finite element (FE) models were employed to quantify material and failure properties of human liver parenchyma. The mean material model parameters were then determined, and a stochastic optimization approach was utilized to determine the standard deviations of the material model parameters. The distributions of the material parameters were used to develop probabilistic FE models of the liver implemented in THUMS human FE model to simulate oblique impact tests under three impact speeds. In addition, the influence of organ preservation on the biomechanical responses of animal livers was investigated using indentation and tensile tests.

Results showed that the first five modes of the human liver shape models accounted for more than 70% of the overall anatomical variations. The Ogden material model with two parameters showed a good fit to experimental tensile data before failure. Significant changes of the biomechanical responses of liver parenchyma were found after cooling or freezing storage. The force-deflection responses of THUMS model with probabilistic liver material models were within the test corridors obtained from cadaveric tests. Significant differences were observed in the maximum and minimum principal Green-Lagrangian strain values recorded in the THUMS liver model with the default and updated average material properties. The results from this study could help in the development of more biofidelic human models, which may provide a better understanding of injury mechanisms of the liver during automobile collisions.

Acknowledgements

I would never have been able to finish my dissertation without the guidance of my committee members, help from friends, and support from my family and wife. I would like to express my deepest gratitude to my advisor, Dr. Costin Untaroiu, for his excellent guidance, caring, patience, and providing me with an excellent atmosphere and financial support for doing research. I would like to thank Dr. Andrew Kemper, who let me experience the research of tensile testing on abdominal tissues and instructed me to prepare the coupon specimens of the tissues. I would also like to thank Dr. Philippe Beillas and Dr. F. Scott Gayzik for guiding my research for the past several years and helping me to develop my background in computer simulations. I would like to give special thanks to Dr. Warren Hardy for his valuable comments on my dissertation work and his financial support for my research during my last semester in the Ph.D. program. Finally, I am indebted to all the members of the Virginia Tech Center for Injury Biomechanics for sharing their knowledge and expertise with me.

Table of Contents

Chapter 1 1
Introduction 1
1.1. Background 1
1.2. Project Aims 3
Chapter 2 4
Statistical Shape Analysis of Human Liver 4
2.1. Introduction 4
2.2. Methodology 6
2.2.1. Image Acquisition 6
2.2.2. Registration 8
2.2.3. Correspondence 8
2.2.3.1. “He” Approach 10
2.2.3.2. “Giessen” Approach 11
2.2.4. Refining the Target Landmarks by Iterative TPS 11
2.2.5. Principal Component Analysis 12
2.2.6. Distribution of Shapes 13
2.2.7. Three Measures for Shape-Correspondence Evaluation 13
2.2.7.1. Model Compactness 14
2.2.7.2. Model Generalization 14
2.2.7.3. Model Specificity 14
2.2.8. Statistical Boundary Shape Models 14
2.3. Results 17
2.4. Discussion 22
Chapter 3 27
Effect of Preservation on Material Properties of Liver Parenchyma 27
3.1. Introduction 27
3.2. Methodology 28
3.2.1. Indentation Testing on Porcine Livers 28
3.2.1.1. Specimen Preparation and Testing Procedure 28

3.2.1.2. Identification of Material Properties 29
3.2.1.3. Statistical Analysis 31
3.2.2. Tensile Testing on Bovine Livers 31
3.2.2.1. Specimen Preparation and Testing Procedure 31
3.2.2.2. Data Analysis 36
3.2.2.3. Identification of Material Properties 38
3.2.2.4. Statistical Analysis 39
3.3. Results 39
3.3.1. Indentation Testing on Porcine Livers 39
3.3.2. Tensile Testing on Bovine Livers 41
3.4. Discussion 45
Chapter 4 51
Material Model Identification of Human Liver Parenchyma under Tensile Loading 51
4.1. Introduction 51
4.2. Methodology 52
4.2.1. Specimen Preparation and Testing Procedure 52
4.2.2. Identification of Material Properties 53
4.2.2.1. Marker Data Analysis 54
4.2.2.2. Specimen-specific FE Analysis 55
4.2.3. Stress-Strain Curve Average and Variation Corridor 57
4.2.4. Stochastic Optimization 57
4.3. Results 58
4.3.1. Marker Data Analysis 58
4.3.2. Specimen-specific FE Analysis 62
4.3.3 Stochastic Optimization 67
4.4. Discussion 68
Chapter 5 73
Probabilistic Finite Element Models of Human Liver 73
5.1. Introduction 73
5.2. Methodology 77

5.2.1. Liver Parenchyma Compressive Property 77
5.2.2. Liver Capsule Tensile Property 78
5.2.3. Average and Probabilistic Liver Material Models 79
5.2.4. Full-Body Behavior 80
5.3. Results 82
5.3.1. Liver Parenchyma Compressive Property 82
5.3.2. Liver Capsule Tensile Property 83
5.3.3. Average and Probabilistic Liver Material Models 84
5.3.4. Full-Body Behavior 89
5.3.5. Probabilistic Liver Material Models 92
5.3.6. Rib Injuries 96
5.3.7. Liver Injuries 97
5.4. Discussion 100
Chapter 6 104
Conclusion 104
6.1. Contribution 104
6.2. Future Work 105
Reference 107

List of Figures

Chapter 1 1

Introduction 1

Figure 1.1. Illustration of human liver. (a) The location of the human liver in a standing posture; (b) A liver organ placed on a flat table. 2

Chapter 2 4

Statistical Shape Analysis of Human Liver 4

Figure 2.1. Processes of statistical shape analysis on human livers. 6

Figure 2.2. Subject seated positions: (a) “Lyon” dataset; (b) “Wake” dataset. 8

Figure 2.3. An illustration of constructing template landmarks from point clouds (2D case). 9

Figure 2.4. Illustrations of surface normals: (a) A typical surface normal; (b) Each point on the surface has a coordinate (3-dimension) and a surface normal (3-dimension). 11

Figure 2.5. An illustration of the set of 95% statistical boundary models developed using three pre-selected modes (q=3) (Lu et al., 2013). 16

Figure 2.6. Quantitative evaluation (compactness, generalization, and specificity) on human liver data (Error bar: 1 SD) between three reduced numbers of surface points. A better model is a model with lower values of compactness, generalization and specify for a certain number of principal modes. 18

Figure 2.7. Quantitative evaluation (compactness, generalization, and specificity) on human liver data (Error bar: 1 SD) between “He” approach and “Giessen” approach. ... 18

Figure 2.8. Percentage of variation contributed by each mode for the human liver statistical shape model. 19

Figure 2.9. The first five modes of variation of human livers. P: Posterior view; S: Superior view; L: Lateral view; M: Medial view. 20

Figure 2.10. Distribution of principal component scores of the first five modes of human liver. p represents p-value resulting from a Kolmogorov–Smirnoff test on the similarity between standardized principal component scores and a standard normal distribution. p-values>0.05 represent normally distributed shape parameters. 21

Figure 2.11. Four selected boundary models of human liver, developed using the first five principal component modes: (a) Boundary model #1; (b) Boundary model #2; (c) Boundary model #3; (d) Boundary model #4. 22

Figure 2.12. Comparison of the liver volumes between current and previous studies. Error bar: 1SD. 23

Chapter 3 27

Effect of Preservation on Material Properties of Liver Parenchyma 27

Figure 3.1. a) Overall test procedure. b) The indentation location of each specimen. c) Schematic illustration of the custom-built indentation-testing device used for experiments in the current study. 29

Figure 3.2. Overall procedure for bovine liver tensile testing. 32

Figure 3.3. Specimen slicing methodology (fresh liver). 33

Figure 3.4. Specimen stamping methodology (fresh liver). 33

Figure 3.5. Specimen size. 34

Figure 3.6. Experimental setup (fresh liver). 35

Figure 3.7. High-speed video stills of a typical uniaxial tensile test (Fresh, Rate 2: 0.1 s^{-1}). 35

Figure 3.8. An illustration of the local and global models for the stretch ratio calculation. 36

Figure 3.9. An illustration of the development approach of the elliptical corridor. SD: standard deviation. 38

Figure 3.10. Examples of curve fitting with QLV model. 40

Figure 3.11. (a) Average $Pe(h)$ for the cooling and freezing storages; (b) Average $G(t)$ for the cooling and freezing storages. Error bars represent ±1 SD. 40

Figure 3.12. An illustration of a typical experimental force-time curve (Rate 1) recorded on a liver specimen during tensile testing and its fitted curve using 5^{th} degree polynomial. 42

Figure 3.13. Characteristic averages and elliptical corridors of local model for a) 0.01 s^{-1} b) 0.1 s^{-1} c) 1 s^{-1} strain rates and of global model for d) 0.01 s^{-1} e) 0.1 s^{-1} f) 1 s^{-1} strain rates. 42

Figure 3.14. Failure stain and failure stress of the fresh and preserved tissues at three loading rates. 43

Figure 3.15. Illustrations of the time histories of reaction force of Ogden material model fitting for local and global models: (a) 0.01 s^{-1}; b) 0.1 s^{-1}; c) 1.0 s^{-1} strain rates. 45

Figure 3.16. Comparison of the shear modulus ratios with published studies for fresh porcine livers. 46

Chapter 4 51
Material Model Identification of Human Liver Parenchyma under Tensile Loading 51
Figure 4.1. Schematic of material identification process. 54
Figure 4.2. Illustration of the specimen-specific FE model: (a) mesh topology; (b) intermediate FE model (1,550 elements); (c) final FE model (360 elements) with boundary conditions. 56
Figure 4.3. Schematic diagram of the development of the stochastic material model. 58
Figure 4.4. High-speed video stills of a typical uniaxial tensile test (Rate 2: 0.1 s^{-1}). 59
Figure 4.5. Stress vs. strain curves from marker data analysis (a) Rate 1: 0.01 s^{-1}; (b) Rate 2: 0.1 s^{-1}; (c) Rate 3: 1.0 s^{-1}; (d) Rate 4: 10.0 s^{-1}. The last digit of each specimen ID is the donor subject ID. 59
Figure 4.6. Characteristic averages and variation corridors by rates based on the marker data analysis. 60
Figure 4.7. Comparisons of failure properties between current study, Kemper's study [2], and Lu's study [5]. (a) Failure Green-Lagrangian strain; (b) Failure 2nd Piola-Kirchhoff stress. 61
Figure 4.8. The distribution of Green-Lagrangian strain before failure for typical samples at high loading rate tensile tests. FE model with FE-based optimized material model parameters (a) Rate 4 (specimen L4_02_1); (b) Rate 3 (specimen L3_02_1). Red boxes represent the locations of boundary conditions. 63
Figure 4.9. Stress vs. strain curves from FE-based optimization analysis (a) Rate 1: 0.01 s^{-1}; (b) Rate 2: 0.1 s^{-1}; (c) Rate 3: 1.0 s^{-1}; (d) Rate 4: 10 s^{-1}. The last digit of each specimen ID is the donor subject ID. 64
Figure 4.10. Characteristic averages and variation corridors by rates based on the Ogden material models from specimen-specific FE simulations. 65
Figure 4.11. Comparisons of characteristic averages and variation corridors by rates between marker data and FE-based data (a) Rate 1: 0.01 s^{-1}; (b) Rate 2: 0.1 s^{-1}; (c) Rate 3: 1.0 s^{-1}; (d) Rate 4: 10.0 s^{-1}. 67
Figure 4.12. Stochastic optimization: comparisons between test and simulation corridors (a) Rate 1; (b) Rate 2; (c) Rate 3; (d) Rate 4. 68
Figure 4.13. A comparison between local response (tear site and gage length) and global response of a typical example (Rate 2: 0.1 s^{-1}). (a) Definitions of local and global; (b) Stress-strain curves measured at the three locations. 70
Chapter 5 73
Probabilistic Finite Element Models of Human Liver 73

Figure 5.1. Illustrations of (a) deterministic analysis and (b) probabilistic analysis. 73

Figure 5.2. The structures surrounding the liver model in THUMS. (a) and (b): anterior view; (c) and (d): posterior view. 75

Figure 5.3. The force-displacement curve defined in the material model (MAT_181) of liver parenchyma in the THUMS AM50 Version4. 76

Figure 5.4. Lateral abdominal impact testing setup [3, 4]. 77

Figure 5.5. Lateral abdominal impact simulation in THUMS. 81

Figure 5.6. Stochastic optimization: comparison between test and simulation corridors for liver parenchyma compression testing (a) Rate 1; (b) Rate 2; (c) Rate 3; (d) Rate 4. 83

Figure 5.7. Stochastic optimization: comparison between test and simulation corridors for liver capsule tensile testing. 84

Figure 5.8. The average material model for human liver: (a) Capsule; (b) Parenchyma. 84

Figure 5.9. Tensile and compressive force-displacement input curves for the average and probabilistic human liver parenchyma material models used in THUMS oblique impact simulations: (a) Rate 1; (b) Rate 2; (c) Rate 3; (d) Rate 4. 88

Figure 5.10. Tensile force vs. displacement input curves for the average and probabilistic human liver capsule material models used in THUMS oblique impact simulations. 89

Figure 5.11. THUMS behavior at the impact speed of 4.79 m/s. 89

Figure 5.12. THUMS behavior at the impact speed of 6.83 m/s. 90

Figure 5.13. THUMS behavior at the impact speed of 9.40 m/s. 90

Figure 5.14. Comparisons between THUMS default and updated average liver materials in terms of force-deflection and force-time responses for lateral abdomen impacts at three test speeds. (a) and (b): 4.79 m/s; (c) and (d): 6.83 m/s; (e) and (f): 9.40 m/s. 91

Figure 5.15. Comparisons between THUMS default and updated average liver materials in terms of maximum tensile and compressive strains for lateral abdomen impacts at three test speeds. (a) Liver capsule; (b) and (c) Liver parenchyma. 92

Figure 5.16. Force-deflection and force-time responses of 30 probabilistic THUMS simulations for lateral abdomen impacts at three test speeds. Each speed includes 30 simulations corresponding to 30 probabilistic liver materials. (a) and (b): 4.79 m/s; (c) and (d): 6.83 m/s; (e) and (f): 9.40 m/s. 94

Figure 5.17. The distributions of (a) the peak force, (b) the time of peak force, and (c) the absorbed energy determined from the 30 THUMS oblique impact simulations. The maximum values of peak force, time of peak force, and energy absorbed were fitted with 2nd degree polynomial (red dot curves). Error bar: 1 SD. 95

Figure 5.18. Comparisons between three test speeds in terms of (a) maximum tensile strain and (b) maximum compressive strain for oblique abdomen impacts for the 30 probabilistic THUMS simulations. Error bar: 1 SD. Red line: failure strain of the updated average material model. 96

Figure 5.19. Location of rib fractures. (a) 4.79 m/s; (b) 6.83 m/s; (c) 9.40 m/s. 96

Figure 5.20. Number of rib fractures. 97

Figure 5.21. Posterior view of the contour maps of 1st principal Green-Lagrangian strain ("tensile strain") in liver capsule: (a) 4.79 m/s; (b) 6.83 m/s; (c) 9.40 m/s. Red circle: the location of gallbladder. 98

Figure 5.22. Posterior view of the contour maps of 1st principal Green-Lagrangian strain ("tensile strain") in liver parenchyma: (a) 4.79 m/s; (b) 6.83 m/s; (c) 9.40 m/s. Red circle: the location of gallbladder. 99

Figure 5.23. Posterior view of the contour maps of 3rd principal Green-Lagrangian strain in liver parenchyma: (a) 4.79 m/s; (b) 6.83 m/s; (c) 9.40 m/s. Red circle: the location of gallbladder..... 100

Figure 5.24. The maximum tensile stress, maximum compressive stress, and maximum shear stress of the liver capsule and liver parenchyma for the three testing speeds (4.79 m/s, 6.83 m/s, and 9.40 m/s). 102

List of Tables

Chapter 2 4

Statistical Shape Analysis of Human Liver 4

Table 2.1. Demographic data of subjects. 7

Chapter 3 27

Effect of Preservation on Material Properties of Liver Parenchyma 27

Table 3.1. Data acquisition and video sampling rates by loading rate. 35

Table 3.2. Identified parameters of QLV material model (fresh vs. preserved tissues). The reported values are average±1 SD. 41

Table 3.3. The comparison of fresh and preserved tissues for cooling and freezing storages using the paired two-sample t-test. Each cell represents the average of differences between fresh and preserved tissues of $G\infty$ and $\mu 0$ and its corresponding p-value in the parentheses. 41

Table 3.4. Statistical comparison (p-values from Mann-Whitney U-Test) of failure strain between preservation times. 44

Table 3.5. Statistical comparison (p-values from Mann-Whitney U-Test) of failure stress between preservation times. 44

Table 3.6. Statistical comparison (p-values from Mann-Whitney U-Test) of failure strain between rates. 44

Table 3.7. Statistical comparison (p-values from Mann-Whitney U-Test) of failure stress between rates. 44

Table 3.8. The Ogden material model parameters of average stress-strain models for the three loading rates and preservation methods. 45

Table 3.9. Comparison of the freezing effect on liver tissues between studies. 48

Chapter 4 51

Material Model Identification of Human Liver Parenchyma under Tensile Loading 51

Table 4.1. Subject information 52

Table 4.2. Data acquisition and video sampling rates by loading rate. 53

Table 4.3. Averages and standard deviations by loading rate 60

Table 4.4. Two-way ANOVA for testing the effects of strain rates and donors on the mean of the failure strain and failure stress. Bold: p-value<0.05. 61

Table 4.5. Ogden material model parameters. 62

Table 4.6. Averages and standard deviations by loading rate. 66
Table 4.7. Two-way ANOVA for testing the effects of strain rates and donors on the mean of the failure strain and failure stress. Bold: p-value<0.05. 66
Table 4.8. Stochastic optimization of Ogden material parameters and failure strain by strain rate. 68
Chapter 5 73
Probabilistic Finite Element Models of Human Liver 73
Table 5.1. Material models and element information for the default liver capsule and parenchyma in the THUMS AM50 Version4. 75
Table 5.2. List of simulation cases. 81
Table 5.3. Stochastic optimization of polynomial parameters by loading rate for liver compression testing. Unit for all "P" parameters: MPa. 82
Table 5.4. Stochastic optimization of Ogden material parameters and failure strain for liver capsule tensile testing. 83
Table 5.5. Scaling factors for probabilistic human liver parenchyma tensile properties used in THUMS oblique impact simulations. 85
Table 5.6. Scaling factors for probabilistic human liver parenchyma compressive properties used in THUMS oblique impact simulations. 86
Table 5.7. Scaling factors for probabilistic human liver capsule tensile properties used in THUMS oblique impact simulations. 87

Chapter 1

Introduction

1.1. Background

Abdominal injuries caused by traffic accidents have severe consequences and are major causes of death in the United States [11-13]. According to the National Automotive Sampling System (NASS) datasets, approximately 19,000 adult occupants sustain AIS 2+ abdominal injuries each year [14]. Even though the abdominal organs, such as liver, spleen, and kidney, occupy a large relatively protected space in the human abdomen, these organs are the most commonly injured intra-abdominal organs in severe traffic accidents [11, 15, 16]. Abdominal injuries have severe consequences [11-13], and motor vehicle crashes are the leading cause of blunt abdominal trauma in children [17].

Improvements in automotive occupant safety have reduced the frontal fatality rate per mile of travel in USA about 2.6 times from 1979 to 2007 [18]. The novel designs of airbags and seat belt have largely contributed to the safety improvement. However, recent statistical studies of fatal injuries [19] show an increase in the ratios of abdominal injuries to head and thorax injuries of 9.6 and 5 times, respectively in newer cars relative to older cars. Therefore, the protection of abdomen in frontal crashes has recently attracted increased attention in the automotive safety community.

The liver is one of the most frequently injured abdominal organs in frontal vehicle crashes [16] (Fig. 1.1). The right lower rib cage covers a greater portion of the liver in the anterior region, but its downward displacement during the inhalation reduces its protection [20]. Capsule laceration and parenchyma damage are common liver injuries and can be severe [21]. The liver regulates most chemical levels in the blood making it essential to life, so its injuries due to blunt trauma have higher morbidity and mortality rates than other abdominal organs [22].

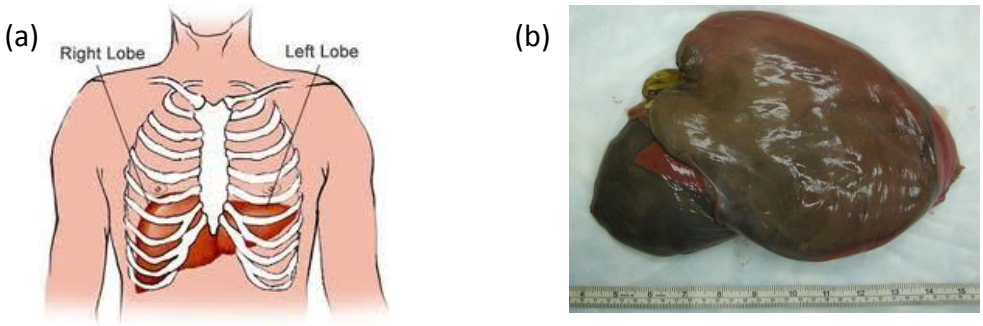

Figure 1.1. Illustration of human liver. (a) The location of the human liver in a standing posture; (b) A liver organ placed on a flat table.

A better understanding of the mechanisms of blunt liver trauma during the traffic accidents may help safety engineers optimize the restraint systems in order to reduce the occurrence of liver injuries. Several injury mechanisms of blunt liver trauma, such as crush, deceleration, and acceleration mechanisms [23], have been proposed in the medical literature based on the cause of injury, assumed direction and site of the blunt force, and medical images of the injured subjects [23-25]. While valuable for the management of major blunt liver injuries by emergency surgeons, these injury mechanisms should be validated by experimental and/or computational tests. Recently, high-speed biplane x-ray was used to investigate relative kinematics of the thoraco-abdominal organs in response to blunt loading [25]. However, the simplified loading conditions and limited field of view in the x-ray images during impacts makes a complete understanding of injury mechanisms challenging. With the rapid increase in computational power, a higher use of numerical models for vehicle safety research is observed. The human finite element (FE) models are currently the most sophisticated human numerical models, due to their ability to calculate detailed stress/strain distributions inside the model that consequently could be correlated with the risk of injury [26-31]. However, the majority of current human models was developed based on the anthropometry of a 50^{th} percentile male and has assigned material models which lack realistic biological tissue properties (e.g. strain-rate independent). Therefore, to better understand the injuries observed in the field we believed that new modeling approaches are necessary to take into account the variability of subjects in terms of anthropometries and material properties.

Biological systems, such as abdominal organs, contain inherent variability in geometry, and material properties. The combined effects of these differences along with the uncertainty associated with the loading conditions in the input variables could dramatically affect the system response. Probabilistic analyses consider the uncertainties of the input variables [32], so each variable is typically represented as a distribution, and a distribution of performance is predicted as output. In contrast, particular values are chosen for each input variable in deterministic studies, and the outputs are provided as certain numerical values, which cannot provide information about the effect of system uncertainties. Probabilistic analyses are widely used in many areas, such as aeronautical [33, 34], automotive [35], orthopedic studies [32, 36-41]. However, due to high computational cost, simplified FE models [36] or idealized cylindrical geometry [38] are commonly used in these studies. A probabilistic analysis to predict the maximum stress distribution on a cantilever beam FE model, representing an orthopedic cervical fixation plate was reported [32]. The authors mentioned that this probabilistic method was not very efficient,

requiring about 1,000 simulations to get a reasonably smooth distribution; therefore, a simplified FE model was employed. A 3-dimensional (3D) femur-implant model, in which variability of material properties and loading conditions were considered in order to predict a probability of failure, was also developed [38]. A simplified FE model for this femur-implant structure was used to avoid large computational time, and no geometry variability was considered. Therefore, to perform complex probabilistic analyses on human liver models, both variations in geometry and material properties of liver parenchyma properties could be investigated.

The main objective of this study was to investigate the variations of the material and shape properties of the human liver under loading ranges corresponding to automotive impact loading and to develop probabilistic human livers. It is believed that these data could be implemented in probabilistic human FE models which may help to better understand the risk of abdominal injuries and consequently contribute to the development of better designed safety systems.

1.2. Project Aims

Four aims in this dissertation are listed and discussed as follows.

(1) Development of the statistical size and shape models of the human liver. Mean and boundary models of these organs were also constructed.

(2) Investigation of the storage effects (cooling and freezing) on the material properties of porcine and bovine livers. Two loading types were conducted: indentation and tensile tests.

(3) Development of the distributions of material model parameters of the human liver using tensile tests with four loading rates (0.01, 0.1, 1.0, and 10.0 s^{-1}). Two approaches were conducted: marker data analysis and specimen-specific FE analysis.

(4) Development of probabilistic FE models of the human liver. The resulting probabilistic models were tested in a commercial human FE model, THUMS, under impact loading.

Chapter 2

Statistical Shape Analysis of Human Liver

2.1. Introduction

Statistical shape models (SSMs) show considerable capacity for the measurements of geometrical variability of human organs [42-46]. SSMs of the abdominal organs represent useful tools for the investigation of the organ variations for medical treatments [47, 48], and could be also applied to the development of computational probabilistic FE models [49, 50]. While some studies have investigated the shape variations of the abdominal organs (e.g. liver, spleen, and kidney) [43, 48, 51, 52], none of these studies has studied the shape of these organs in an occupant posture or proposed 3D boundary models [50] for the use of the FE simulations.

The statistical shape analysis (SSA) is a common technique to evaluate the size and shape variations. Traditionally, the SSA begins with manual identification of anatomical landmarks on the training shapes, and follows with the model registration which removes translation, rotation, and/or scaling differences [53, 54]. While the landmarks are also defined manually in some atlas-based segmentation schemes [55, 56], the landmarking process is time-consuming and it is challenging when few homologous, well-defined anatomical features, are available in complex 2D and 3D shapes [51, 57-62]. Therefore, semi-landmark approaches have been employed in the recent SSA studies. The semi-landmarks are the surface points utilized for the shape reconstruction of the object which are not required to be anatomic feature points [63]. In most semi-landmark approaches, the model registration, automatic landmark identification through correspondence process, and the principal component analysis (PCA) are included as major steps of the construction of 3D SSMs. The principal directions of variation, also called "modes of variation", could be represented by eigenvectors calculated from PCA [46]. Several studies have applied SSA on human internal organs [43, 47, 48, 51, 52, 64], bones [44-46, 65, 66], and the entire human body [67, 68]. Fripp et al. [65] and Bredbenner et al. [45] constructed the distal femur and proximal tibia models to investigate the shape variability of the knee joint. Giessen et al. [46] applied SSA on wrist bones and found that the first five modes have the highest variations. Lorenz et al. [66] developed 3D lumbar vertebrae shape models and built corresponding FE mesh models. SSMs for human soft tissues have also been studied such as pancreas [48], liver [52], kidney and spleen [43, 64] shape models. All of these recent studies utilized PCA to construct SSMs and present at least first three significant shape modes.

Some studies have investigated the shapes of the abdominal organs (liver, spleen, and kidney) using various approaches. Chen et al. [43] constructed 3D shape models of human liver, spleen, and right and left kidneys using minimum description length (MDL) for the landmark correspondence. Davies et al. [51] also constructed the shape models of the first three modes of rat kidney using MDL approach. Nevertheless, this method involves an extensive optimization process, resulting in substantial computational time [69]. Lamecker et al. [52] built the shape models for human livers. While the first three principal modes were presented in their study, the

percentage of the contribution of each principal component (mode) and the examinations of the normality of the modes were not reported. Reyes et al. [48] investigated the shape models of human liver, spleen, and kidney, and a multi-level shape model approach [47], which divided the organs into anatomical parts, were implemented. Since the normalization of the organs was executed, the size differences were not considered in their study. In all of these abdominal shape analysis studies, the abdominal organs of the subjects were scanned in supine posture, or the postures during image data collection were not clearly stated.

Since abdominal organs such as liver, kidney, and spleen are soft tissues, the shapes of these organs may vary in different postures [70, 71]. Beillas et al. [70] quantified the effects of postures on the positions and shapes of the abdominal organs. Magnetic resonance imaging (MRI) scans were obtained from subjects with four postures: supine, standing, seated and forward-flexed. The authors have shown that organ volume was mostly unaffected by postures. In addition, they found that except for the supine posture, the organ positions were mostly unaffected between seated, standing, and forward-flexed positions. They also found that the supine posture was associated with a motion of all abdominal solid organs of up to 39 mm when compared with the seated, standing, and forward-flexed positions. The authors suggested that the abdominal geometries in different postures should be considered accordingly in FE simulations. Hayes et al. [71] compared the location and morphology of abdominal organs between supine and seated postures. Both locations and the morphological changes in the organs were observed in their study. When comparing the seated posture to the supine posture, liver expanded 7.8% cranially and compressed 3.4% and 5.2% in the anterior-posterior and medial-lateral directions, respectively. Similar results were found in spleen and kidney. These studies suggested that the shapes of the abdominal organs change in different postures mostly due to the gravitation.

To automatically build SSMs from a training set of shapes, finding point correspondence across images becomes an essential task [64]. Several correspondence approaches to determine the corresponding landmarks between shapes have been proposed and compared in the literature [43, 46, 52, 69, 72, 73]. Dalal et al. [69] proposed a correspondence approach, which establish landmarks on a selected shape (template), and use the shortest distance between the landmarks on the template surface and the points on the target surfaces to determine the corresponding landmarks on the target surfaces. However, estimating corresponding points based merely on minimum Euclidean distance was found to be inaccurate in regions with large curvatures [63], and if the two aligned shapes do not have a certain amount of overlapping, the approach based on shortest distance may fail to establish the correct correspondence [73, 74]. To solve this problem, some improved correspondence algorithms were proposed using both coordinates and surface normal [57, 73, 75]. Comparing to each landmark on the template surface, the surface point on a target model with the smallest Euclidean distance and smallest differences between surface normals was chosen as the target landmark [73, 75]. In addition, Belongie et al. [76] showed that the iterative thin-plate spline (TPS) algorithm, which was first introduced by Bookstein [77], could efficiently refine the corresponding landmarks and showed that this iterative algorithm performs faster than the landmark sliding approach proposed by Dalal et al. [69], without loss of accuracy. Our study will therefore adopt the iterative TPS algorithm proposed by Belongie et al. [76].

The objective in this chapter was to develop 3D mean and boundary shape models of liver. The first few principal components which contributed a total of more than 70% of the overall variation were presented [46]. Mean and boundary models were constructed for human livers, so these models could be later used in the probabilistic FE models.

2.2. Methodology

An overview of the SSA processes on human livers is shown in Fig. 2.1. The MRI images of human livers scanned in a seated posture were obtained from 15 subjects. Corresponding landmarks were established from the MRI images through the segmentation, registration and correspondence processes. The SSMs of human livers were then constructed from the corresponding landmarks using PCA. The details of these processes are shown in the following sections.

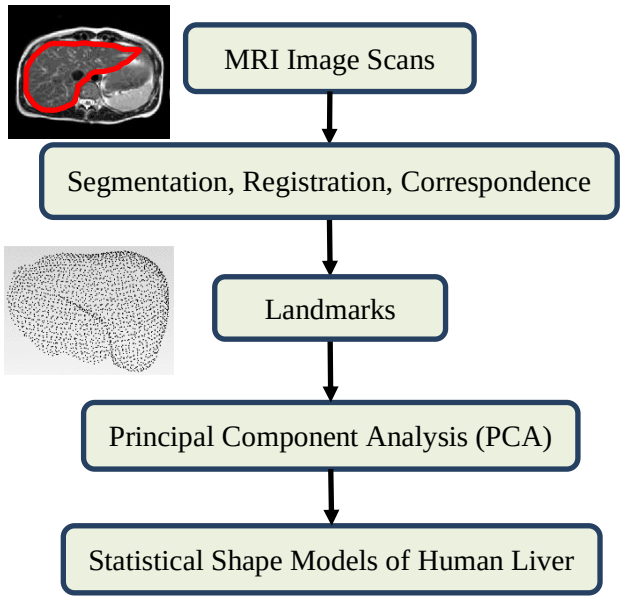

Figure 2.1. Processes of statistical shape analysis on human livers.

2.2.1. Image Acquisition

The shapes of livers used to build the SSMs were reconstructed from the MRI images of 15 subjects in a seated posture. The details of the MRI image acquisition can be referred to the studies conducted by Beillas et al. [70] ("Lyon" dataset) and Hayes et al. [71, 78] ("Wake" dataset). The demographic data of these subjects are listed in Table 2.1.

Table 2.1. Demographic data of subjects.

Subject ID	Sex	Height (m)	Weight (kg)	Age (yrs)	Source
F01	Female	1.74	68	41	Lyon
F02	Female	1.72	64	42	Lyon
F03	Female	1.62	53	34	Lyon
F04	Female	1.50	48	24	Wake
F05	Female	1.62	60.8	31	Wake
F06	Female	1.67	91.7	33	Wake
M01	Male	1.75	70	29	Lyon
M02	Male	1.91	88	32	Lyon
M03	Male	1.75	64	29	Lyon
M04	Male	1.69	60	26	Lyon
M05	Male	1.81	80	26	Lyon
M06	Male	1.83	82	37	Lyon
M07	Male	1.60	56.2	27	Wake
M08	Male	1.75	78.6	26	Wake
M09	Male	1.90	102.1	26	Wake

In the "Lyon" dataset, the subjects were seated in a custom built seat, with a seat back angle of 65 degrees to the horizontal plane and a seat pan angle of 9 degrees to the horizontal plane (Fig. 2.2a) [70]. The height of the seat was adjustable. The MRI scans were performed at sagittal plane of the subjects. The MRI slice resolution was 256 by 256 pixels, with a pixel size of 1.5625 mm by 1.5625 mm. This created an image area of a 400 mm by 400 mm per slice. In total 54 to 60 slices were obtained for each subject with a constant distance chosen from the range of 1-5 mm between two slices depending on the width of the subject. The subjects were instructed to breathe calmly during the MRI scanning process. The 3D polygonal surfaces were reconstructed from the MRI scans using Imod (University of Colorado, Boulder, CO) and Scilab (www.scilab.org) open-source software packages.

In the "Wake" dataset, the pixel size of the MRI images was 2.1 mm, and the field of view was 430 mm [71, 78]. The distance between two image slices ranged from 1.5 to 2 mm. The back seat had an angle of 67 degrees to the horizontal plane, and the seat pan was perpendicular to the back seat (Fig. 2.2b). While there was a slight discrepancy of the back seat angles between these two datasets, Beillas et al. [70] have shown that the organ volumes and their positions were mostly unaffected between seated, standing, and forward-flexed postures. The 3D polygonal surfaces were created from the MRI images using Mimics (Materialise, Leuven, Belgium), and were refined by Geomagic Studio (v. 11, Geomagic, Raleigh,NC) software.

In both datasets, the resolution of the MRI images used for organ segmentation preserved the shapes of the organs as compared to the raw MRI images [70, 71]. Point clouds of approximated 45,000 points for each liver were generated from the polygonal surfaces reconstructed from MRI images. These point clouds were then used in SSA as described in the following sections.

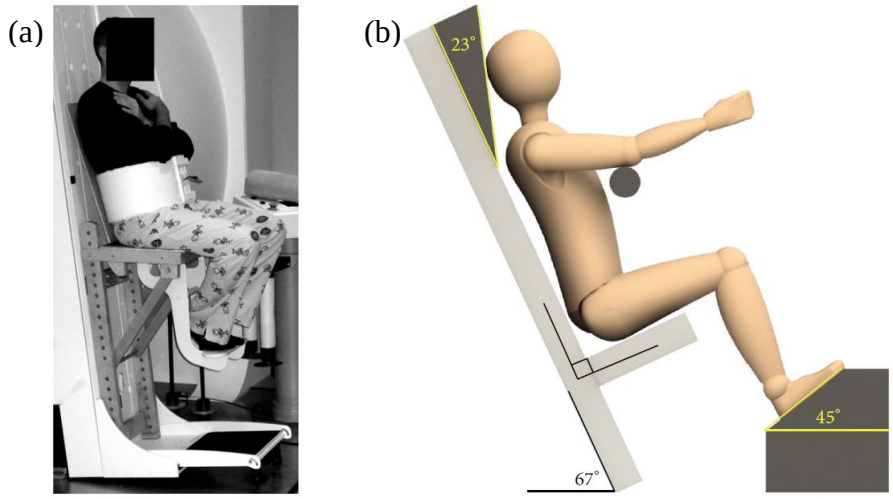

Figure 2.2. Subject seated positions: (a) "Lyon" dataset; (b) "Wake" dataset.

2.2.2. Registration

During the registration process, position and orientation differences between organs were minimized such that the only remaining differences between the organs could be quantified by size and shape variations. One subject's organ was selected randomly as the "template", and the remaining 14 target liver models were registered to it. In the current study, the liver model from a 50th percentile male in Wake dataset was selected as the template in this study. This registration process utilized all surface points on the template and target models, and the landmark identification was conducted after the registration process (Section 2.2.3).

A registration approach, the Iterated Closest Point (ICP) technique, introduced by Besl and McKay [79] and Zhang [80], has become the most popular approach for aligning 3D models based purely on the geometry [46, 57, 81, 82]. ICP was widely used because of its simplicity and its performance. ICP starts with two meshes and an initial guess for their relative rigid-body transform, and then it iteratively refines the transformation by repeatedly generating pairs of corresponding points on the meshes and by minimizing an error metric. While the algorithm converges relatively quickly, the initial estimate is not reasonably good [81]. Therefore, this study implemented a modified ICP method, called "LM-ICP registration", proposed by Fitzgibbon [81]. The LM-ICP abandons one of the basic characteristics of ICP, its closed-form inner loop, and employs instead a standard iterative non-linear optimizer, called the Levenberg–Marquardt (LM) algorithm [81]. Fitzgibbon showed that this approach incurs no significant loss of speed, but allows the extension of ICP to use truly robust statistics, with a concomitant reduction of dependence on the initial estimate.

2.2.3. Correspondence

After the registration, the correspondence process was performed to identify the landmarks on livers, which could be used for subsequent PCA. Three phases were involved in the establishment of landmarks on template and target surfaces: 1) establishment of the landmarks on the template surfaces; 2) establishment of surface normals for the landmarks on

template surface and the points on target surfaces; 3) establishment of the landmarks on the target surfaces.

The landmarks on the template surface were first constructed by the equal-size cubic grid method, proposed by Dalal et al. [69]. The basic consideration is that the template surface point is sufficiently dense to represent the surface of the organs, but sufficiently sparse for the construction of a compact SSM. The 3D space for the template surface was divided into equal-size cubic grid cells [69]. For each cell containing some surface points, the one closest to the center of this cell was picked as a landmark. A 2D illustration of this process is shown in Fig. 2.3. The size of the grid cell could be altered to control the number or the density of the template landmarks, and it was chosen as 7 × 7 × 7 mm for livers. The numbers of the template landmarks was 2,133 for livers.

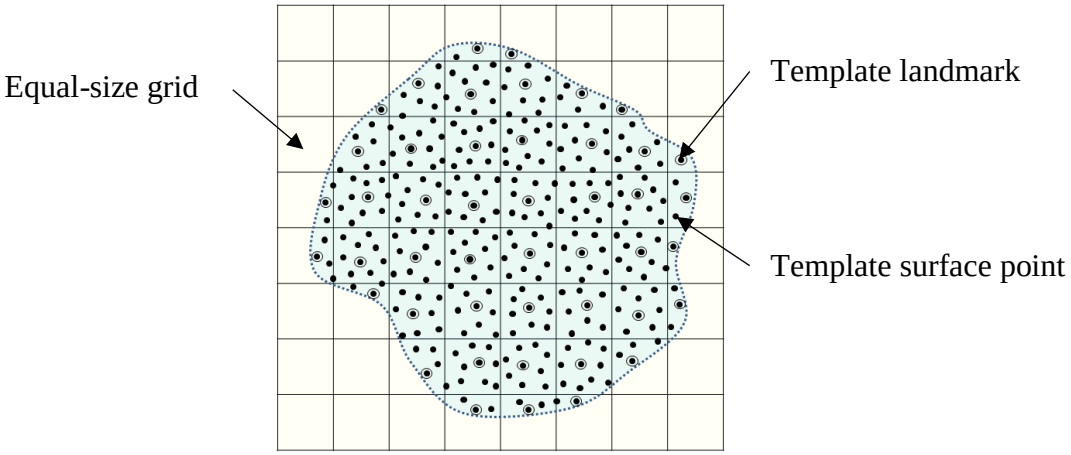

Figure 2.3. An illustration of constructing template landmarks from point clouds (2D case).

The second phase was to find the surface normal (Fig. 2.4a) of each landmark on the template surfaces and of each point on the target surfaces. The number of points on the target surfaces was first reduced to a certain number in order to accelerate the process of correspondence, by randomly selecting the points from the point clouds of initial approximated 45,000 surface points for each liver. The effects of three reduced numbers of surface points (5,000 vs. 10,000 vs. 20,000) on the shape correspondence were compared by the measures for shape-correspondence evaluation (Section 2.2.7).

The surface normals could be found through the following process. First, let the set of the template landmarks be U_L, and let the set of all target surface points be V. Each landmark in U_L is denoted as $u_i \in U_L$, and each point in V is denoted as $v_j \in V$. The following five steps should be achieved to determine the surface normals [69].

Step 1. Find a few nearest neighbors of u_i or v_j, where the neighbors have the distances less than 3 mm between the neighbors and u_i or v_j.

Step 2. Construct a 3×3 covariance matrix of nearest neighbors with respect to their x, y, z coordinate positions.

Step 3. Perform eigen decomposition of the covariance matrix.

Step 4. The eigenvector corresponding to the smallest eigenvalue is the direction around which least variation is observed. Since we find a small set of k-nearest neighbors which should be fairly flat, this smallest eigenvector, denoted as $\overrightarrow{n_i}$ or $\overrightarrow{n_j}$, corresponds to the normal direction of the surface at u_i or v_j. Normalize the eigenvector corresponding to the normal direction.

Step 5. Each surface normal should then be determined whether it points out of surface or points into the surface. A set of dense point clouds is created inside of surfaces. For each u_i (or v_j), a closest point, u_p (or v_p), inside the surfaces is chosen. To orient all normals consistently towards outside of the surface, they need to satisfy the equation:

$$\overrightarrow{n_i} \cdot (u_p - u_i) < 0 \text{ (template) and } \overrightarrow{n_j} \cdot (v_p - v_j) < 0 \text{ (template)} \qquad \text{(Eq. 2.1)}$$

If a surface normal on the template surface has a value of $\overrightarrow{n_i} \cdot (v_p - u_i)$ greater than zero, then a negative sign is given to the surface normal to make its direction towards outside of the surface.

After establishing the surface normals of u_i and v_j, two correspondence approaches, proposed by He et al. [73] and Giessen et al. [75], were utilized for identifying the landmarks on the target surface and were compared by the measures for shape-correspondence evaluation (Section 2.2.7).

2.2.3.1. "He" Approach

The following three steps were achieved to find the target landmarks.

Step 1. For each $v_j \in V$, find its closest landmark $u_i \in U_L$ based on the Euclidean distance. Several v_j may select the same u_i as their closest landmark on U_L.

Step 2. For each $u_i \in U_L$, group the set of $v_j \in V$ that select this u_i as their closest landmark on U_L and denote this set as V_i.

Step 3. If there is only one point in V_i, this point is chosen as the corresponding landmark of u_i on the target surface. Move this point to the set of the target landmark V_L and remove the point from V. If there are more than one point in V_i, select one point from V_i whose surface normal is closest to the surface normal of u_i. Move this point to the set of the target landmark V_L and remove the point from V. If there is no points in V_i, select one closest point from V based on the Euclidean distance and assign this point as the corresponding landmark of $u_i \in U_L$. Move this point to the set of the target landmark V_L and remove the point from V. The resulting set of $v_i \in V_L$ are the corresponding landmarks on the target surface.

2.2.3.2. "Giessen" Approach

Comparing to each landmark on the template surface, the surface point on a target model with the smallest Euclidean distance and differences between surface normals was chosen as the target landmark. Considering two triangulated surfaces A and B, the correspondence between a point a_i on surface A and a point b_{ai} on surface B was defined by the minimum Euclidean distance in a six-dimensional space:

$$b_{ai} = \arg\min_{b_j} \|a_i - b_j\| \quad \text{(Eq. 2.2)}$$

with $a_i = \begin{bmatrix} \xi_i \\ \phi n_i \end{bmatrix}$ and $b_j = \begin{bmatrix} \xi_j \\ \phi n_j \end{bmatrix}$, where ξ_i and ξ_j are the point coordinates (non-normalized values), and n_i and n_j are the surface normals (normalized values) (Fig. 2.4b). To avoid the possible problem of selecting the same target surface point for two different template landmarks, a target surface point was excluded from the search space if it has been included in the target landmarks in previous searches [46, 75]. The weight factor ϕ was experimentally determined and tested for the values of 0, 0.5, … , 5. A good correspondences and little differences for various ϕ values were observed visually when ϕ was set between 1 and 2.5, so ϕ=1 was chosen in this study.

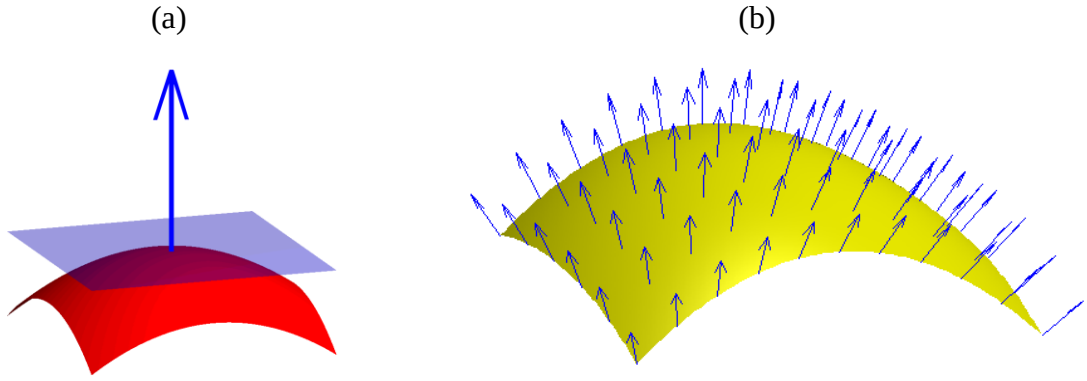

Figure 2.4. Illustrations of surface normals: (a) A typical surface normal; (b) Each point on the surface has a coordinate (3-dimension) and a surface normal (3-dimension).

2.2.4. Refining the Target Landmarks by Iterative TPS

After the initial corresponding landmarks between template and target surfaces were established, the quality of the target landmarks could be further improved by iterative TPS algorithm through transformation functions [73, 76, 77]. A transformation function T could be calculated based on the initial correspondence between template and target landmarks, U_L and V_L. Suppose the number of landmarks is n_L in U_L and V_L. Let the landmarks in U_L be $u_i =$

(u_{ix}, u_{iy}, u_{iz}) and the landmarks in V_L be $v_i = (v_{ix}, v_{iy}, v_{iz})$, i=1,…, n_L, where u_i and v_i are the corresponding landmarks for the same i. The TPS function which transforms the target landmarks to the template landmarks can be expressed as:

$$f(v_{ix}, v_{iy}, v_{iz}) = a_0 + a_x v_{ix} + a_y v_{iy} + a_z v_{iz} + \sum_{j=1}^{n_L} w_j \phi(\|(v_{jx}, v_{jy}, v_{jz}) - (v_{ix}, v_{iy}, v_{iz})\|) \quad \text{(Eq. 2.3)}$$

where $\phi(r) = r$ in 3D case. Therefore, each TPS function has n_L+4 parameters (a_0, a_x, a_y, a_z, w_1,…, w_{n_L}). Three TPS functions, f_x, f_y, f_z, are utilized to represent the transformation function T of x, y, z coordinates.

$$T(v_{ix}, v_{iy}, v_{iz}) = \left(f_x(v_{ix}, v_{iy}, v_{iz}), f_y(v_{ix}, v_{iy}, v_{iz}), f_z(v_{ix}, v_{iy}, v_{iz})\right) = (u_{ix}, u_{iy}, u_{iz}) \quad \text{(Eq. 2.4)}$$

Each TPS functions (f_x, f_y, and f_z) has the same form as Eq. 2.3; therefore, Eq. 2.4 contains $3n_L$ simultaneous equations with a total of $3(n_L + 4)$ unknown parameters. For each TPS function, four additional constraints are imposed [76]:

$$\sum_{i=1}^{n_L} w_i = 0 \text{ and } \sum_{i=1}^{n_L} w_i x_i = \sum_{i=1}^{n_L} w_i y_i = \sum_{i=1}^{n_L} w_i z_i = 0 \quad \text{(Eq. 2.5)}$$

Thus, these 3(n_L+4) parameters in each transformation function T can be simply solved by the $3(n_L + 4)$ simultaneous equations (Eq. 2.4 and Eq. 2.5). The transformation function T can be applied to the entire set of the target points V.

The initial corresponding landmarks U_L and V_L are first utilized to estimate a transformation function T. This transformation function T is then used to transform all points in V, and the transformed points are denoted as V^1. The Phase 3 in Section 2.2.3 is applied to U_L and V^1 to find a new set of landmarks from V^1, denoted as V_L^1. A new transformation function T^1 can be estimated by U_L and V_L^1, and then transform the points on V^1 to a new set of points, denoted as V^2. Continuing this transformation process with k iterations, the landmark set V_L^k on surface V^k can be determined. The indices of the target landmarks are tracked during each iteration so the k-iteration target landmarks can be mapped to their original positions on V. Five iterations were executed for each correspondence calculation between two surfaces (k=5). The CPU time about 1.5 hours (Microsoft Windows workstations equipped with Intel Core i5-2400 CPU at 3.10 GHz processors) was required to obtain corresponding landmarks between one template and 14 target surfaces using 5-iteration TPS for human livers.

2.2.5. Principal Component Analysis

The mean shape and its deviations were computed using PCA, based on the established landmarks [45, 64, 72]. PCA was also used to determine the modes of variation and to define axes that were aligned with the principal directions. Let N be the number of 3D training shapes and P be the number of 3D landmarks per model. Conventionally, each shape can be represented by a vector x_k whose dimension is $3P \times 1$ where k=1,…, N. The mean vector $\bar{x}$ and the covariance matrix D are computed from the set of object vectors as [72]:

$$\bar{x} = \frac{1}{N}\sum_{k=1}^{N} x_k;\ D = \frac{1}{N-1}\sum_{k=1}^{N}(x_k - \bar{x}) \cdot (x_k - \bar{x})^T. \quad \text{(Eq. 2.6)}$$

An eigen decomposition on D delivers max(N-1, 3 P) principal modes of variation, e_i (eigenvectors), and their respective variances λ_i (eigenvalues) [63], where i stands for the ith mode (Eq. 2.7). The sorted eigenvalues λ_i and eigenvectors e_i of the covariance matrix D are the principal directions spanning a shape space with $\bar{x}$ at its origin. The modes of variation are orthogonal and thus statistically independent. A mode with a high variance describes a larger part of the total size and shape variation between shapes. The percentage of variability of each mode can therefore be defined as $\lambda_i / \sum_{i=1}^{N-1} \lambda_i$.

Typically, only the first few modes with large eigenvalues (i.e. large variance) describe meaningful size and shape variations. The modes with smaller eigenvalues mainly describe noise that emanates from MRI scanning and random point sampling. The number of elements in each data vector is larger than the number of shapes and therefore the covariance matrix has as many non-zero eigenvalues as the number of shapes minus one, i.e. N-1 [46].

Each mode of variation is a dimension of the distribution space that describes similar shapes to the abdominal organs used in this study. Objects $\tilde{x}_j$ in the shape space are described as a linear combination of the eigenvectors on $\bar{x}$ (Eq. 2.7).

$$D \cdot e_i = \lambda_i e_i;\ E = \{e_i\};\ \tilde{x}_j = \bar{x} + E \cdot H = \bar{x} + \sum_{i=1}^{q} e_i h_i \qquad \text{(Eq. 2.7)}$$

where e_i are the eigenvectors of the covariance matrix that describe a set of orthogonal modes of size and shape variation, $H = \{h_i\}$ are shape parameters that control these modes of variation, and q is the number of preselected modes of variation [58, 59].

2.2.6. Distribution of Shapes

To satisfy the conditions for developing the size and shape models, it is necessary to examine the normality of the principal component scores [46]. These scores, calculated as linear combinations of the original landmarks and the principal components, were the positions of each abdominal organ in this new coordinate system of principal components. The scores for each mode could be plotted as a histogram, and their distributions could be tested whether they were not significantly different from normal distributions. A series of Kolmogorov–Smirnoff (K–S) tests on the similarity between standardized principal component scores and a standard normal distribution had to be conducted to test the null hypothesis that the principal component scores were normally distributed. The distributions of principal component scores with p-values greater than 0.05 were judged to be not significantly different from the normal distribution.

2.2.7. Three Measures for Shape-Correspondence Evaluation

The goodness of correspondence was quantified using three measures widely applied in the literature [46, 50, 51, 58, 69, 72, 83]. While short descriptions of these measures for evaluating shape-correspondence performance are briefly outlined below, a more detailed treatment could be referred in Davies' study [58].

The measures for shape-correspondence evaluation were applied to two scenarios: (1) comparison of the shape-correspondence between three reduced numbers of target surface points (5,000 vs. 10,000 vs. 20,000); (2) comparison of the shape-correspondence between "He" approach and "Giessen" approach;

2.2.7.1. Model Compactness

A compact model is one that has slight variance and requires few parameters to define an instance. The important information is captured in a plot of cumulative variance of the M^{th} mode:

$$C(M) = \sum_{i=1}^{M} \lambda_i \quad \text{(Eq. 2.8)}$$

where λ_i is the i^{th} eigenvalue. If for two methods α and β, $C_\alpha(M) \leq C_\beta(M)$ for all M and $C_\alpha(M) < C_\beta(M)$ for some M, it is concluded that model α is more compact.

The standard error of $C(M)$ is determined from the training set size N:

$$\sigma_{C(M)} = \sum_{i=1}^{M} \sqrt{\frac{2}{N}} \lambda_i \quad \text{(Eq. 2.9)}$$

2.2.7.2. Model Generalization

The generalization ability of a model measures its capability to represent unseen instances of the class of object modeled. This is a fundamental property as it allows a model to learn the characteristics of a class of objects from a limited training set. A model over-fitted to the training set is unable to generalize to unseen examples. The generalization ability of each model is measured from the training set using leave-one-out reconstruction. A SSM is constructed based on 14 livers, leaving a randomly selected test liver out. Then, the model is fit to the test organ using a selection of the q modes with the highest variances. Error is measured by calculating the mean difference of the predicted surface points and the surface points on the test liver. The experiment is carried out for M=1, 2,…, 14 modes of variation and repeated 15 times with different test shape selections for each mode M. As in the compactness criterion, if for two methods α and β, $G_\alpha(M) \leq G_\beta(M)$ for all M and $G_\alpha(M) < G_\beta(M)$ for some M, it can be concluded that the generalization ability of method α is better than that of method β.

2.2.7.3. Model Specificity

A specific model should only generate instances of the object class that are similar to those in the training set. This property can be accessed qualitatively by generating a population of instances using the model and then comparing them to the members of the training set. A quantitative measure of specificity as a function of M can be defined as:

$$S(M) = \frac{1}{\widehat{N}} \sum_{j=1}^{\widehat{N}} \left| \tilde{x}_j(M) - x_j \right| \quad \text{(Eq. 2.10)}$$

where $\tilde{x}_j$ are sample examples generated by the model using first M modes and x_j is the nearest member (minimum difference between landmark positions) of the training set to $\tilde{x}_j$. The experiment is carried out for M=1, 2,…, 19 modes of variation and $\widehat{N}$=1,000 iterations. A model α is more specific than β if $S_\alpha(M) \leq S_\beta(M)$ for all M and $S_\alpha(M) < S_\beta(M)$ for some M.

2.2.8. Statistical Boundary Shape Models

The most commonly used Anthropomorphic Test Dummies (ATDs), so called "50$^{\text{th}}$ percentile" ATD, tried to approximate median male seated height and body weight. In an effort

to cover the variation in size and shape that reflect the whole occupant populations, different percentile ATDs were developed as well (e.g. 5^{th} percentile female and 95^{th} percentile male). The distributions of mass and seated height were usually the only variables used in development of these percentile ATDs [84, 85]. However, several studies showed that the mass and stature only describe part of the complexity of the human body's shape and only captures a small percentage of the population [67, 68]. To mitigate that problem, this study utilized a novel approach for developing "statistical boundary shape models" (or simply "boundary models") based on SSA [50, 86].

The essential difference between the percentile models and boundary models is how they were created. The percentile models were traditionally developed (by scaling) based on the percentiles of the anthropometric data (e.g. mass and stature). However, the boundary models were developed from the multi-normal distributions of the shape modes which try to cover a percentage of the whole population [50].

The mean model was determined as the mean of the corresponding landmarks [87], i.e. $\bar{x}$ in Eq. 2.6, and the PCA was applied to identify the most significant modes of liver size and shape models, which were then utilized to construct the boundary models. While the mean model was unique, the definition of boundary models constructed from principal modes was challenging.

The term "κ% boundary models", was used to define the boundary models which cover κ% of overall population [50, 86]. For example, if the distributions of the principal component scores are not significantly different from normal distribution (Section 2.2.6), the shape space [-1.96 SD, 1.96 SD] of each mode will cover 95% of the overall population (SD: standard deviation) [50, 86].

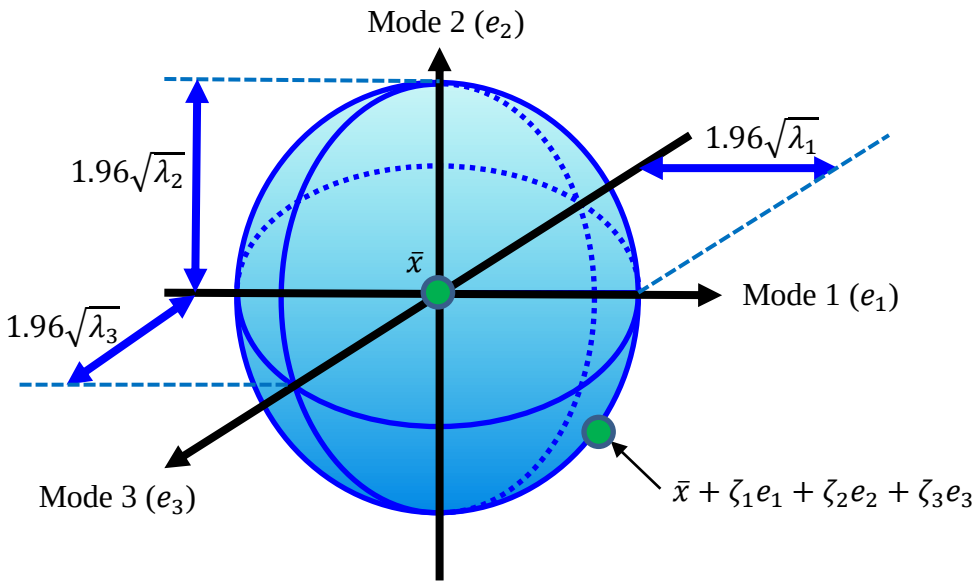

Figure 2.5. An illustration of the set of 95% statistical boundary models developed using three pre-selected modes (q=3) (Lu et al., 2013).
Note: Each eigenvector e_i (dimension: 3 P ×1) is not the same as the basis vector of ordinary 3D Euclidian space (dimension: 3×1).

The set of statistical boundary models could be defined as q-hyper-rectangles [50] around the mean model, where q is the number of pre-selected orthogonal modes of variation. However, this approach may over predict the boundaries of κ% boundary models, similar to the rectangle approach used to define the boundaries of test data corridors [88, 89]. Therefore, a q-hyper-ellipsoid approach [86] was used to define the set of boundary models (Fig. 2.5). In this approach, a statistical boundary model ($\hat{x}$) is a point of the q-hyper-ellipsoid and it is defined as:

$$\hat{x} = \bar{x} + \sum_{i=1}^{q} \zeta_i e_i \qquad \text{(Eq. 2.11)}$$

where ζ_i are shape parameters with q-dimensional elliptical coordinates.

When q=2 (Fig. 2.7), the 2-hyper-ellipsoids equation for 95% boundary models is

$$\sum_{i=1}^{2} \frac{\zeta_i^2}{(1.96\sqrt{\eta_i})^2} = 1 \qquad \text{(Eq. 2.12)}$$

Therefore, ζ_i are

$$\zeta_1 = 1.96\sqrt{\eta_1}\cos(\delta)$$

$$\zeta_2 = 1.96\sqrt{\eta_2}\sin(\delta) \qquad \text{(Eq. 2.13)}$$

where $0 \leq \delta < 2\pi$.

Sets of ζ_i would be changed according to different q. For example, when q=5, the 5-hyper-ellipsoids equation for 95% boundary models is

$$\sum_{i=1}^{5} \frac{\zeta_i^2}{(1.96\sqrt{\eta_i})^2} = 1 \qquad \text{(Eq. 2.14)}$$

Therefore, ζ_i are

$$\zeta_1 = 1.96\sqrt{\eta_1}\cos(\delta_1)$$

$$\zeta_2 = 1.96\sqrt{\eta_2}\sin(\delta_1)\cos(\delta_2)$$

$$\zeta_3 = 1.96\sqrt{\eta_3}\sin(\delta_1)\sin(\delta_2)\cos(\delta_3)$$

$$\zeta_4 = 1.96\sqrt{\eta_4}\sin(\delta_1)\sin(\delta_2)\sin(\delta_3)\cos(\delta_4)$$

$$\zeta_5 = 1.96\sqrt{\eta_5}\sin(\delta_1)\sin(\delta_2)\sin(\delta_3)\sin(\delta_4) \qquad \text{(Eq. 2.15)}$$

where $0 \leq \delta_i \leq \pi$ when i=1,2,3, and $0 \leq \delta_i < 2\pi$ when i=4.

By adjusting the shape space, different κ% boundary models can be obtained. For instance, the shape space [-1.65 SD, 1.65 SD] of each mode can be used to develop the "90% boundary models."

2.3. Results

The compactness, generalization and specificity were used to evaluate the shape-correspondence constructed using "Giessen" approach between three reduced numbers of surface points (Fig. 2.6a-2.6c). The compactness values of models constructed using 10,000 and 20,000 surface points were similar and both smaller than corresponding values of the model with 5,000 surface points (Fig. 2.6a). A similar trend was found for the generalization and specificity properties (Fig. 2.6b and 2.6c), indicating that the sufficient number of target surface points for constructing the SSMs was 10,000 and therefore it was used to construct SSMs for the rest of the comparisons and analysis.

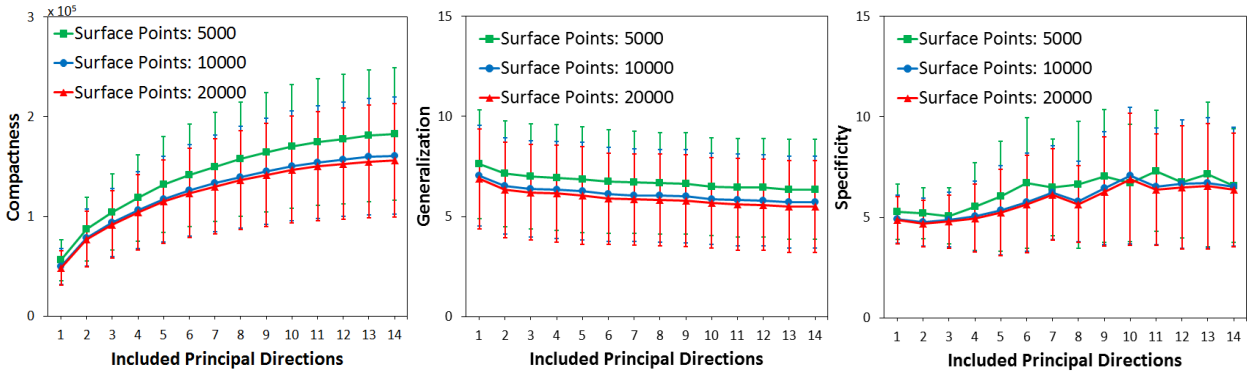

Figure 2.6. Quantitative evaluation (compactness, generalization, and specificity) on human liver data (Error bar: 1 SD) between three reduced numbers of surface points. A better model is a model with lower values of compactness, generalization and specify for a certain number of principal modes.

The three measures for shape-correspondence evaluation were also applied to compare the models constructed by "He" approach and "Giessen" approach, using 10,000 target surface points (Fig. 2.7). The values of the compactness, generalization and specificity from "Giessen" approach were smaller than the corresponding values from "He" approach. This indicates that the "Giessen" approach gave the better correspondence results in terms of the three measures for shape-correspondence evaluation (Fig. 2.7). Both approaches require similar CPU time (90 minutes on Microsoft Windows workstations equipped with Intel Core i5-2400 CPU at 3.10 GHz processors) for determining the corresponding landmarks of all liver models. Therefore, the "Giessen" approach was chosen to construct the mean and boundary models of the human liver.

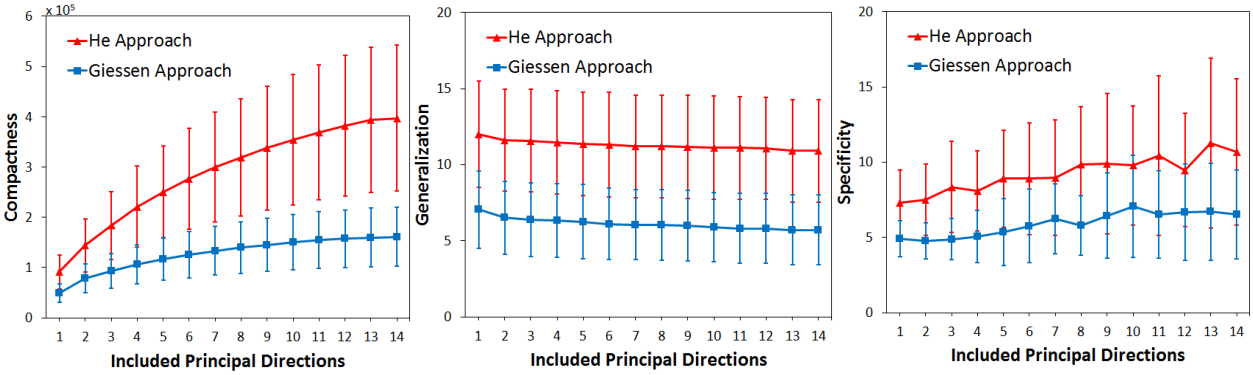

Figure 2.7. Quantitative evaluation (compactness, generalization, and specificity) on human liver data (Error bar: 1 SD) between "He" approach and "Giessen" approach.

The principal components of 15 human liver shape analyses were presented here using "Giessen" correspondence approach and 10,000 target surface points, and the SSMs of human liver were constructed using PCA. Overall, the first five modes accounted for total 73% (Fig. 2.8). The first five modes were chosen to graphically represent their corresponding SSMs since in total they contributed greater than 70% of the overall anatomical variability of human liver

[46]. The noise of MRI scanning and random point sampling influenced the higher modes. The LM-ICP registration method used to align all 15 livers required CPU time of about 10 minutes on Microsoft Windows workstations equipped with Intel Core i5-2400 CPU at 3.10 GHz processors.

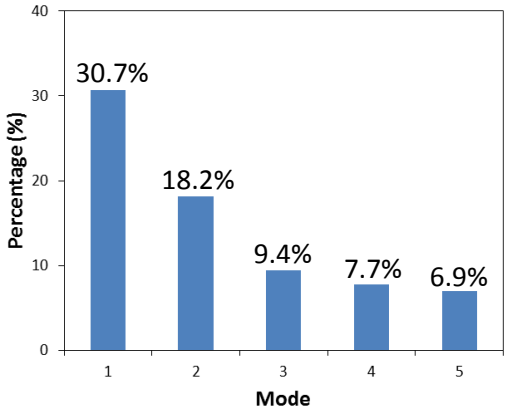

Figure 2.8. Percentage of variation contributed by each mode for the human liver statistical shape model.

The liver size and shape models were plotted for -3 SD, mean, and +3 SD for the first five modes (Fig. 2.9). The height of the liver was found to be the most significant variation (30.7%) on the first principal component (Fig. 2.9, Mode 1). Changes of the thickness and width of the liver were found in the second mode (Fig. 2.9, Mode 2), which represented 18.2% of the global variance. The third mode of variation represented 9.4% of the global variability and corresponded to the variation of the concave of the right lobe (Fig. 2.9, Mode 3). The fourth mode of variation represented 7.7% of the entire variance, and the curvature of the liver was found to be the main difference between the shape models in this mode (Fig. 2.9, Mode 4). The angle of the two lobes from the medial view and the height of left lobe were found to be the variations on the fifth principal component, accounting for 6.9% of the overall variation (Fig. 2.9, Mode 5).

Mode	-3 SD	Mean Shape	+3 SD	Var.	Description
1 (P)	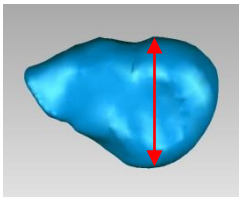	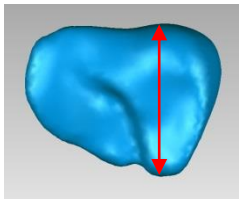	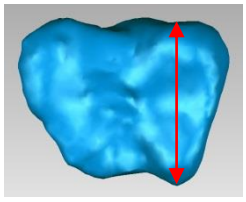	30.7%	Height of liver
2 (S)	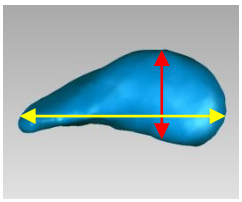	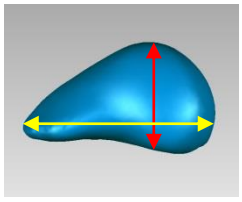	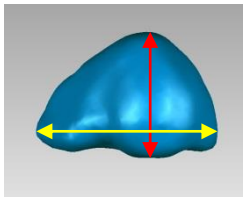	18.2%	Thickness and width of liver
3 (L)	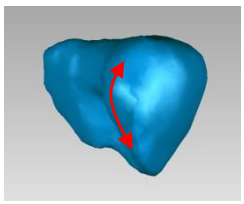	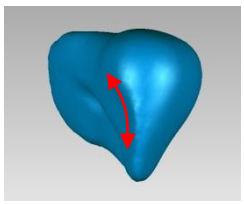	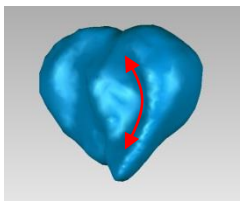	9.4%	Concave of right lobe
4 (S)	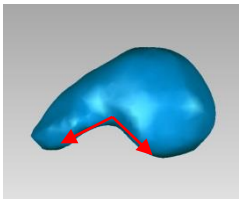	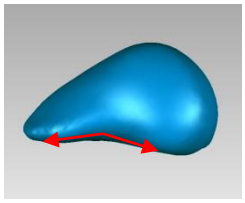	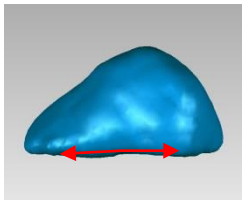	7.7%	Curvature of liver
5 (M)	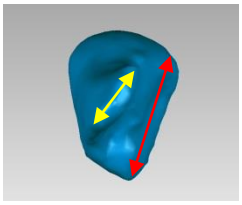	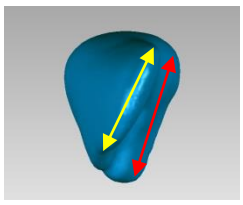	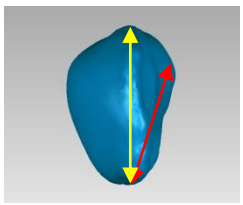	6.9%	Angle of two lobes and height of left lobe

Figure 2.9. The first five modes of variation of human livers. P: Posterior view; S: Superior view; L: Lateral view; M: Medial view.

The modes used for the construction of the boundary models were described by a set of principal component score distributions. These score distributions corresponding to the first five modes of human liver were standardized by their means and SD (Fig. 2.10). All p-values from the Kolmogorov–Smirnoff test on the similarity between the standardized principal component scores and a standard normal distribution were greater than 0.05 (Fig. 2.10). This indicates that the distributions of the principal component scores were not significantly different from normal for all five modes in human livers.

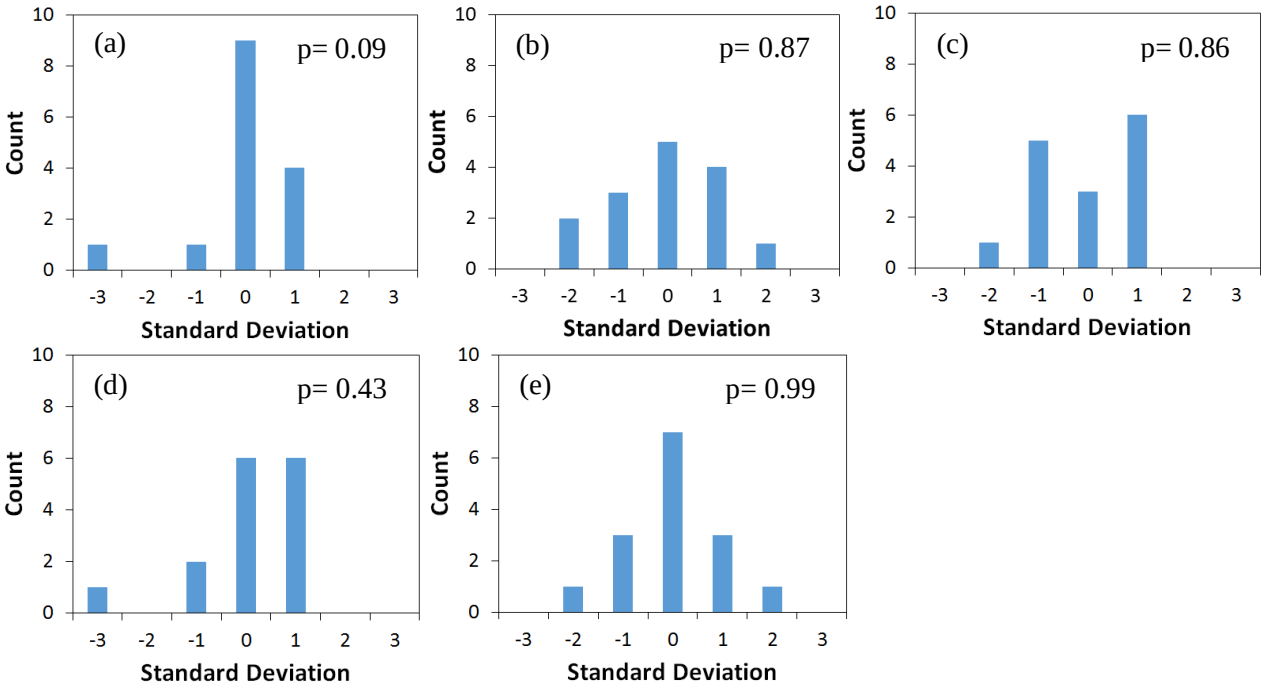

Figure 2.10. Distribution of principal component scores of the first five modes of human liver. p represents p-value resulting from a Kolmogorov–Smirnoff test on the similarity between standardized principal component scores and a standard normal distribution. p-values>0.05 represent normally distributed shape parameters.

The surfaces of four selected 95% boundary models of the human liver were constructed (Fig. 2.11). These boundary models correspond to 1) $\delta_1 = \delta_2 = 0, \delta_3 = \delta_4 = \pi$, 2) $\delta_1 = \delta_2 = \delta_3 = \delta_4 = \pi/4$, 3) $\delta_1 = \pi/2$, $\delta_2 = 0, = \delta_3 = \pi/2, \delta_4 = 0$ and 4) $\delta_1 = \pi$, $\delta_2 = \delta_3 = \delta_4 = 0$ (Eq. 2.15). No linear correlations of 3D shapes were observed between the variations of the boundary models, as is assumed by traditional scaling methods used frequently to develop percentile models.

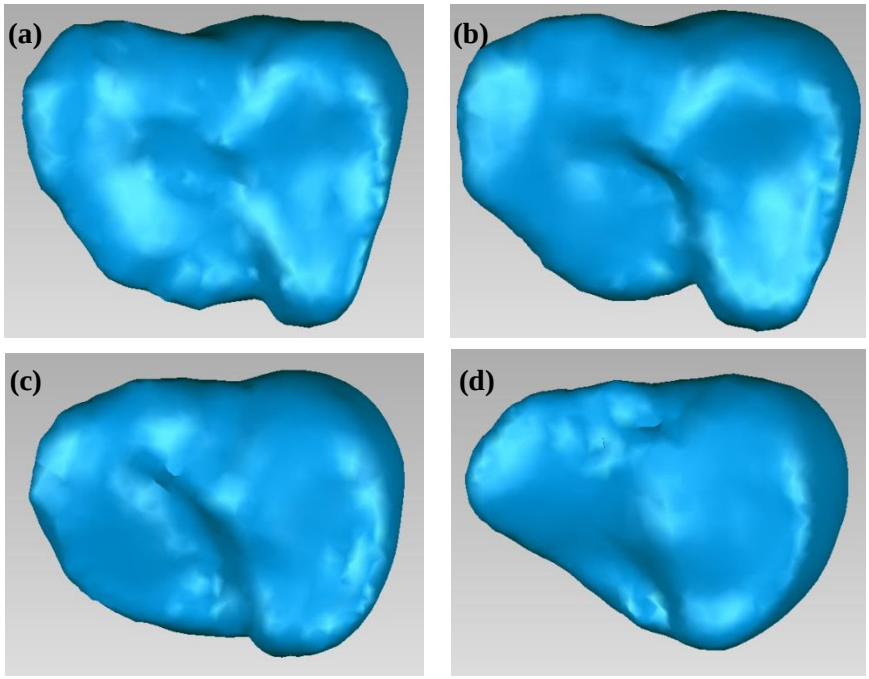

Figure 2.11. Four selected boundary models of human liver, developed using the first five principal component modes: (a) Boundary model #1; (b) Boundary model #2; (c) Boundary model #3; (d) Boundary model #4.

2.4. Discussion

Although the variations of human liver geometry have been investigated in a few previous studies, the subjects' liver scans in these studies were obtained at supine position or the scanning postures were not specified. The current study fully investigates the liver shape variations based on seated posture models. The first two variation modes of liver shape presented in this study are different from the corresponding modes reconstructed from subjects in supine postures [52, 90]. Kohara et al. found that the size of the right lobe of the liver accounted for the first mode variation, and the size of the left lobe of the liver accounted for the second mode variation [90]. However, they used a less number of the surface points (1,000 vertex points) to express the liver training shapes, whose results could be biased as demonstrated in the current study. Lamecker et al. also showed that the sizes of the two lobes accounted for the major variations of the first three modes, using 12,500 surface points for each training shape [52]. In both studies, the liver scans utilized to construct shape models were from both male and female subjects at supine postures. The differences of the shape variations between these previous studies and current study could be explained by the shape changes of the abdominal organs due to gravitation between supine and seated postures reported previously [70, 71], by different populations and/or SSA methodologies used in the their studies. In addition, some previous studies on liver shape models focused on the development of new correspondence methodologies [43] or multi-level SSA [47, 48], and the modes of variation were not clearly defined.

The comparison of the liver volumes between current and previous studies is shown in Fig. 2.12. The liver volumes in this study were measured using Rhino v. 5.0 (Robert McNeel &

Associates, Seattle, WA) for all 11 shape models in Fig. 2.9 (One mean shape and ten +3/-3SD shape models). The average and SD were then calculated based on these 11 shape models (Fig. 2.12, first column). Hayes et al. measured the liver volume based on a single subject (midsized male) at seated posture [71]. While the body size of the subject recruited in Hayes' study was close to a 50th percentile male, it was shown that its liver volume may not be close to an average liver volume measured from population-based studies (Fig. 2.12). Other studies [91-93] measured the liver volumes from Caucasian adults including both male and female subjects scanned at the supine postures. It was already reported that the liver volume does not change between supine and seated postures [71]. In Fig. 2.12, the liver volumes obtained in the current study had no significant difference when comparing to the liver volumes reported by Heinemann et al. [92] using two-sample t-test assuming unequal variances (p=0.596). The higher average liver volume reported by Chouker et al. [91] and lower average liver volume reported by Vauthey et al. [93] could be due to the recruited subjects in their studies.

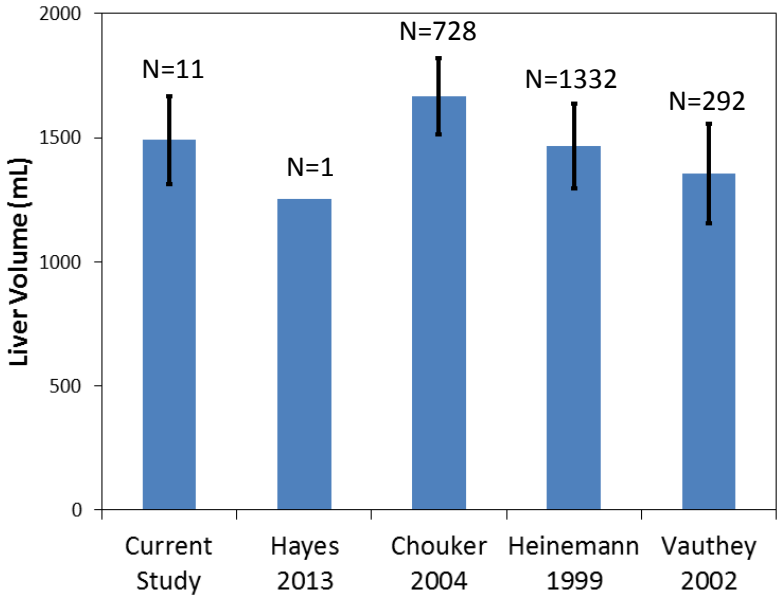

Figure 2.12. Comparison of the liver volumes between current and previous studies. Error bar: 1SD.

It was found in the current study that a sufficient number of surface points on a target model was 10,000 for the liver shape correspondence process. However, the original point clouds from the MRI scans had a lower number of surface points (less than 5,000) due to the MRI slice thickness. Therefore, in the current study, point clouds of approximated 45,000 points for each liver were generated from the original polygonal surfaces constructed from MRI images. It should be noted that these refined point clouds were obtained from the fitted polygonal surfaces and may not represent exactly the original liver surfaces. Thus, it is suggested to use higher resolution medical image scans to obtain refined 3D models in order to conduct statistical shape analysis.

In this study, the normalization of the training shapes was not considered. Two main reasons for the normalization [67] are: (1) Normalization isolates the shape variation from the height variation; (2) Normalization improves the correspondences between the models because if

the models are at the same height, their anatomical components tend to align better with each other. Several studies have normalized the training shapes of their models such as hippocampus [69], patella bone [65], and pancreas [48], while other studies did not consider the normalization scaling on their shape model applications such as tibia [45], spine [66], and liver [52]. The current study did not incorporate the normalization of the training shapes because the size variation of the liver models should be considered for constructing the crash test FE abdominal models.

The current study showed that the "Giessen" approach performed better than the "He" approach in terms of the three measures of shape-correspondence evaluation. This indicates that the coordinates and surface normals of landmarks should be combined together (six-dimensional space, Eq. 2.2) to determine the corresponding landmarks. While the surface normal was also considered in "He" approach, it was used only when multiple target surface points were initially chosen for a template landmark (Section 2.2.3.1, Step 2 and 3). This could induce some discrepancy of the surface normals between certain target landmarks and their corresponding template landmarks. Therefore, it is suggested to use the six-dimensional space of the combined coordinate and surface normal information of surface points to establish the corresponding landmarks between shapes.

An optimization technique for improving the correspondence, called "iterative landmark sliding" (SLIDE), had been proposed recently [69]. The approach has shown to be better than MDL and spherical harmonics (SPHARM), in terms of three shape model evaluation measures (compactness, generalization, and specificity). While the SLIDE optimization was not considered in the current study, it has been shown that the correspondence map established using coordinates and surface normals along with iterative TPS to refine landmarks is sufficient to obtain similar results of refined landmarks [74]. In addition, it was also shown that the iterative TPS approach requires less computational time, and all the corresponding landmarks are on the original surface without sliding away [73, 74]. Moreover, the CPU time for the registration and correspondence process with SLIDE optimization was considerably high (4.6 hours on Microsoft Windows workstations equipped with Intel Core i5-2400 CPU at 3.10 GHz processors) for their hippocampus models, whose geometry were simpler than the liver models [69]. The LM-ICP registration and correspondence process in our 15 liver models without the SLIDE optimization required less than 90 minutes. Therefore, considering efficiency and accuracy, the SLIDE optimization may not be required, but the comparison of correspondence maps with SLIDE and without SLIDE is suggested to be investigated in future studies.

The shape variations between 95% liver boundary models (Fig. 2.11) indicate that the traditional scaling technique based on geometry parameters such as height and width may not be sufficient for constructing different percentile anthropometric models. This scaling technique has been extensively applied in crash test dummies [85, 94]. The mesh of HUMOS2 model was scaled to any percentile in driving position through only 10 (external) parameters[94]. The Polar-II FE model was scaled in vertical direction to match the stature (height) and in the transverse plane to match the total mass between the pedestrian dummy model and subjects, in order to create 5^{th} female, 50^{th} female, and 95^{th} male FE models [85]. The current study showed that the changes between 95% liver boundary models are irregular and non-linear, thus the proposed boundary models provide a better perspective on liver variations than the traditional percentile

models. While several studies have investigated the shape models of bones (e.g. pelvic bone [56]) or soft tissues (e.g. brain ventricle [57]) represented by each single principle component, the current study is the first study which combines the most significant five shape modes to construct mean and boundary liver models using a novel and efficient correspondence approach ("Giessen" approach). This technique could be applied to other human tissues and the resulting shape models could be further used to investigate the biomechanical response corridors [85].

The concept of the κ% boundary models can be extended to build numerous shape models in the new shape space by adjusting the shape parameters. For example, suppose each mode of variation is not significantly different from the normal distribution, samples inside the boundaries can be generated by the Latin Hypercube approach from the multinormal distribution formed by the principal modes, and shape instances can therefore be constructed based on these samples. This approach could produce generalized shape models, which cover a wider range of shape variations rather than merely 95% variations, which were considered in the current study.

It was reported by Beillas et al. [70] that the the subject-to-subject variations of abdominal organ size and position would be larger than changes due to different postures, especially for human spleen and kidney. However, this was not applied to human liver, where the size and shape changes due to subject-to-subject variations would be smaller than the changes caused by different postures [70]. This shows again the importance of using the seated posture MRI scans to construct SSMs of the liver.

One limitation in this study is that we treated the liver as a homogeneous material, which is typical in a majority of human FE models [27, 95-97]. Therefore, only liver surfaces were reconstructed for the SSMs based on the MRI images. An approach utilizing the relationship between tissue's material property and relative density on medical images for constructing the femoral head shape models was proposed by Belenguer Querol et al. [70]. The authors built the correspondence map between template and target shapes based on not only the Euclidian coordinates but also the intensity at voxel of CT scans. The advantage of this approach is that the established SSMs have the information of the tissue density on each landmark and therefore provide refined material property distribution along the shape. However, robust universal relationships for soft tissues of abdominal organs have not been published yet. Therefore, the incorporation of the density information from medical images into SSA may not be applicable at this time. Furthermore, the Kolmogorov–Smirnoff tests used for the examination of the normality of the principal component scores may be influenced by the relative small sample size. This is especially true when marginal significance is observed (e.g. p-value=0.09). While the subjects recruited in the current study covered a wide range (5% percentile female-95% percentile male) and our sample size (N=15) was close to the sample sizes utilized in previous liver statistical shape analysis studies (N=18 in [90] and N=20 in [52], it is suggested in future studies to use larger sample size to construct SSMs to avoid the possible bias caused by the size of the samples. The current study focuses on the size and shape variations of the liver itself. The location and orientation of the liver relative to other body organs (e.g. spleen and kidney) could be obtained by extending the concept of the shape analysis to a larger scale. For example, some studies have applied the SSA to whole body scale to discover the variations of the relative positions and orientations between body segments [67, 68, 98]. This could be a critical topic for future research to connect size and shape FE models of internal organs and bones.

The proposed approaches and the strategies could be also applied to other abdominal solid organs such as kidney and spleen. In addition, the size and shape models of the human liver could be further combined with distributions of liver material properties to develop probabilistic FE models of the liver [99]. Using these probabilistic FE models in impact simulations could also help to better understand the variability observed in biomechanical and injury response of the abdominal organs under impact loading [100].

Chapter 3

Effect of Preservation on Material Properties of Liver Parenchyma

3.1. Introduction

The abdominal injury criteria were determined exclusively from PMHS in recent studies [49, 101, 102]. However, it is unclear that whether the injuries recorded in these tests associated with some changes of material properties of PMHS livers due to preservation. In addition, while the material properties of abdominal tissues were recently investigated, most of these studies [103-106] tested only fresh human or porcine abdominal organs. Since the majority of abdominal tests used to develop injury criteria were done with preserved cadavers [49, 101, 107-110], there is a need to better understand possible changes to the material properties of the abdominal tissues caused by preservation methods (such as cooling or freezing).

In recent years, PMHS have served as invaluable tools for the characterization of human biomechanical responses during impact loading [107, 111]. Therefore, the development of reliable preservation methods for PMHS, which minimize the biomechanical differences between living humans and preserved PMHS, became very important for biomechanics research. During the late 1960s, it was shown that the embalming process changes the response of human tissues [111]. As a result of these findings, the testing of embalmed PMHS was abandoned. From this point on, freezing and refrigeration methods have been widely used to store and preserve unembalmed post mortem tissue. Typically, freezer storage methods are used to preserves post mortem tissue at temperatures ranging from -10°C to -70°C. Various studies have shown that freezing within this range does not have effect on the biomechanical response of bone or collagenous tissues such as ligaments or intervertebral discs [9, 112-118]. While several studies have reported some comparisons of the mechanical properties between fresh and previously frozen abdominal organ tissues [7, 8, 119], the effect of cooling and freezing on the mechanical response of the liver tissue under different loading rates is still largely unknown.

A number of studies have investigated the effects of freezing on the responses of animal livers under different types of loading schemes. Brunon et al. [1] conducted quasi-static tensile failure tests on both fresh and previously frozen porcine liver parenchyma and capsule samples, and found that freezing affects the failure properties of porcine liver capsule but not human liver capsule. Ocal et al. [8] conducted compressive impact experiments on bovine liver specimens to investigate the effect of preservation period (1h-48h after harvesting) on the viscoelastic material properties and found that the liver tissue becomes stiffer and more viscous as the preservation time increases. Santago et al. [10] compared the tensile failure stress and failure strain of fresh bovine liver parenchyma and bovine liver parenchyma frozen for 26 days and concluded that freezing decreased the failure strain. However, the study by Santago et al. [10] was limited to samples obtained from only one bovine liver and the evaluate of a single loading rate. Nguyn et al. [6] investigated the influence of a freeze-thaw cycle on the stress-stretch curves of porcine

liver and reported that the mechanical properties of the liver tissues were almost unaffected by the freeze-thaw cycle. Tamura et al. [7] performed a series of pre-conditioning compression tests on fresh and previously frozen porcine liver specimens and determined that freezing had no effects on the mechanical response of the tissue. However, it is possible that damage to the tissue during the pre-conditioning may have masked any potential changes in the compressive response resulting from the freezing process.

Although there have been some studies that have investigated the effect of freezing on liver tissue, the conclusions regarding the effect freezing on the material response of liver tissues varies between studies. The discrepancies between these studies could potentially be due to variability in the composition of the liver tissues between mammalian species, the preservation periods, the loading rates, or the mechanism of loading.

The scope of this chapter was to investigate the influence of freezing and refrigeration storage methods on the biomechanical responses of porcine and bovine livers. Two tests were included in this chapter. First, the local material properties of the porcine livers were obtained from the indentation testing, a popular testing method which requires only a small volume of tissue and relatively easy sample preparation [120], for fresh and preserved specimens. The test data recorded in typical relaxation tests and a quasi-linear viscoelastic (QLV) model were used to characterize the dynamic behavior of porcine liver. Second, the influence of freezing on the biomechanical responses of the bovine liver parenchyma in tensile loading was investigated.

3.2. Methodology

3.2.1. Indentation Testing on Porcine Livers

3.2.1.1. Specimen Preparation and Testing Procedure

The overall indentation testing procedure is shown in Fig. 3.1a. Five intact fresh adult porcine livers were obtained from a local slaughterhouse, saved in plastic bags covered by towels, and stored in an ice container with 4.5 kg ice during transportation until use. The direct contact between the organs and the ice was therefore avoided. After arrival, each liver was sectioned into two equal halves: one half was used to investigate the freezing effect, and the other half was used to investigate the cooling effect. Four specimens ($25\times25\times15$ mm^3) were cut, using a custom blade assembly, from each half, keeping both the fibrous capsule and parenchyma intact and attached together. A total of 40 specimens were obtained (5 livers×2 halves per liver×4 specimens per half).

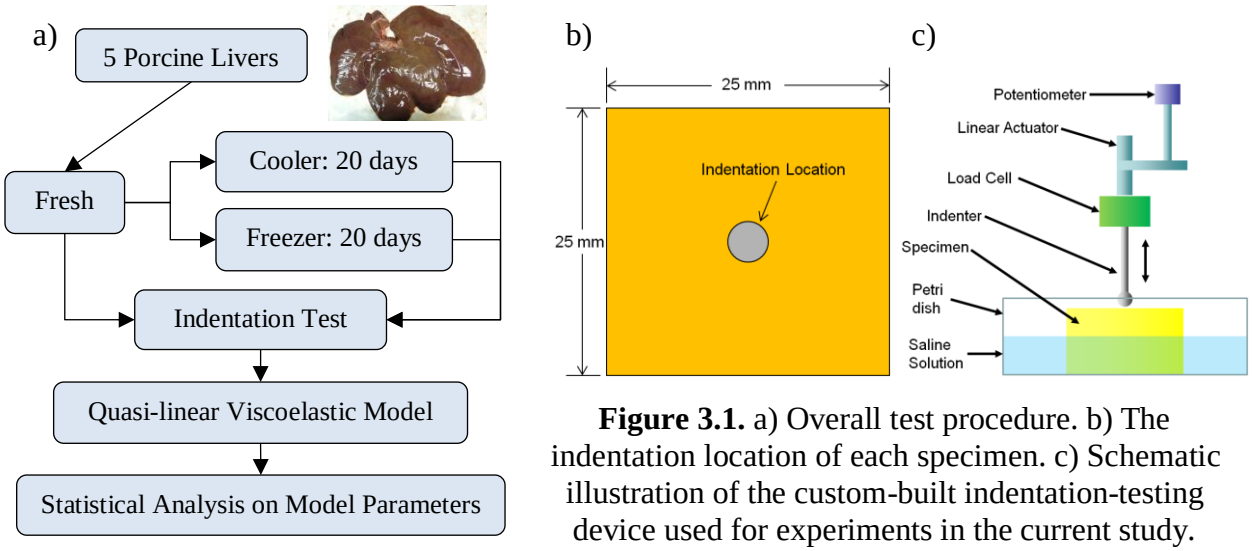

Figure 3.1. a) Overall test procedure. b) The indentation location of each specimen. c) Schematic illustration of the custom-built indentation-testing device used for experiments in the current study.

Indentation tests were first conducted on the capsule side of the porcine liver specimens within 4 hours of obtaining the tissues. Indentation ramp-hold tests with 1 mm displacement peaks (rate of indentation: 0.5 mm/s) and then a 2-minute hold time were conducted on the center of each specimen (Fig. 3.1b). A 250 g-force uniaxial load cell (Honeywell Sensotec, Inc., Columbus, OH) was mounted between the linear actuator and the shaft of the 3.175 mm-radius spherical indenter tip (Fig. 3.1c) [120]. A linear potentiometer (Novotecknik, model T-25, Southborough, MA) was mounted on the actuator to verify the input displacement–time profile. Indenter-material contact was determined prior to each test by detection of a small (5 mN) load change. To maintain a consistent temperature during testing, all samples were immersed in physiological (0.9%) saline (Fig. 3.1c) [105, 106, 121]. The samples were rested on the petri dish during testing without flotation. The testing temperature was chosen to be close to a normal room temperature (24°C), which approximates the post-mortem human surrogate (PMHS) temperature during abdominal tests. Four specimens from half of each organ were then frozen at -12°C (freezing storage), and the four specimens of the other half were stored at 4°C (cooling storage). All specimens were stored in the sealed container and under moist paper to ensure hydration, and then retested under the same testing condition and indentation locations after 20 days. This time interval approximates reasonably to the time required for performing the PMHS pre-test medical examinations and obtaining the required testing approvals [102, 107, 111]. The cooled and frozen specimens were rested in the saline before each test until a laser thermometer (Maverick Industries, Inc., model LT02, Edison, NJ) confirmed that the temperatures of the specimens were at 24°C. This thawing process until testing took approximately 3 hours and 9 hours for cooled specimens and frozen specimens, respectively. All fresh and preserved specimens were preconditioned (loading and unloading) by performing ramp-hold tests 3 times at a rate of 0.5 mm/s with 1 mm displacement peaks to reach the steady–state prior to the recording of force and displacement data during the 4^{th} cycle [7, 122].

3.2.1.2. Identification of Material Properties

The relationship between indentation force $P(t)$ and depth $h(t)$ was modeled using a QLV model:

$$P(t) = \int_0^t G(t-\tau)\frac{\partial P^e(h)}{\partial h}\frac{\partial h}{\partial \tau}d\tau \quad \text{(Eq. 3.1)}$$

where $P^e(h)$, representing the stiffness of a material, is the instantaneous elastic function, and $G(t)$ is the reduced relaxation function, and *t* is the time [123]. A discrete spectrum was assumed for the reduced relaxation function $G(t)$:

$$G(t) = G_\infty + G_1 e^{-\frac{t}{\tau_1}} + G_2 e^{-\frac{t}{\tau_2}} + G_3 e^{-\frac{t}{\tau_3}} \quad \text{(Eq. 3.2)}$$

subjected to the constraint $G(0) = G_0 = G_\infty + G_1 + G_2 + G_3 = 1$, where G_∞ is the long-time shear modulus ($G_\infty = \lim_{t\to\infty} G(t)$), and the G_i coefficients represent the relaxation strength corresponding to the τ_i time constant [124]. The contribution of the long-time shear modulus (G_∞) within the instantaneous shear modulus (G_0) can be simply represented by G_∞ (i.e. G_∞/G_0=G_∞) [120].

The duration of the ramp was about 2 seconds and the hold time was 120 seconds as in [120]. To reduce the number of unknown material parameters of the QLV model, three decay rates of relaxations ($1/\tau_i$) were assumed: τ_1=1 second, τ_2=10 seconds, and τ_3=100 seconds.

The relationship between the instantaneous elastic function P^e and the indentation depth *h* was assumed to have a formula similar to the isotropic elastic Hertzian contact (spherical indentation) expression for an incompressible material [120]:

$$P^e(\mathrm{t}) = \frac{8\sqrt{R}}{3}[2\mu_0]\cdot h(t)^{3/2} \quad \text{(Eq. 3.3)}$$

where *R* is the indenter radius, and μ_0 is the elastic shear modulus. The indentation force can then be described as:

$$P(t) = \frac{16\sqrt{R}}{3}\int_0^t G(t-\tau)\left[\frac{d}{d\tau}\left(\mu_0 h(t)^{3/2}\right)\right]d\tau \quad \text{(Eq. 3.4)}$$

The values of the reduced relaxation coefficients (G_∞, G_1, G_2, and G_3) and the elastic shear modulus (μ_0) (5 optimization variables) were obtained by minimizing the sum of squared errors (SSE) between the model and experimental forces using the active-set algorithm in MATLAB v. R2011b (The MathWorks, Inc., Natick, MA). This algorithm utilizes a sequential quadratic programming method used usually to solve medium scale optimization problems (problems with reduced number of variables) [125]. The initial values of G_∞, G_1, G_2, G_3, and μ_0 were chosen as 0.25, 0.25, 0.25, 0.25, and 5000 kPa, correspondingly. The time history of the indentor displacement recorded in testing was used in the calculation of the model indentation force (Eq. 3.4). The averaged coefficient of determination (R^2) was calculated between the model and experimental forces for each treatment.

G_∞ and μ_0, corresponding to the reduced relaxation response and instantaneous elastic response, served as indicators for comparing fresh and preserved tissues and comparing the cooled and frozen storage methods.

3.2.1.3. Statistical Analysis

To investigate the possible changes induced by cooling and freezing, the paired two-sample t-test was employed to compare material parameters (G_∞ and μ_0) between fresh and cooled tissues and between fresh and frozen tissues. A paired two-sample t-test is defined as

$$t = \frac{\bar{d}}{\sqrt{s^2/n}} \sim t_{df=n-1} \quad \text{(Eq. 3.5)}$$

where $s^2 = \sum_{i=1}^{n} \frac{(d_i - \bar{d})^2}{n-1}$, $\bar{d}$ is the mean difference between two measurements, and n is the sample size. The mean differences between two measurements tested at fresh and Day 20 were calculated, along with their corresponding p-values of the paired two-sample t-test. The critical α value was set to be 0.01 [126].

In addition to the evaluation between the fresh and Day 20 tissues, a comparison between cooling and freezing effects was conducted by using a statistical approach called Generalized Estimating Equations (GEE). GEE is a robust statistical method employed to study population-average pattern or trend over time for longitudinal data [127]. The statistical model was expressed as $Y = \beta_0 + \beta_1 x_1 + \beta_2 x_1 x_2$ where Y is the material coefficients (G_∞ and μ_0). x_1 (the preservation time) and x_2 (the preservation method) are dummy (indicator) variables which indicate the presence or absence of categorical effect that may be expected to shift the outcome (Y). The x_1 dummy variable was assigned the values of 0 and 1, representing the fresh and preserved specimens, respectively. Similarly, the x_2 dummy variable was assigned the values of 0 and 1, representing the specimens preserved by freezing and cooling, respectively. Therefore, the outcomes, average values of material parameters (G_∞ and μ_0) recorded on the preserved specimens, can be expressed as:

$$E[Y|frozen] = \beta_0 + \beta_1, \;\; E[Y|cooling] = \beta_0 + \beta_1 + \beta_2 \quad \text{(Eq. 3.6)}$$

The p-values of $\beta_2 = E[Y|cooling] - E[Y|frozen]$ less than 0.01 indicate that there are significant changes in terms of material properties between the specimens preserved by freezing and cooling. Both the paired two-sample t-test and GEE approach were conducted in SAS 9.2 (SAS Institute Inc., Cary, NC).

3.2.2. Tensile Testing on Bovine Livers

3.2.2.1. Specimen Preparation and Testing Procedure

Uniaxial tensile tests were performed on the parenchyma of 10 fresh bovine livers obtained from Animal Technologies (Tyler, Texas, USA) (Fig. 3.2). To investigate tissue responses in a longer preservation period than 20-day preservation in the porcine indentation study in Section 3.2.1, a different protocol with longer preservation periods was utilized [10]. Each organ was sectioned into three equal portions: one was tested immediately upon receipt; one tested after 30 days of frozen storage (Day 30); one tested after 60 days of frozen storage (Day 60). The bovine livers were received within 24 hours after slaughter. It has been shown that the tensile responses of the liver would not change within 24 hours after slaughter [1]. During transportation, the livers were saved in plastic bags and, stored in ice containers. Frozen specimens were stored in a sealed container at -12°C [128], and then tested under the same

testing condition as fresh samples after thawing. The time between the start of the thawing process and testing was approximately 12 hours. Frozen-thawed specimens were evaluated in this study because previously frozen PMHS are commonly used in abdominal impact tests [49]. These time intervals reasonably approximate to the time window required to obtain serology, required approval, and pre-test medical examinations for PMHS.

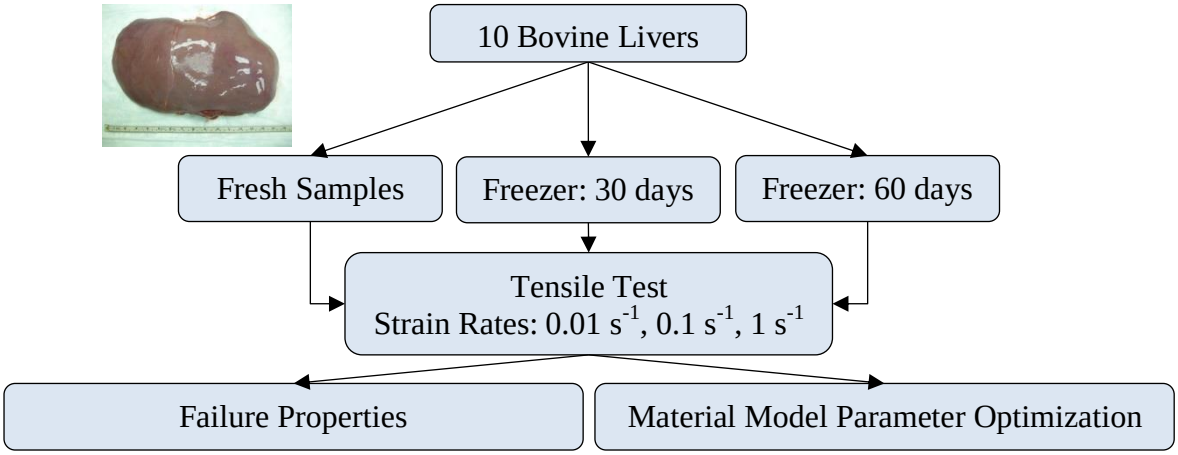

Figure 3.2. Overall procedure for bovine liver tensile testing.

The tissue slicing and stamping procedures described by Kemper et al. [2, 104] were used to obtain constant thickness "dog-bone" shaped liver parenchyma specimens (thickness: ~5mm, gage length: 19 mm, gage width: 10 mm) commonly used for uniaxial tensile testing [2, 104]. Cubic blocks of parenchyma (Fig. 3.3a,b) were first cut and securely held in a slicing jig, an aluminum fixture with vertical slots spaced 5 mm apart [2, 104]. The slicing was performed in a smooth motion, to avoid tissue damage and deformation, using a blade assembly consisting of five long skinner blades (R-203506MOD, American Cutting Edge, Centerville, OH) (Fig. 3.3c,d). A custom stamp and stamping base were used to obtain the "dog-bone" shape specimens (Fig. 3.4). The stamp dimension used in the current study was described by Kemper et al. [2] (Fig. 3.3). The parenchyma specimens without capsule had their longitudinal axis (loading direction) parallel to the liver surface (Fig. 3.4d). All samples were then immersed in a bath of Dulbecco's Modified Eagle's Medium to maintain specimen hydration until testing [2, 104]. Every specimen was tested once until failure at a temperature close to a normal room temperature (24°C).

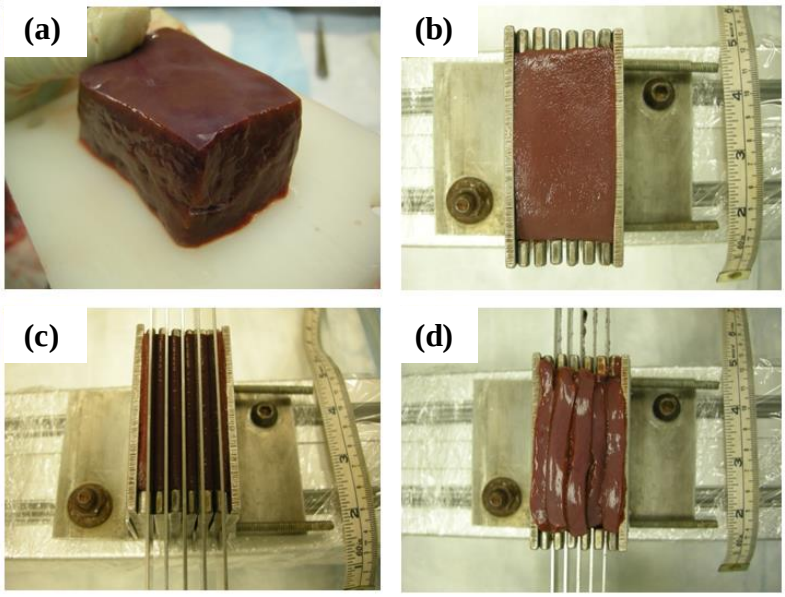

Figure 3.3. Specimen slicing methodology (fresh liver).

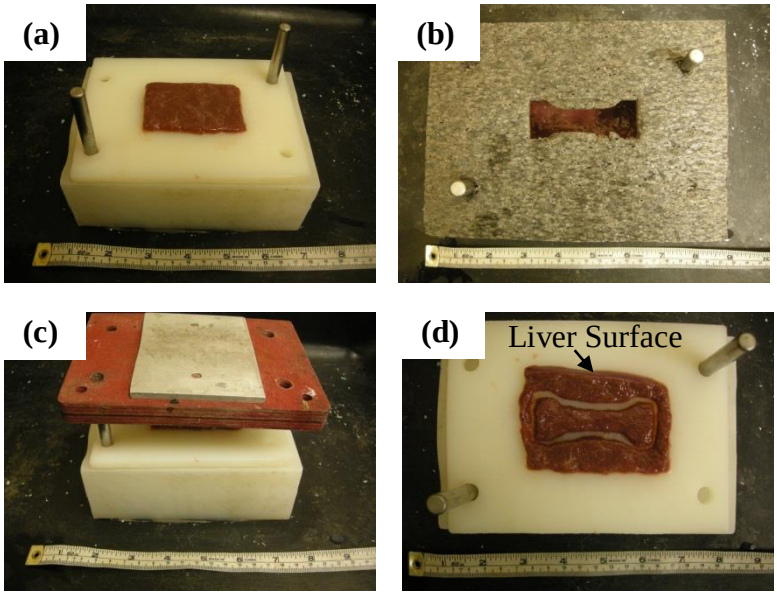

Figure 3.4. Specimen stamping methodology (fresh liver).

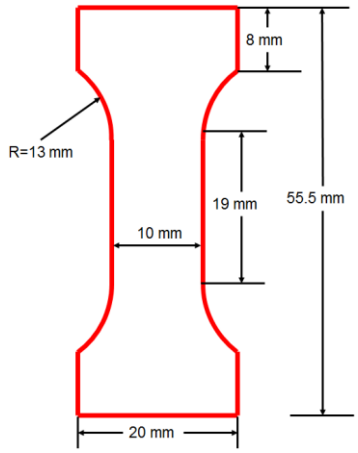

Figure 3.5. Specimen size.

Specimens from each group (fresh, Day 30, and Day 60) were divided into three sets which were tested until failure at the following strain rates: 0.01 s^{-1}, 0.1 s^{-1}, and 1.0 s^{-1} in order to characterize the tissue strain-rate dependency over a large range of strain rates. It should be noted that these strain rates are consistent with similar previous publications [2, 104].

The tensile testing system consisted of two motor driven linear stages (Parker Daedal MX80S, Irwin, PA) mounted to a vertically oriented aluminum plate (Fig. 3.6). A uniaxial load cell (Interface, WMC Miniature-22.24N, Scottsdale, AZ) and an accelerometer (Endevco 7264B, 2000 G, San Juan Capistrano, CA) were mounted between the linear actuator and the grip. The system was operated with a multi-axis controller (Parker ACR9000, Irwin, PA), which provided synchronized motion of both linear stages, and a motor driver (Parker ViX, Irwin, PA). The specimen mounting procedure described by Kemper et al. [2, 104] was used to ensure that all specimens had a minimal but consistent preload (i.e. 1 g of tension caused by gravitation). The testing system loaded the specimen by simultaneously moving the top and bottom grips away from one another at a constant velocity.

A typical uniaxial test is shown in Fig. 3.7. The force and displacement time histories were recorded during each test, along with high-speed video. The data acquisition and video sampling rates for each loading rate are listed in Table 3.1. A collinear and equidistant pattern of optical (white dot) markers was applied to each specimen prior to testing with about 4 mm between each marker (Fig. 3.6). A high speed video camera (Phantom V4, Vision Research, Wayne, NJ), with a resolution of 7.7 pixels/mm, was used to record the marker movements at different sampling rates during testing (Table 3.1). The testing temperature was chosen to be normal room temperature (24°C), which is representative of the temperature used during PMHS abdominal impact tests.

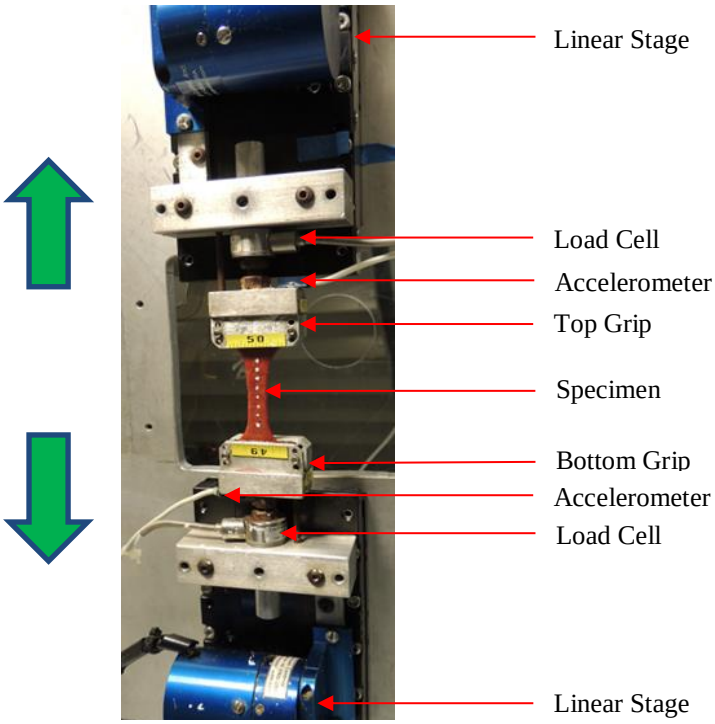

Figure 3.6. Experimental setup (fresh liver).

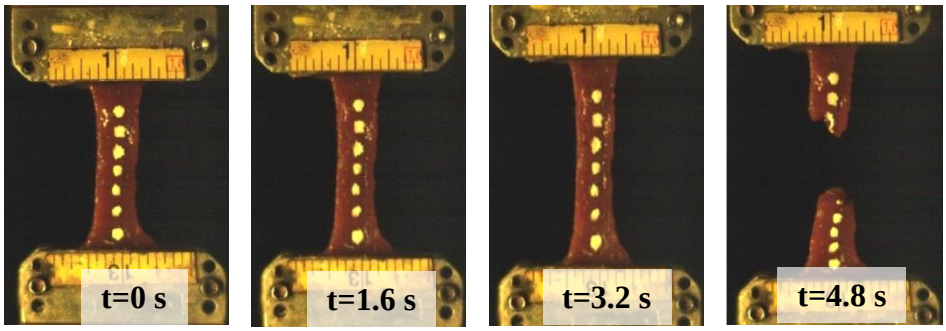

Figure 3.7. High-speed video stills of a typical uniaxial tensile test (Fresh, Rate 2: 0.1 s^{-1}).

Table 3.1. Data acquisition and video sampling rates by loading rate.

Rate	Desired Strain Rate (s^{-1})	Data Acquisition (kHz)	Video (Hz)
Rate 1	0.01	0.2	20
Rate 2	0.1	2.0	70
Rate 3	1.0	20.0	500

In the majority of the tests, the tissue tears were propagated gradually until complete disruption of the tissue without a sudden drop of the tensile force. Defining the failure time is challenging because some tears occurred inside of the tissue or on the back surface of the tissue and therefore were not video-recorded. Therefore, the point of the force-time curve where the

force reaches a maximum and then decreases more than 3% of its peak value is defined as failure point, and its corresponding time is defined as the "time of failure". This corresponded to the timing of the initiation of the failure tear when the initiation of the failure tear could not be observed in the video [2, 86, 88, 104].

3.2.2.2. Data Analysis

The material response of the specimens was analyzed using local and global models (Fig. 3.8). The local model (LM) approximated the specimen as a beam with the length corresponding to the closest optical markers spanning the location of the tear and constant initial cross-sectional area at the tear region located always in the middle region of the specimen (i.e. the gage length). The initial cross-sectional area at the region of the tear for LM was quantified by determining the location of the failure in the high-speed video and then determining the initial width and thickness at that location from the pre-test pictures. The marker displacement was calculated based on the two closest optical markers spanning the location of the tear site. The optical markers were tracked throughout the duration of the test using motion analysis software (TEMA Version 2.6, Linkoping, Sweden). The displacement between these markers was curve fit with a 5^{th} degree polynomial up to the time of failure (average R^2=0.936) to reduce the measurement noise because it was found that the 5^{th} degree polynomial fitted the displacement-time curves better than polynomials with other degrees [2, 104]. This methodology is consistent with that used by previous studies [2, 104]. The global model (GM) approximated the specimen as a beam with the specimen length corresponding to distance between the grips and constant initial cross-sectional area. The global displacement between the grips was measured during tests using potentiometers attached to the linear stages and then fit with a 1^{st} degree polynomial (average R^2=0.999) to reduce the measurement noise. The initial cross-sectional area for GM was calculated from pre-test pictures as the average of the cross-sectional areas at three locations: the middle location, 3 mm above the middle location, and 3 mm below the middle location.

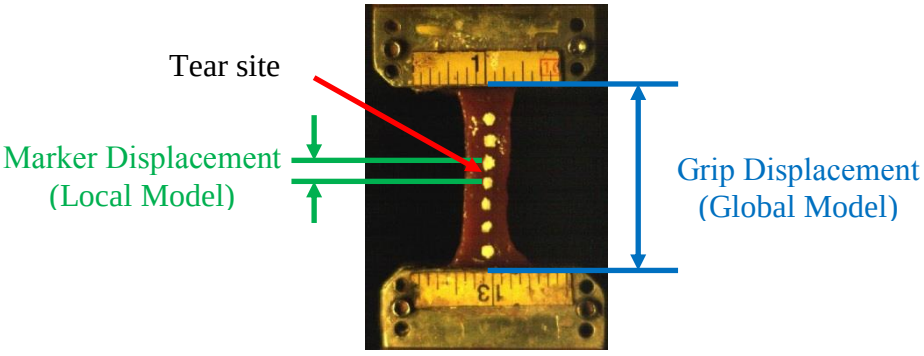

Figure 3.8. An illustration of the local and global models for the stretch ratio calculation.

The stretch ratio (λ) and Green-Lagrangian strain (ε) of LM and GM were then calculated from the curve fit displacement data as follows:

$$\lambda = \frac{L_n}{L_0} \qquad \text{(Eq. 3.7)}$$

$$\varepsilon = \frac{1}{2}(\lambda^2 - 1) \quad \text{(Eq. 3.8)}$$

where L_0 is the initial distance between the optical markers (LM) or the initial distance between grips (GM) (Fig. 3.8). L_n is the instantaneous distance between the optical markers (LM) or instantaneous distance between the grips (GM). The strain rates for LM and GM were calculated as the slope of the time histories of the local strain and global strain, correspondingly from 25% to 75% of the peak strain, which was corresponding to the time of failure [2, 104].

The inertia compensated force (F_{IC}) was calculated based on the measured time histories of force (F), grip acceleration (a), and effective mass (m_{eff}) (Eq. 3.9). The inertial force added by the grip mounting was calculated based on grip acceleration (a), and effective mass (m_{eff}). The effective mass was defined as half of the load cell mass plus the grip mass between the load cell and specimen. This inertial force showed negligible values for the two low strain rates (0.01 s^{-1} and 0.1 s^{-1}), so the measured force was not inertially compensated at these two rates. For the highest rate, 1.0 s^{-1}, the inertial force showed higher levels, but under the level of 5% of the measured force (F). Therefore, in this case the force was inertially compensated (Eq. 3.9). The force (F for 0.01 s^{-1} and 0.1 s^{-1}; F_{IC} for 1.0 s^{-1}) was fit with a 5th degree polynomial up to the time of failure (average R^2 = 0.890) to reduce the inherent measurement noise because it was found that the 5th degree polynomial fitted the force-time curves better than polynomials with other degrees [2, 104].

$$F_{IC} = F - a * m_{eff} \quad \text{(Eq. 3.9)}$$

The 2nd Piola-Kirchhoff (PK) Stress (S) is a symmetric tensor usually employed for characterization of materials with large deformation, and is the energy conjugate of the GL strain tensor. In the case of uniaxial test, the 2nd PK Stress was calculated based on the curve fit force data, the stretch ratio (λ), and initial cross-sectional area (A_0) (Eq. 3.10).

$$S = \frac{F}{\lambda * A_0} \text{ for 0.01 } s^{-1} \text{ and 0.1 } s^{-1}; \; S = \frac{F_{IC}}{\lambda * A_0} \text{ for 1.0 } s^{-1} \quad \text{(Eq. 3.10)}$$

The stress-strain curves were calculated for each test. The failure stress and failure strain were defined as the stress and strain at the time of failure. The average curves and their corresponding variation corridors were calculated for each combination of strain rates and fresh/preservation methods using a normalization technique [89]. This technique begins with a method for averaging specimen stress-strain responses in which curve shape characteristics are maintained and discontinuities are avoided. Individual responses sharing a common characteristic shape are averaged based upon normalized strain values. The normalized average response is then scaled to represent the given data set using the mean peak strain value associated with the set of experimental data. Some applications and justification of this technique were previously published [88, 89]. An elliptical corridor approach was used to account for variability in both stress and strain coordinates along the average curves [88]. The boundaries of the elliptical corridor were obtained as an envelope of the ellipsoids defined along the average curves using 1 standard variation (±1 SD) as ellipsoid axes [88] (Fig. 3.9).

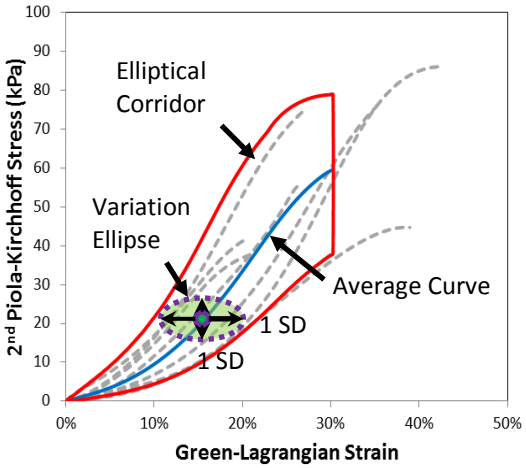

Figure 3.9. An illustration of the development approach of the elliptical corridor. SD: standard deviation.

3.2.2.3. Identification of Material Properties

Many studies have demonstrated that the abdominal tissues can be reasonably approximated as isotropic and incompressible materials [6, 129-131]. In contrast to the QLV modeling of the viscoelastic behaviors using relaxation tests in Section 3.2.1, the hyperelastic formulation has been shown to be a good phenomenological constitutive approach within the nonlinear regime of biological tissues for tensile and compressive tests [132]. This approach postulates the existence of a strain energy function (W), defined as a scalar function per unit reference volume, which depends only on the deformation gradient (F). Several hyperplastic material models, used usually to model isotropic rubberlike materials (e.g. Ogden, Mooney-Rivlin, Blatz-Ko, and Frazer-Nash), were implemented in LS-Dyna FE software v. 6.0 (LSTC, Livermore, CA). A hyperelastic model called the Ogden material model [133], which is frequently used to model soft tissue [129, 130, 134], was utilized for material characterization of liver parenchyma as it demonstrated the closest match to the test data compared to other hyperelastic material models implemented in LS-Dyna v. 971 [88]. The strain energy function of the Ogden incompressible material model [133] is expressed as:

$$W(\lambda_1, \lambda_2, \lambda_3) = \sum_{i=1}^{M} \frac{\mu_i}{\alpha_i}\left(\lambda_1^{\alpha_i} + \lambda_2^{\alpha_i} + \lambda_3^{\alpha_i} - 3\right) \qquad \text{(Eq. 3.11)}$$

where λ_1, λ_2, λ_3 are the principal stretches, M is the order of the Ogden material model, μ_i and α_i are the i^{th} shear modulus and exponent, respectively. In this approach, the specimen was approximated as a beam with an average cross-sectional area and the length as the pre-test distance measured between clamps (GM) or between markers (LM). Therefore, the strain is assumed to be constant along the specimen based on the isotropy and homogenous assumptions. For an isotropic incompressible material with an applied stretch λ_1 along the loading direction, the stretches along the other two orthogonal directions are:

$$\lambda_2 = \lambda_3 = \lambda_1^{-1/2} \qquad \text{(Eq. 3.12)}$$

The strain energy function of a first-order Ogden model (M=1) can therefore be

expressed as:

$$W(\lambda_1) = \frac{\mu_1}{\alpha_1}\left(\lambda_1^{\alpha_1} + 2\lambda_1^{-\alpha_1/2} - 3\right) \quad \text{(Eq. 3.13)}$$

The first (P_1) and second (S_1) PK stresses derived from the strain energy function along the principal directions are expressed as [132]:

$$P_1 = \frac{\partial W}{\partial \lambda_1} = \mu_1\left(\lambda_1^{\alpha_1 - 1} - \lambda_1^{-\alpha_1/2-1}\right) \quad \text{(Eq. 3.14)}$$

$$S_1 = \frac{P_1}{\lambda_1} \quad \text{(Eq. 3.15)}$$

Therefore, the time history of the force predicted by the model in the specimen is:

$$F_m(t) = \lambda_1 S_1(\mu_1, \alpha_1, t) A_0 \quad \text{(Eq. 3.16)}$$

An optimization procedure was employed to identify the material model properties of both fresh and preserved bovine livers. The values of the material model parameters (α_1 and μ_1) were optimized using the active-set algorithm in MATLAB v. R2012b (The MathWorks, Inc., Natick, MA), which tried to minimize the root mean square (RMS) of the differences between the model force to the corresponding test data (F for 0.01 s^{-1} and 0.1 s^{-1}; F_{IC} for 1.0 s^{-1}) (Eq. 3.17).

$$F_{error} = \sqrt{\sum_{i=1}^{n_t}[F_m(t_i) - F(t_i)]^2};\ F_{error} = \sqrt{\sum_{i=1}^{n_t}[F_m(t_i) - F_{IC}(t_i)]^2} \quad \text{(Eq. 3.17)}$$

where t_i is a series of n_t-time sequences equally distributed from the time when the specimen started to be loaded (time 0) up to the time of failure. The initial values of α_1 and μ_1 were chosen as 10 and 5 kPa, respectively [88]. The parameters (α_1 and μ_1) were optimized for each average stress-strain curve of each combination of the three loading rates and three preservation times (fresh, Day 30, and Day 60). The ground-state shear modulus μ can then be determined by [130]:

$$\mu = \frac{\mu_1 \alpha_1}{2} \quad \text{(Eq. 3.18)}$$

3.2.2.4. Statistical Analysis

A series of two-sample Mann–Whitney tests for the difference in median were performed to evaluate significance (α=0.05) in failure stress, failure strain, and optimized material properties between storage times and between loading rates. When comparing the failure properties between local and global stretch ratio data sets, paired two sample t-tests were utilized (α=0.05).

3.3. Results

3.3.1. Indentation Testing on Porcine Livers

Typical viscoelastic behavior of the liver recorded on a specimen during ramp-hold indentation is presented in Fig. 3.10. The average functions $P^e(h)$ and $G(t)$ corresponding to the

two different storage methods are shown in Fig. 3.11. Identified parameters of the QLV material model are provided in Table 3.2. The unpaired two-sample t-test assuming equal variance was conducted on the fresh tissues in the two treatment groups, cooling and freezing, and it was proved that there were no significant differences of the fresh tissues on G_∞ and μ_0 between these two groups ($p>0.05$).

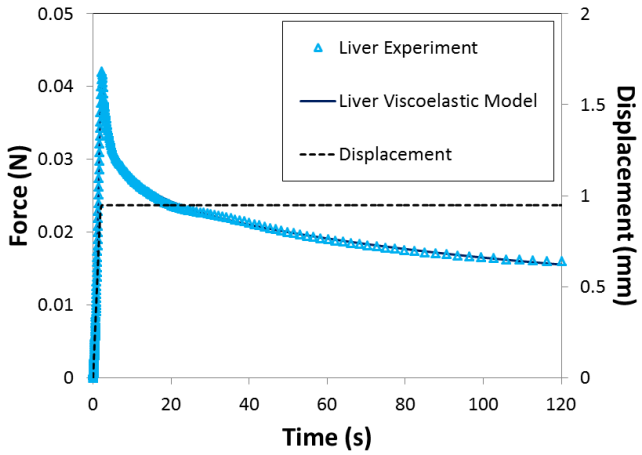

Figure 3.10. Examples of curve fitting with QLV model.

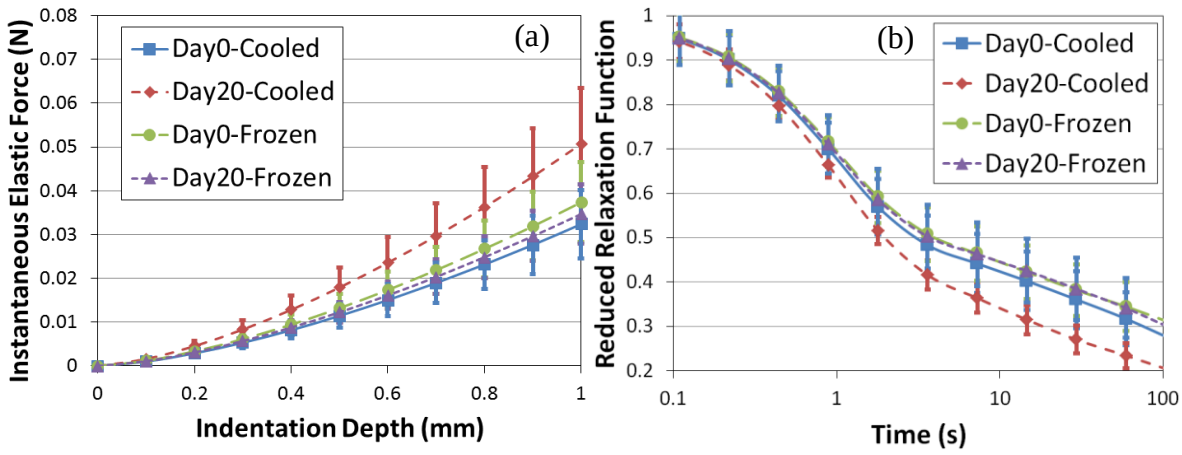

Figure 3.11. (a) Average $\mathbf{P^e(h)}$ for the cooling and freezing storages; (b) Average $\mathbf{G(t)}$ for the cooling and freezing storages. Error bars represent ±1 SD.

Table 3.2. Identified parameters of QLV material model (fresh vs. preserved tissues). The reported values are average±1 SD.

	Cooling		Freezing	
	Fresh	Day 20	Fresh	Day 20
G_∞	0.207±0.059	0.153±0.026	0.256±0.055	0.231±0.066
G_1	0.492±0.042	0.547±0.051	0.462±0.030	0.474±0.038
G_2	0.102±0.026	0.153±0.020	0.122±0.014	0.095±0.041
G_3	0.199±0.060	0.147±0.035	0.160±0.052	0.200±0.065
μ_0 (kPa)	3.406±0.819	5.333±1.349	3.930±0.962	3.651±0.708
R^2	0.796	0.927	0.799	0.809

The comparisons between the fresh and cooled tissues showed that μ_0 was significant increased ($p<0.05$) (Table 3.3). G_∞ was significantly decreased between fresh and cooled tissues ($p<0.05$). For the freezing effect, μ_0 and G_∞ were not significantly changed ($p>0.05$).

Table 3.3. The comparison of fresh and preserved tissues for cooling and freezing storages using the paired two-sample t-test. Each cell represents the average of differences between fresh and preserved tissues of $\boldsymbol{G_\infty}$ and $\boldsymbol{\mu_0}$ and its corresponding p-value in the parentheses.

	Cooling	Freezing
G_∞	**-0.054**	-0.025
	(<.001)	(0.202)
μ_0 (kPa)	**1.927**	-0.280
	(<.001)	(0.129)

* Bolded values represent the significant changes of coefficients ($\alpha=0.05$).

The differences between the cooling and freezing effects were investigated using the GEE statistical approach. μ_0 after cooling was significantly higher by 1.991 kPa compared to that obtained by freezing ($p<0.05$). In addition, G_∞ after cooling was significantly lower (6.7%) than G_∞ after freezing ($p<0.05$).

3.3.2. Tensile Testing on Bovine Livers

A typical force versus time curve recorded on a liver specimen during tensile testing is presented in Fig. 3.12. The averages and elliptical corridors of stress-strain curves by loading rate for fresh, Day 30, and Day 60 specimens are shown in Fig. 3.13. The average strain rates were 0.007 s^{-1}, 0.071 s^{-1}, and 0.684 s^{-1} for LM and 0.009 s^{-1}, 0.091 s^{-1}, and 0.914 s^{-1} for GM for specimens tested at 0.01 s^{-1}, 0.1 s^{-1}, and 1.0 s^{-1}, correspondingly. The data show that the tissue stiffness and failure stress of both LM and GM increased as a result of freezing for all loading rates, while failure strain of both LM and GM decreases. The number of samples in each group is shown in Fig. 3.14a.

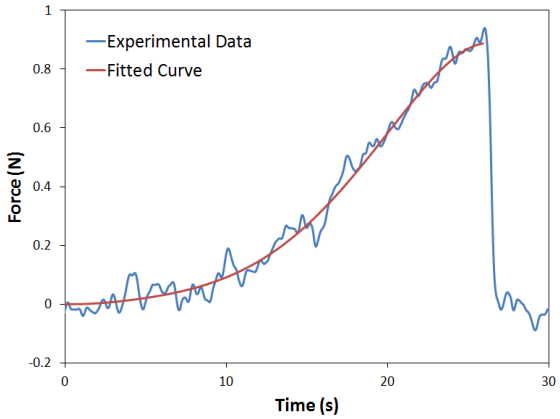

Figure 3.12. An illustration of a typical experimental force-time curve (Rate 1) recorded on a liver specimen during tensile testing and its fitted curve using 5th degree polynomial.

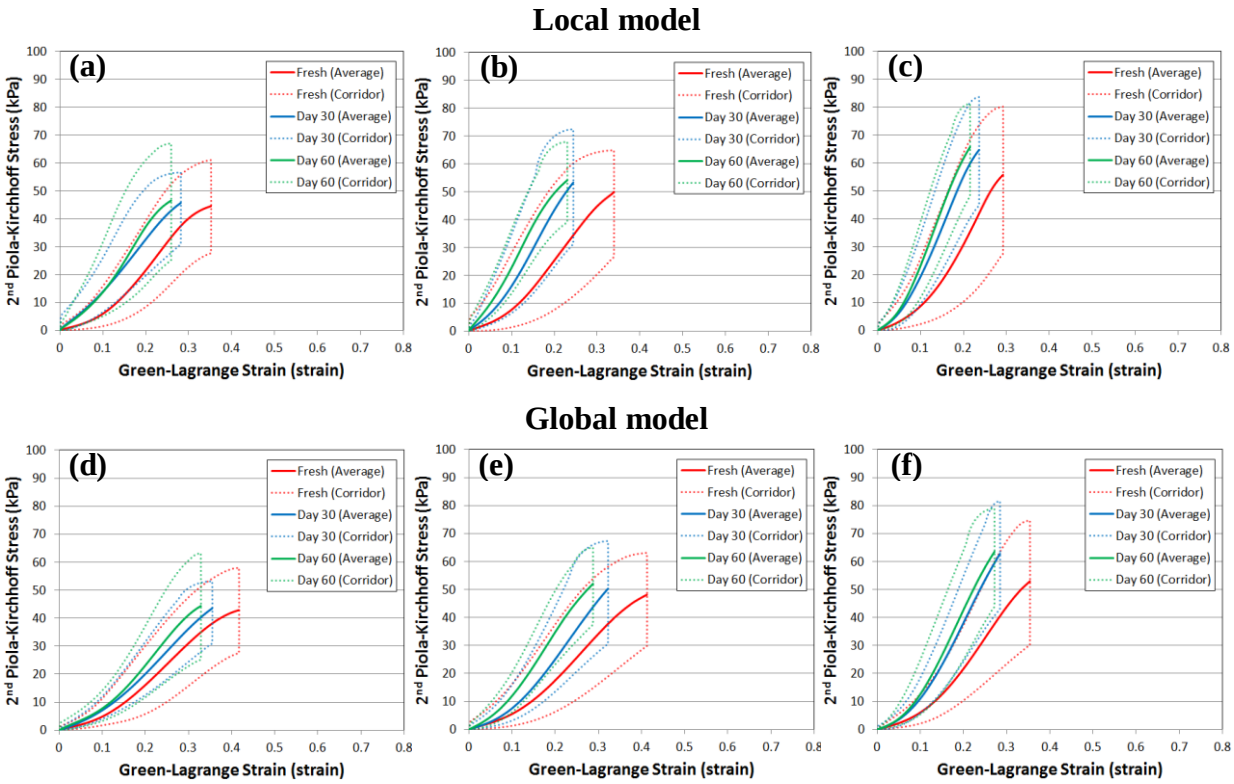

Figure 3.13. Characteristic averages and elliptical corridors of local model for a) 0.01 s^{-1} b) 0.1 s^{-1} c) 1 s^{-1} strain rates and of global model for d) 0.01 s^{-1} e) 0.1 s^{-1} f) 1 s^{-1} strain rates.

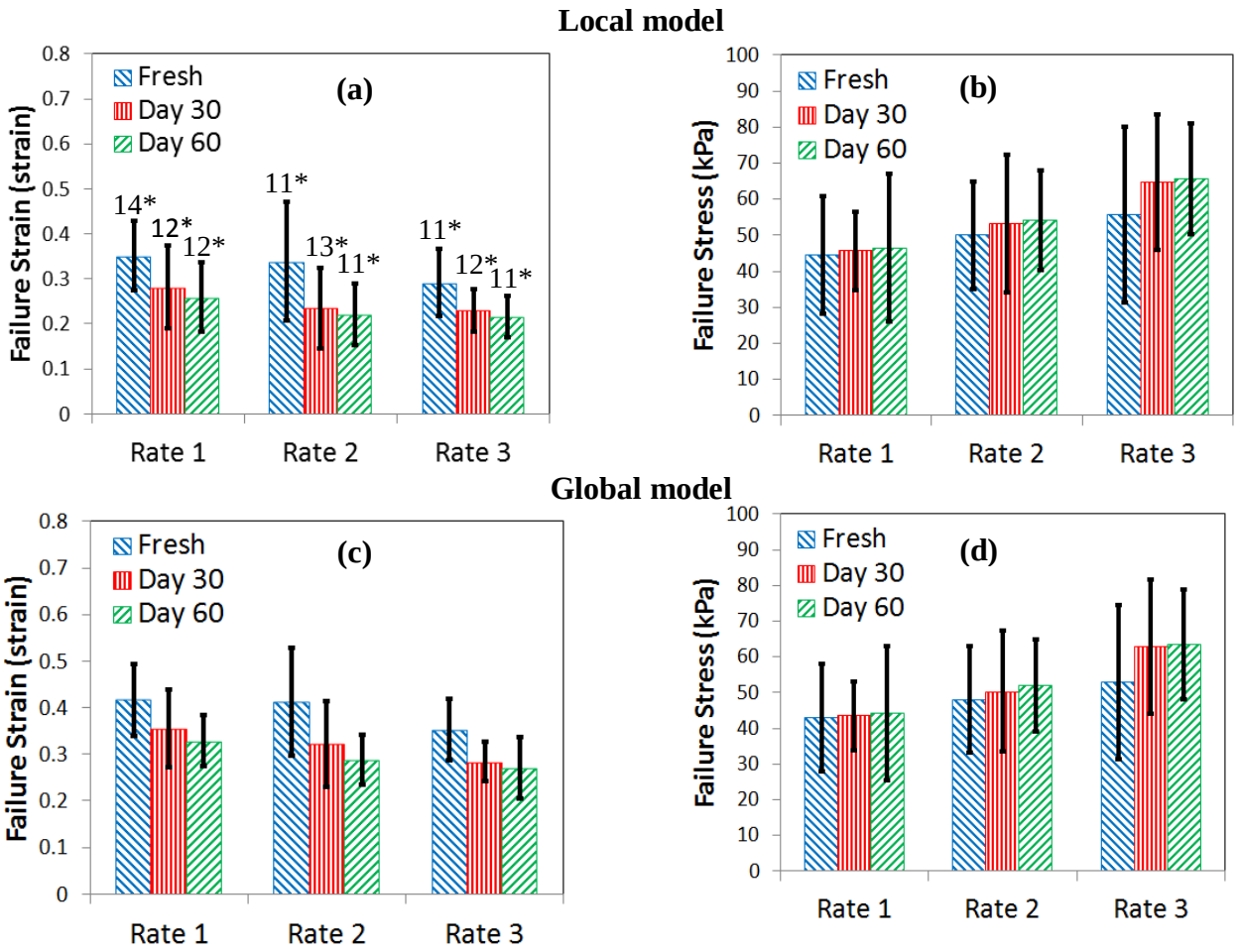

Figure 3.14. Failure stain and failure stress of the fresh and preserved tissues at three loading rates.

The averages and SDs of failure strain and failure stress for both LM and GM are shown by loading rate in Fig. 3.14. The fresh specimens were found to have 17-44% higher failure strains than the Day 30 specimens and 27-50% higher failure strains than Day 60 specimens across all three loading rates for both LM and GM (Fig. 3.14a, 3.14c). The average failure stresses of preserved tissues where found to be larger than the average failure stresses of fresh tissues for both LM and GM (Fig. 3.14b, 3.14d). The comparisons using paired two sample t-tests between LM and GM showed significant differences for all corresponding failure strain pairs and failure stress pairs ($p<0.05$), where the global failure strain was significantly higher and failure stress was significantly lower than the local values.

Statistical comparisons using Mann–Whitney tests showed significant differences in the failure strain between fresh and Day 30 specimens and between fresh and Day 60 specimens ($p<0.05$) for both LM and GM at all three loading rates (Table 3.4). However, the differences in failure strain between Day 30 specimens and Day 60 specimens were not significant ($p>0.05$). In addition, no significant differences were found for failure stress between fresh and preserved specimens or between storage times ($p>0.05$) (Table 3.5).

Table 3.4. Statistical comparison (p-values from Mann-Whitney U-Test) of failure strain between preservation times.

	Rate 1	Rate 2	Rate 3
Comparison	Local/Global	Local/Global	Local/Global
Fresh vs. Day 30	**0.037**/**0.033**	**0.049**/**0.049**	**0.029**/**0.007**
Fresh vs. Day 60	**0.015**/**0.002**	**0.036**/**0.013**	**0.018**/**0.015**
Day 30 vs. Day 60	0.707/0.544	0.772/0.385	0.601/0.559

Note: **Bold**: p-value<0.05.

Table 3.5. Statistical comparison (p-values from Mann-Whitney U-Test) of failure stress between preservation times.

	Rate 1	Rate 2	Rate 3
Comparison	Local/Global	Local/Global	Local/Global
Fresh vs. Day 30	0.898/1.000	0.685/0.772	0.442/0.230
Fresh vs. Day 60	0.857/0.817	0.511/0.599	0.393/0.212
Day 30 vs. Day 60	0.403/0.403	1.000/0.954	0.926/0.878

No significant differences in the failure strain or failure stress were found between loading rates for fresh tissues ($p>0.05$) (Table 3.6-3.7). The only significant changes in preserved specimens were found between Rate 1 and Rate 3 in terms of the failure stress and the failure strain for both LM and GM ($p<0.05$), except the Day 30 and Day 60 specimens for LM.

Table 3.6. Statistical comparison (p-values from Mann-Whitney U-Test) of failure strain between rates.

	Fresh	Day 30	Day 60
Comparison	Local/Global	Local/Global	Local/Global
Rate 1 vs. Rate 2	0.978/1.000	0.201/0.430	0.310/0.091
Rate 1 vs. Rate 3	0.059/0.059	0.157/**0.023**	0.132/**0.039**
Rate 2 vs. Rate 3	0.293/0.131	0.683/0.341	0.743/0.599

Note: **Bold**: p-value<0.05.

Table 3.7. Statistical comparison (p-values from Mann-Whitney U-Test) of failure stress between rates.

	Fresh	Day 30	Day 60
Comparison	Local/Global	Local/Global	Local/Global
Rate 1 vs. Rate 2	0.311/0.338	0.265/0.221	0.148/0.148
Rate 1 vs. Rate 3	0.262/0.239	**0.007**/**0.009**	**0.011**/**0.011**
Rate 2 vs. Rate 3	0.743/0.646	0.165/0.183	0.168/0.237

Note: **Bold**: p-value<0.05.

The optimal material model parameter α_1 ranged from 6.45 to 11.86, and μ_1 ranged from 5.86 to 27.72 kPa (Table 3.8). The ground-state shear modulus μ increased when comparing the preserved tissues to fresh tissues for both LM and GM at all three loading rates. The coefficients of determination (R^2) between the model force and experimental force were greater than 0.95 for all cases, indicating the good model fittings of the Ogden material model (Fig. 3.15).

Table 3.8. The Ogden material model parameters of average stress-strain models for the three loading rates and preservation methods.

	Rate 1 Fresh/Day 30/Day 60	Rate 2 Fresh/Day 30/Day 60	Rate 3 Fresh/Day 30/Day 60
Local			
α_1	8.51/7.52/8.49	9.00/9.72/6.45	11.86/10.44/10.69
μ_1 (kPa)	8.14/14.50/12.92	8.42/12.15/27.72	5.86/13.27/14.69
μ (kPa)	34.64/54.51/54.86	37.90/59.05/89.45	34.78/69.29/78.55
Global			
α_1	7.72/8.93/9.14	8.20/10.46/9.07	10.23/11.37/11.12
μ_1 (kPa)	7.79/6.97/7.55	7.65/6.25/10.95	5.95/7.77/9.00
μ (kPa)	30.10/31.12/34.50	31.36/32.71/49.62	30.43/44.17/50.08

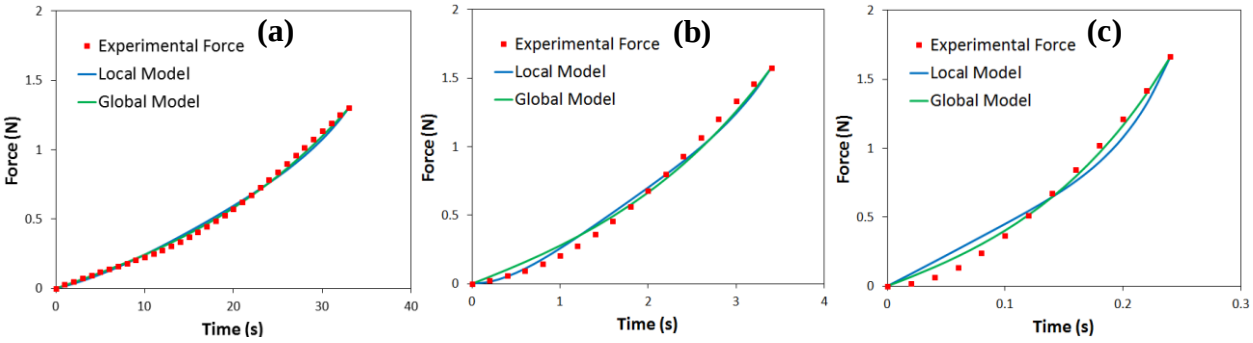

Figure 3.15. Illustrations of the time histories of reaction force of Ogden material model fitting for local and global models: (a) 0.01 s^{-1}; b) 0.1 s^{-1}; c) 1.0 s^{-1} strain rates.

3.4. Discussion

Preservation by cooling and freezing storage showed the cooling effect made the liver stiffer while the freezing effect did not significantly change the instantaneous elastic response (Fig. 3.11a, Table 3.3). Similarly, significant change on the liver's reduced relaxation function was observed by cooling storage, but this effect was not observed on liver specimens preserved by freezing (Fig. 3.11b, Table 3.3). Both the reduced relaxation response and the instantaneous elastic response of the liver were highly sensitive when comparing the cooling to the freezing effects.

Some previous studies reported similar findings to the liver stiffness responses: cooling made the liver stiffer (e.g. bovine [8]) and freezing did not change the properties of the liver (e.g. porcine [7]). During the cooling process, increase of osmolality of the extracellular fluid of livers

could be found, creating an osmotic gradient and causing the cells to dehydrate [135, 136]. This may alter the structure of the liver cells while strengthening the elastic behaviors of the extracellular areas of the liver, leading to the increase of the stiffness of the tissues during the early stage of the cooling process. This result was comparable to those reported by Ocal et al. who tested bovine livers in several pre-selected time points within 48 hours after harvesting [8]. On the other hand, while both extra- and intracellular ice formation could be achieved with fast freezing or freezing to very low temperatures [137], it has been shown that cells may survive freezing and rehydrate after thawing [138-140]. Porcine liver parenchyma exhibits better recovery ability and therefore has no considerable difference in the compressive response of the fresh versus previously frozen samples, as demonstrated in [7]. While the porcine liver properties may not be influenced by the freezing effect in terms of the compressive response, this study showed that any cellular damage that might have been caused by the freezing process had effect on the tensile failure property of bovine livers, as discovered by Santago et al. [10]. In addition, Brunon et al. indicated that the freezing preservation may affect the failure properties of the porcine liver capsule alone [1]. While the current study quantifies only the porcine material properties under the indentation testing, further comparison of the storage methods and the failure properties between different loading types would be suggested.

In general, the mean values of the ratios of the long-time shear modulus (G_∞) to the instantaneous shear modulus (G_0) for fresh porcine livers were close to the values reported in the previous study [141], but some differences were observed as well. The unpaired two-sample t-test assuming unequal variance showed that this ratio for fresh porcine liver obtained in the current study was significantly lower than the ratio obtained in [141] ($p<0.05$) (Fig. 3.16). These discrepancies could be caused by different viscoelastic modeling techniques and number of specimens. Ahn et al. [141] utilized only two time constants (average τ_1=1.136, τ_2=51.204), and small variation of G_∞/G_0 values was observed probably due to the small sample size (3 specimens).

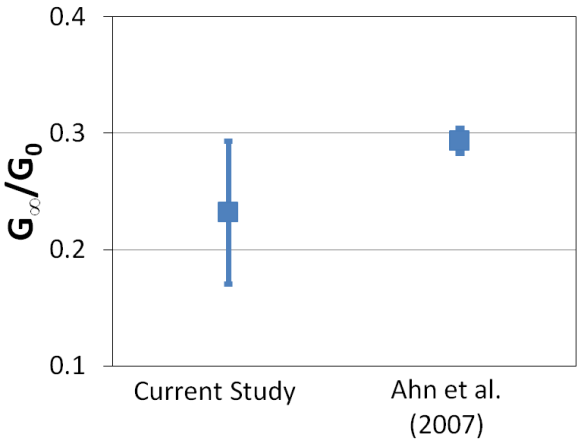

Figure 3.16. Comparison of the shear modulus ratios with published studies for fresh porcine livers.

Similar biomechanical behaviors between human and porcine abdominal organs have been reported in some previous studies (e.g. kidney [105], liver [103], and spleen [142]). In fact,

Vodicka et al. [143] showed that the miniature pig, sharing many physiological similarities with humans, offered several breeding and handling advantages (when compared to non-human primates), making it an optimal species for preclinical experimentation. Thus, the porcine abdominal tissues may serve reasonably as a surrogate of human tissues in some conditions, such as fresh tissues [1]. However, there is a lack of data regarding the comparisons of the tissue properties between different storage conditions among the porcine and human abdominal tissues; therefore, these comparisons could be further investigated for the references of future liver material model development. Furthermore, the obtained material models should be validated and compared with whole body impact/belt loading tests such as oblique impact (Chapter 5).

One assumption in the indentation test is the isotropy of the tissues; however, porcine abdominal organs usually exhibit anisotropic properties. Farshada et al. [144] studied the uniaxial compression behavior of porcine kidney parenchyma sample at various loading speeds and showed that the parenchyma tissue was not only rate dependent, but also anisotropic. In addition, Chui et al. [103] found that with the primary axis perpendicular to the cross sectional surface of porcine liver tissue specimens, the tissue was stiffer with tensile or compressive force in the axial direction compared to that of the transverse direction. Therefore, the investigation of the isotropic behaviors of the abdominal organs under the cooling and freezing effects by indenting different directions on the tissues would be suggested to acquire the full scope of the tissue mechanical responses. In addition, since several studies (e.g. [145]) showed that the mechanical properties of porcine soft tissues are temperature-dependent, additional experiments should be performed to investigate the effect of preservation on abdominal tissues conducted at different temperatures (e.g. body temperature vs. room temperature).

Some limitations were observed in this indentation study. First, specimens with connected outer capsule and inner parenchyma structures were indented, and the capsule side was loaded rather than the parenchyma side, as shown in other studies testing on porcine abdominal tissues [103, 146, 147]. However, some previous studies have shown the different material properties of the capsule and parenchyma [103, 106, 121, 147]. Therefore, the effects of degradation over time may be underestimated through the indentation tests because the capsule is much stronger and more resilient than the parenchyma for the abdominal tissues due to the collagen structure of the capsule, so its properties may not be changed largely by the cooling and freezing effects in comparison with the parenchyma. Testing these structures individually will be desirable and the results can be more accurate to individually model the mechanical behavior of abdominal organ components (e.g. in FE models). In addition, the indentation-based properties may be within the toe region of the entire stress-strain curve of the human liver. Additional tests (e.g. tension and compression) incorporating the effects of preservation methods in the domain of higher strains would help to better understand the tissue behavior in the failure region.

For the tensile testing in the current study, the failure strains of previously frozen bovine liver parenchyma were significantly different ($p<0.05$) from those of fresh liver parenchyma under tensile loading. Therefore, preservation by means of freezing resulted in an increase in liver parenchyma stiffness. Significant differences between previously frozen bovine liver tissue and fresh bovine liver tissue have also been reported by previous studies [1, 8, 10]. In addition, the failure properties and material model parameters were found to change with respect to the duration of frozen storage time. While no histology study was conducted for the tested

specimens in the current study, these observations can potentially be explained by the state of the cellular composition and architecture of the bovine liver tissue during the freezing and thawing processes. Extra- cellular and intra-cellular ice formation can be achieved by freezing the hepatic tissue to low temperatures [137]. Therefore, during freezing the expansion of the fluid and formation of irregularly shaped ice particles may damage the cell membranes of bovine livers and the connective tissue which binds the cells together, leading to a reduction in failure strain [1, 8, 10].

Although some studies have investigated the effect of freezing on liver tissues, conclusions regarding the effect of freezing on the material response of liver tissues varied between studies. A summary of various studies related to the comparison between fresh and frozen liver tissues is shown in Table 3.9. As can be observed, the majority of studies performed on porcine livers have reported that the material properties of porcine liver are not affected by the freezing process. Conversely, the properties of the bovine liver tissue have consistently been shown to be affected by the process of freezing in both tensile and compressive loading. This discrepancy could potentially be explained by the differences of the cellular architecture between porcine liver parenchyma and human/bovine liver parenchyma. Specifically, the lobules of porcine liver parenchyma are separated by relatively thick layers of collagenous septum, while the lobules of human and bovine liver are not [148-151]. This accounts for the tougher nature of porcine liver compared to bovine liver [151]. In addition, the majority of the porcine studies were performed with the capsule attached to the parenchyma. Tamura et al. [7] is the only study which quantified the effect of freezing on the compressive properties of isolated porcine liver parenchyma. Tamura et al. [7] concluded that freezing does not affect the compressive repose of porcine liver parenchyma based on the response of matched specimens after 5 cycles of sub-failure preconditioning. However, it is possible that the compressive material properties of liver parenchyma are not as sensitive to the effects of freezing as the tensile material properties since the mechanics of compressing cells together are fundamentally different than the mechanics of pulling cells apart. Overall, based on the summary and comparison of the various studies which have investigated the effect of freezing on liver tissues, it is reasonable to conclude that while porcine liver material properties are generally unaffected by the process of freezing, the tensile and compressive material properties of bovine liver parenchyma are significantly affected by the process of freezing.

Table 3.9. Comparison of the freezing effect on liver tissues between studies.

Study	Source	Type	Loading	Specimen	Comparison	Effect of Freezing
Brunon et al. [1]	Human	Tension	$0.001\ s^{-1}$-$0.01\ s^{-1}$	Capsule+Parenchyma	Fresh, 24 hr	No
Brunon et al. [1]	Porcine	Tension	$0.001\ s^{-1}$-$0.01\ s^{-1}$	Capsule+Parenchyma	Fresh, 24 hr	Yes
Current Study	Porcine	Indentation	0.5 mm/s	Capsule+Parenchyma	Fresh, Day 20	No
Nguyen et al. [6]	Porcine	Tension	$0.08\ s^{-1}$	Capsule+Parenchyma	Fresh, 48hr	No
Tamura et al. [7]	Porcine	Compression	0.5 mm/s	Parenchyma	Fresh, 24 hr	No
Ocal et al. [8, 9]	Bovine	Compression	48 mm/s	Parenchyma	Fresh, 1hr-48hr	Yes
Santago et al. [9, 10]	Bovine	Tension	$0.07\ s^{-1}$	Parenchyma	Fresh, Day 26	Yes
Current Study	Bovine	Tension	$0.01\ s^{-1}$, $0.1\ s^{-1}$, $1.0\ s^{-1}$	Parenchyma	Fresh, Day 30, Day 60	Yes

With respect to loading rate, the failure strain significantly decreased while the failure stress significantly increased with increased loading rate for previously frozen tissues ($p<0.05$).

However, there were no statistically significant differences found for fresh tissues with respect to loading rate ($p>0.05$). This is consistent with the finding of Kemper at al. [2], who reported that while the tensile failure stress and failure strain of fresh human liver parenchyma increased with respect to loading rate there were not significant differences between loading rates of approximately $0.01s^{-1}$, $0.1\ s^{-1}$, and $1\ s^{-1}$. However, Kemper at al. [2] did report that the tensile failure stress significantly increased and the failure strain significantly decreased between loading rates of $0.01s^{-1}$ and $10.0s^{-1}$. In addition, the comparisons of failure strain and failure stress between the fresh bovine liver parenchyma in the current study and fresh human liver parenchyma in the study conducted by Kemper et al. [2] using Mann–Whitney tests showed no significant differences ($p>0.05$) for all three loading rates (Chapter 4, Fig. 4.7), which is consistent with the findings of Kemper et al. [2]. Therefore, bovine liver tissues may serve as a reasonable surrogate for human liver tissues when investigating the tensile mechanical properties at various loading rates ($0.01\ s^{-1}$-$1.0\ s^{-1}$).

Although there were some observed differences in the failure stress and failure strain between the local and global models (LM and GM), the tissue preservation and rate-dependency comparisons showed the same effect on the changes in the failure properties for both models. As in a previous study [88], significantly larger failure strains and lower failure stresses were observed in the global model compared to the local model for all three loading rates and preservation scenarios ($p<0.05$). These differences could be caused by the inhomogeneity of the tissue material properties or irregularity of the cross-sectional areas within the gage length. However, it is more likely that the majority of differences between the local and global models are due to the fact that the local model does not account for the variation in cross-sectional area outside of the gage length (i.e. the fillets between the gage length and grip area), or the complex state of stress in the fillet area due to the compressive stress imposed on the tissue by the grips.

In the current study, the isolated specimens of liver parenchyma of the liver were tested without the liver capsule attached, which is similar to other studies performed on bovine liver tissue [2, 10, 152]. However, some previous studies using bovine liver have shown that the material properties of the capsule are different than that of the parenchyma [88, 119]. The hepatic capsule surrounding the liver is composed of a tough fibrous layer enriched with collagen and elastin. It was reported that a decomposition of elastin during the periods of thawing at room temperature could change the stiffness of the tissue, making the organ more rigid [105, 108, 153]. Therefore, future studies should be performed to evaluate the effect of different storage conditions on the material properties of the capsule surrounding the liver. The results from such a study would allow the mechanical behavior of capsule and parenchyma to be modeled individually, which may lead to more biofidelic computational models (e.g. in FE models) of the liver as a whole. In addition, the rate dependency of liver parenchyma could be implemented in FE models using a new LS-Dyna material model (MAT_181) [154] (Chapter 5), which employs a tabulated formulation of hyper-elasticity with rate effects [88, 152]. In the future, these data may be used in FE simulations to investigate the differences in global behavior of fresh and preserved PMHS.

As with any study of material properties of soft tissues, this study has some limitations on the tensile testing of bovine livers. First, both GM and LM models assumed constant cross-sectional area (A_0) which means a constant strain distribution along the tissue. A more delicate

approach called specimen-specific FE modeling, utilizing the original shapes of the dog-bone specimens, could be applied to obtain more accurate model parameters [88, 129, 130, 134] (Chapter 4). In addition, while the current study has evaluated the effect of different frozen storage times relative to fresh tissue, there is a lack of data regarding the effect of different storage conditions (e.g. storage temperatures) on the mechanical properties of bovine and human abdominal tissues in tensile loading [128], and these are suggested to be investigated in the future.

All "dog bone shaped" specimens were cut using a template stamp of known shape; however, their shapes prior testing were slightly different mainly due to the gravity. Several non-invasive methods (e.g. elastography) have been applied during *in vivo* tests, primarily for the detection of liver fibrosis in patients [155, 156], and the values of shear modulus reported by these studies (2-6 kPa) were different from the corresponding data reported from mechanical *in vitro* testing [157]. These differences could be associated with the approximations of the liver tissue used to solve the shear wave equation (e.g. purely elastic, isotropic, infinite, and homogenous) [157] and with the different environmental conditions (e.g. *in vivo, in situ*, and *ex vivo*). In addition, these *in vivo* methods only generate finite strains in the liver tissue, which are likely well within the toe region of the stress-strain curve. Therefore, more effort should be placed on improving the understanding of *in vivo* liver properties in order to improve the biofidelity of liver material models.

This chapter shows that the cooling effect impacted the instantaneous elastic response and relaxation response for porcine liver. Statistical analysis found that there were significant differences on the material properties of the porcine liver between cooling and freezing methods. In addition, the current study quantified the material and failure response of fresh and preserved bovine liver parenchyma specimens in tensile loading at various strain rates. Significant changes in the failure strain were observed between previously frozen bovine liver parenchyma samples and fresh samples at both global and local levels ($p<0.05$). Nonlinear and viscoelastic characteristics of the bovine liver parenchyma were observed for both fresh and preserved samples. Specifically, with increased loading rate the failure strain of preserved bovine liver specimens decreased while the failure stress increased. Although fresh bovine liver specimens demonstrated a similar trend with respect to loading rate, the changes in the failure stress and strain of fresh tissues were not significant for various loading rates evaluated in the current study ($p>0.05$). These material properties could be further combined with FE simulations to generate a better understanding of the effect of these material changes on the results of PMHS tests under abdominal loading. It is believed that with continued development of abdominal organ material models, such as applying the methodologies in the current study to human tissues (Chapter 4), will lead to improve whole body FE models that will aid in the mitigation of abdominal injuries resulting from blunt trauma.

Chapter 4

Material Model Identification of Human Liver Parenchyma under Tensile Loading

4.1. Introduction

Material testing on human livers has been widely reported by several previous studies [2, 158, 159]. However, most of these studies focus only on the failure properties, and the identification of a FE material model for liver parenchyma was rarely attempted. In addition, the inherent variations of the material model parameters of the human liver have not been reported. Therefore, to better assess the risk of automotive related injuries on abdominal organs using FE simulations, comprehensive human material models and injury levels are required.

Numerous tests have been performed at low level tensile strains on specimens of liver parenchyma for surgical robot control systems and surgeon training systems based on the virtual reality techniques [103, 146, 160, 161]. Several studies have also investigated the failure properties of liver parenchyma in uniaxial tension [1, 2, 10, 162-164]. An average stress-strain curve and failure data obtained on rabbit livers have been reported [162], but no loading rate information were provided. The failure data recorded on porcine specimens at four different strain rates have also been reported [163]. To characterize the tissue viscoelasticity under a large frequency range, oscillatory shear tests [165-168], impact hammer tests [169], and indentation tests [128, 170, 171] have been performed on liver tissues as well. Recently, an extensive study presented the results of a total of 51 tension tests performed on human liver parenchyma at four loading rates [2]. The stress-strain curves until failure were obtained using optical markers placed on the specimens. Although these studies provide considerable insights regarding the tensile response of liver parenchyma, usually only regional (local) properties (e.g. based on optical marker displacements) have been reported. In addition, an implementation of test data of human liver parenchyma into a FE material model is lacking.

The material characterization of bovine liver parenchyma under tensile loading was recently investigated [88]. In this study, it was demonstrated that the properties obtained from the marker data analysis (optical marker tracking) do not always accurately represent the force response of the whole samples under tensile loading probably due to non-constant strain distribution between markers [161], tissue inhomogeneity, and/or measurement errors. Therefore, in addition to the marker data analysis, the FE-based optimization analysis was also employed in this chapter.

One previous study [164] found no statistically significant changes in failure tensile stress or strain between liver specimens tested at normal room temperature (24°C) and body temperature (37°C). Therefore, in the current study, the human liver specimens were tested at a temperature close to a normal room temperature (24°C) under fresh condition (within 48 hours of death) to minimize the effects of tissue degradation (Chapter 3 and [5, 10, 128]).

The objective in this chapter was to investigate the material properties of human liver parenchyma under a wide range of loading rates. The effects of preservation on the liver material properties under different types of loading schemes have been shown in Chapter 3. Therefore, to avoid possible degradation of the tissues after post mortem, the human livers were all tested under fresh conditions in this chapter. A FE-based optimization analysis similar to a few recent studies [88, 129, 130] was proposed to identify the material parameters of the human liver using specimen-specific FE models and optimization algorithms, assuming homogeneity and isotropy of the tissue. The average stress-strain curves and failure data were then used to determine the mean and SD of material parameters through a stochastic optimization process.

4.2. Methodology

4.2.1. Specimen Preparation and Testing Procedure

Uniaxial tensile tests were performed on the parenchyma of un-embalmed, fresh human livers from five donors within 48 hours after post mortem (Table 4.1). All donors were screened to avoid any medical issues that might affect the mechanical properties of the liver such as hepatitis and abdominal cancer. To preserve the tissue between the time of procurement and specimen preparation, the livers were cooled (without freezing) with wet ice and immersed in a bath of Dulbecco's Modified Eagle Medium (DMEM) to maintain specimen hydration.

The coupon sample preparation and experimental setup for the fresh human liver tensile testing were the same with the procedures for the bovine livers described in Chapter 3 (Section 3.2.2.2).

Table 4.1. Subject information.

Subject ID	Gender (M/F)	Age (years)	Weight (kg)	Stature (cm)
1	M	79	45.4	162.6
2	M	79	81.6	182.9
3	M	76	83.9	172.7
4	M	76	91.0	180.3
5	F	63	60.8	160.0

Prior to each test, the 3D geometry of each specimen mounted in clamps was obtained using the FARO Laser ScanArm (Laser Line Probe V3, FARO Technologies, Inc., Lake Mary, Florida) with an accuracy of ±35 μm. The specimen was scanned from different angles in order to acquire a cloud of points which can reasonably approximate the whole tissue surface. A poly-surface developed through the point cloud using Geomagic Studio 2012 (Geomagic, Inc, Morrisville, NC) was then transformed into a Non-Uniform Rational B-spline (NURBS) surface using Rhino v. 5.0 (Robert McNeel & Associates, Seattle, WA).

Specimens were divided randomly into four sets, which were tested until failure at the following four strain rates: 0.01 s^{-1}, 0.1 s^{-1}, 1.0 s^{-1}, and 10.0 s^{-1} (Table 4.2). The force-time and

displacement-time histories were recorded during each test. In all tests reported in this study, the failure location was in the gage region of the specimen.

Table 4.2. Data acquisition and video sampling rates by loading rate.

Rate	Desired Strain Rate (s^{-1})	Data Acquisition (kHz)	Video (Hz)
Rate 1	0.01	0.2	20
Rate 2	0.1	2.0	70
Rate 3	1.0	20.0	500
Rate 4	10.0	40.0	1000

The inertia compensated force (F_{IC}) was calculated based on the measured time histories of force (F), grip acceleration (a), and effective mass (m_{eff}) for the two higher rates (1.0 s^{-1}, and 10.0 s^{-1}) (Eq. 4.1). The force (F for 0.01 s^{-1} and 0.1 s^{-1}; F_{IC} for 1.0 s^{-1}, and 10.0 s^{-1}) was fit with a 5th degree polynomial up to the time of failure (average R^2= 0.882) to reduce the inherent measurement noise.

$$F_{IC} = F - a * m_{eff} \quad \text{(Eq. 4.1)}$$

4.2.2. Identification of Material Properties

Since the specimen geometries are inherently irregular in cross-sectional area and length, the accuracy of the material identification process depends also on how well the model approximates the geometry of the specimen. Two approaches were attempted in this chapter to identify the material properties (Fig. 4.1). First, the marker data analysis that utilized the cross-sectional area and the displacement of two markers closest to the failure site was used to obtain the stress-strain behaviors and failure properties of the human liver [2, 104]. The failure properties were then compared to previous published data [2] in order to verify the testing protocols used in the current study. Second, specimen-specific FE models were used to determine the material model parameters using a FE-based optimization approach. In FE simulations, a nearly incompressible material model (MAT_77_O in LS-Dyna v. 6.0 [154]) was assigned to the liver parenchyma model. More details about the two approaches used for material model identification are explained in the following sections.

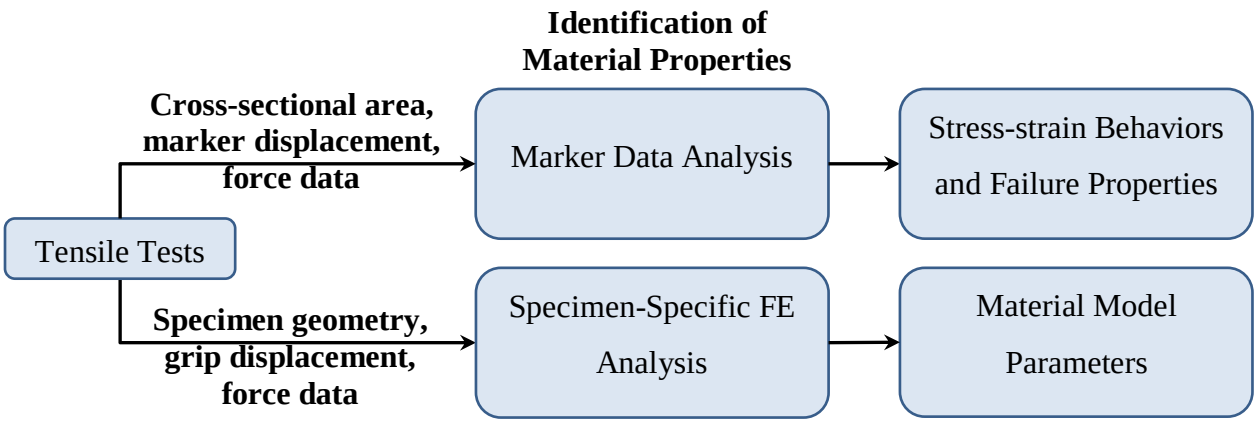

Figure 4.1. Schematic of material identification process.

4.2.2.1. Marker Data Analysis

The methodology of the marker data analysis is consistent with that used in Chapter 3 for bovine liver tensile testing (Section 3.2.2.3). Key formulas were restated here.

The stretch ratio (λ) and Green-Lagrangian strain (ε) were calculated from the curve fit displacement data as follows:

$$\lambda = \frac{L_n}{L_0} \quad \text{(Eq. 4.2)}$$

$$\varepsilon = \frac{1}{2}(\lambda^2 - 1) \quad \text{(Eq. 4.3)}$$

where L_0 is the initial distance between the optical markers spanning the tear site, and L_n is the instantaneous distance between the optical markers. The strain rates were calculated as the slope of the time histories of the strain from 25% to 75% of the peak strain, which corresponds to the time of failure [2, 104].

The 2nd Piola-Kirchhoff (PK) Stress (S) was calculated based on the curve fit measured force data F (for strain rates: 0.01 s^{-1} and 0.1 s^{-1}) or inertia compensated force data (F_{IC}) (for strain rates: 1.0 s^{-1}, and 10.0 s^{-1}), the stretch ratio (λ), and initial cross-sectional area (A_0) (Eq. 4.4). The initial cross-sectional area at the region of the tear was quantified from pre-test pictures.

$$S = \frac{F}{\lambda * A_0} \text{ for 0.01 } s^{-1} \text{ and 0.1 } s^{-1}; \; S = \frac{F_{IC}}{\lambda * A_0} \text{ for 1.0 } s^{-1} \text{ and 10.0 } s^{-1} \quad \text{(Eq. 4.4)}$$

The stress-strain curves were then calculated for each test. The failure stress and failure strain were defined as the stress and strain at the time of failure. Two-way analysis of variance (ANOVA) for testing the effects of strain rates and donors on the mean of the failure stress and failure strain was conducted (α=0.05). Tukey-Kramer multiple comparison tests were then performed to identify significant differences between strain rates and between donors (α=0.05). In addition, a series of two-sample Mann–Whitney tests [172] for the difference in median were

performed to evaluate statistical significance (α=0.05) in failure stress and failure strain between the data in the current study and previous published data [2].

It should be mentioned that through the marker data analysis, the material properties close to the tear site were determined. One previous study [88] showed that these regional properties incorporated in specimen-specific FE models do not always predict reasonably the stiffness behavior of tissue during tensile tests. Therefore, an identification of whole specimen material properties was performed, as it is explained in the following section.

4.2.2.2. Specimen-specific FE Analysis

Specimen-specific FE analysis involves the parameter identification of each specimen using a FE-based optimization approach and experimental data, assuming that the human livers were isotropic and incompressible materials [129, 130]. The Ogden material model, used in bovine liver material model identification in Chapter 3, was chosen for parameter identification of all human liver specimens.

The displacement between the grips was measured during tests using potentiometers attached to the linear stages and then fitted with a 1st degree polynomial to reduce the measurement noise. Two steps were conducted in this study to identify the parameters (μ_1 and α_1) of the Ogden material model [88] for each strain rate: 1) analytical-based optimization approach and 2) FE-based optimization approach.

The analytical-based optimization approach was implemented to obtain the initial guess of Ogden material model parameters for the FE-based optimization approach. This analytical-based optimization approach had the same procedures used for the bovine liver material identification in Chapter 3 (Section 3.2.2.3). Key formulas were restated here.

The strain energy function of a first-order Ogden material model is:

$$W(\lambda_1) = \frac{\mu_1}{\alpha_1}\left(\lambda_1^{\alpha_1} + 2\lambda_1^{-\alpha_1/2} - 3\right) \quad \text{(Eq. 4.5)}$$

The first PK stress P_1 and the second PK stress S_1 are given by:

$$P_1 = \frac{\partial W}{\partial \lambda_1} = \mu_1\left(\lambda_1^{\alpha_1 - 1} - \lambda_1^{-\alpha_1/2-1}\right) \quad \text{(Eq. 4.6)}$$

$$S_1 = \frac{P_1}{\lambda_1} \quad \text{(Eq. 4.7)}$$

Therefore, the time history of the force predicted by the model is:

$$F_m(t) = P_1(\mu_1, \alpha_1, t)A_0 \quad \text{(Eq. 4.8)}$$

To be consistent, the cross-sectional area (A_0) was calculated as the average of cross-sectional areas at three locations: the middle location and other 2 locations about 3 mm up and down from the middle location, from pre-test pictures.

The values of the material model parameters (α_1 and μ_1) were optimized using the active-

set algorithm in MATLAB v. R2012b (The MathWorks, Inc., Natick, MA), which tried to minimize the root mean square (RMS) of the differences between the model force (F_m) to the corresponding test data (Eq. 4.9).

$$F_{error} = \sqrt{\sum_{i=1}^{n_t}[F_m(t_i) - F(t_i)]^2} \text{ for strain rates: 0.01 s}^{-1} \text{ and 0.1 s}^{-1};$$

$$F_{error} = \sqrt{\sum_{i=1}^{n_t}[F_m(t_i) - F_{IC}(t_i)]^2} \text{ for strain rates: 1.0 s}^{-1} \text{ and 10.0 s}^{-1} \quad \text{(Eq. 4.9)}$$

where t_i is a series of n_t-time sequences equally distributed from the time when the specimen started to be loaded (time 0) up to the time of failure. The initial values of α_1 and μ_1 were chosen as 10 and 5 kPa, respectively [88].

The FE-based optimization approach employs specimen-specific FE simulations to identify the material model parameters using the displacement data measured at grip locations as the input (Fig. 4.2c). Specimen-specific FE models were developed using a structural meshing approach in TrueGrid v. 2.3.4 (XYZ Scientific Applications, Livermore, CA). This meshing technique consists of filling the solid object with cubic blocks (the mesh topology, Fig. 4.2a) and then projecting the boundaries to the object surface. A uniform smoothing algorithm [173] was used to automatically improve the mesh quality of hexahedral elements.

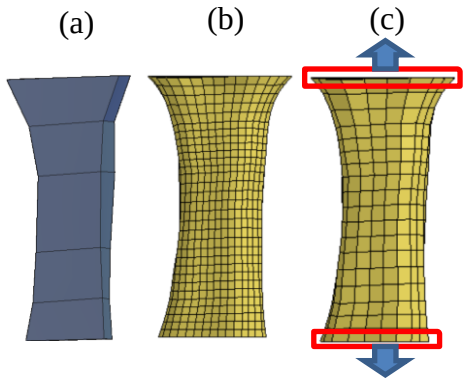

Figure 4.2. Illustration of the specimen-specific FE model: (a) mesh topology; (b) intermediate FE model (1,550 elements); (c) final FE model (360 elements) with boundary conditions.

The implementation of the strain energy function for Ogden material model in the FE software, LS-Dyna v. 6.0, has an unconstrained form that adds a hydrostatic work term to the strain energy functional (MAT_77_O, LS-Dyna Manual [154]):

$$W(\lambda_1, \lambda_2, \lambda_3) = \sum_{i=1}^{N_o} \frac{\mu_i}{\alpha_i}\left(\lambda_1^{\alpha_i} + \lambda_2^{\alpha_i} + \lambda_3^{\alpha_i} - 3\right) + K(J - 1 - lnJ) \quad \text{(Eq. 4.10)}$$

where K is the bulk modulus and J is the volume ratio. As can be observed, this approximated incompressibility formulation (Eq. 4.10) is slightly different than the incompressibility formulation of the theoretical model (Eq. 3.11). The liver parenchyma was assumed as a nearly incompressible material, with a Poisson's ratio of 0.4996 in all models.

For the tests performed at 0.01 s^{-1} and 0.1 s^{-1} loading rates, implicit FE simulations with a fully integrated element integration scheme were employed. To reduce the computational load, an explicit FE approach [154] was used in the simulations of tests performed at higher rates (1.0 s^{-1} and 10.0 s^{-1}). A constant stress element formulation, frequently applied in explicit simulations, was employed to simulate all high rate tests (1.0 s^{-1} and 10.0 s^{-1}). To avoid the occurrence of hourglass (zero-energy) modes, a viscosity-based hourglass control (Q_m= 0.02) was applied in all explicit simulations [154]. To ensure that no additional stiffness was added to the model from the energy induced by hourglass method, a simulation was considered successful if the peak hourglass energy was under 3% of the peak internal (deformation) energy.

A convergence study of mesh density was performed by varying the mesh density of specimen-specific FE models (Fig. 4.2b and 4.2c) for one liver model. The specimen-specific FE models were used to simulate a tensile test by prescribing the displacement-time histories recorded in testing to the specimen ends (Fig. 4.2c). The time histories of tensile force were calculated using cross-sections through the model elements defined at the specimen ends.

The material parameters (μ_1, α_1) calculated from the analytical-based optimization approach were considered as input variables, and the RMS of forces between the test data and corresponding model data was defined as the objective function to be minimized (Eq. 4.9). The successive response-surface methodology (SRSM), an iterative statistical optimization method implemented in LS-Opt v. 4.2 (LSTC, Livermore, CA), was used to find a set of parameters which minimized the objective function. A D-optimal design was used to search the test points around the optimum point determined after each iteration and a quadratic response surface was fit through the values of objective function calculated from FE simulations [100]. The FE optimization process was stopped after 6 iterations. The optimized material model parameters from the FE-based optimization approach were used to calculate the ground-state shear modulus μ [130]:

$$\mu = \frac{\mu_1 \alpha_1}{2} \qquad \text{(Eq. 4.11)}$$

4.2.3. Stress-Strain Curve Average and Variation Corridor

The 2nd PK stress-GL strain curves were calculated using Eq. 4.6 and Eq. 4.7, based on the Ogden material parameters, μ_1 and α_1, obtained from Specimen-Specific FE analysis. For each specimen, the end (failure) point of the stress-strain curve was determined based on the maximum GL strain (ε_f) extracted from the FE simulation of the specimen-specific FE models with optimized Ogden model parameters at the time of failure (end of the simulation). Then, the average curves and their corresponding elliptical corridors were calculated for each strain rate using the same normalization technique as used in Section 3.2.2.2 [88]. The Ogden model parameters of the average curve, denoted as (μ_1^*, α_1^*), were then identified using the same methodology employed for material identification of each specimen by analytical-based optimization approach.

4.2.4. Stochastic Optimization

After stress-strain corridors ("test" corridors) were determined for each loading rate, a stochastic optimization was performed to calculate the SD of the model parameters $(\mu_{1SD}^*, \alpha_{1SD}^*)$

(Fig. 4.3). Since the reduced number of stress-strain curves may influence their statistical values, an iterative adjustment process of their values was performed. In this process, three parameters, μ_{1SD}, α_{1SD}, and ε_{fSD} (the SD of the failure GL strain), were assumed mutually independent, and their values were identified by optimization. First, a set of parameters, (μ_1^S, α_1^S) where S=1,...,N_{opt} (N_{opt} was chosen as 1000 in this study), was generated using (μ_1^*, α_1^*) and their assumed SD $(\mu_{1SD}, \alpha_{1SD})$. A Latin Hypercube Sampling (LHS) approach was employed with the initial values of α_{1SD} and μ_{1SD} chosen as 0.5 and 1 kPa, respectively. Then, a set of failure GL strain values (ε_f^S), coupled with each S in the set (μ_1^S, α_1^S), was determined from a normal distribution with the mean failure GL strain (ε_f^*) calculated from the FE simulations of the specimen-specific models by rates and their assumed SD (ε_{fSD}). The initial SD of the failure GL strain was calculated based on the failure GL strains (ε_f) of specimens extracted from the FE simulations of the specimen-specific models at the time of failure. The stress-strain curves corresponding to this set $(\mu_1^S, \alpha_1^S, \varepsilon_f^S)$ were generated using Eq. 4.6 and Eq. 4.7, and then the elliptical corridor of the new stress-strain curves, which is called "simulation corridor", was calculated. Finally, the "simulation corridor" was compared to the "test corridor", and the active-set optimization algorithm in MATLAB v. R2012b (The MathWorks, Inc., Natick, MA) was used to minimize the RMS between the curves of "simulation" and "test" corridors. Thus, the optimized SD values of the Ogden model parameters $(\mu_{1SD}^*, \alpha_{1SD}^*)$ and the failure GL strain value (ε_{fSD}^*) were reported as statistical parameters of the material model of human liver parenchyma.

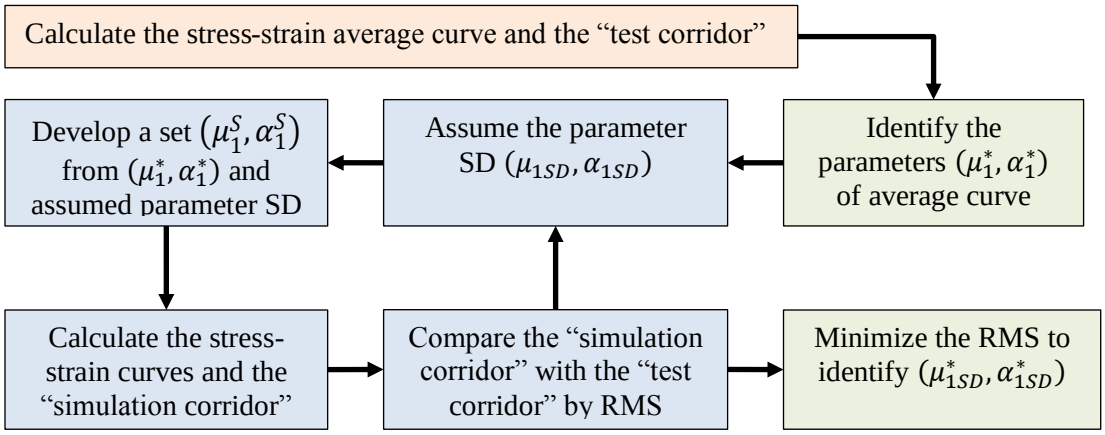

Figure 4.3. Schematic diagram of the development of the stochastic material model.

4.3. Results

4.3.1. Marker Data Analysis

A typical uniaxial test until failure is shown in Fig. 4.4. The stress-strain curves by loading rate obtained from 79 tensile testing specimens are shown in Fig. 4.5. The calculated average strain rates were 0.009 s^{-1}, 0.083 s^{-1}, 0.837 s^{-1}, and 9.541 s^{-1} for specimens tested at 0.01 s^{-1}, 0.1 s^{-1}, 1.0 s^{-1}, and 10.0 s^{-1}, correspondingly (Table 4.3). Furthermore, the characteristic averages and variation corridors were plotted together for the marker data by loading rate (Fig. 4.6). The data showed that when the loading rate increased, the failure stress increased and the failure strain decreased (Table 4.3). The number of samples in each group is shown in Table 4.3.

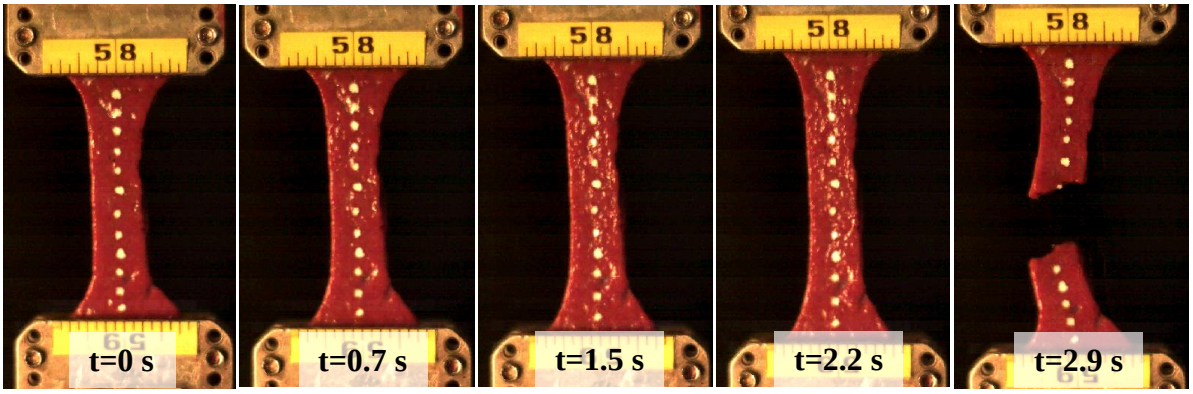

Figure 4.4. High-speed video stills of a typical uniaxial tensile test (Rate 2: 0.1 s^{-1}).

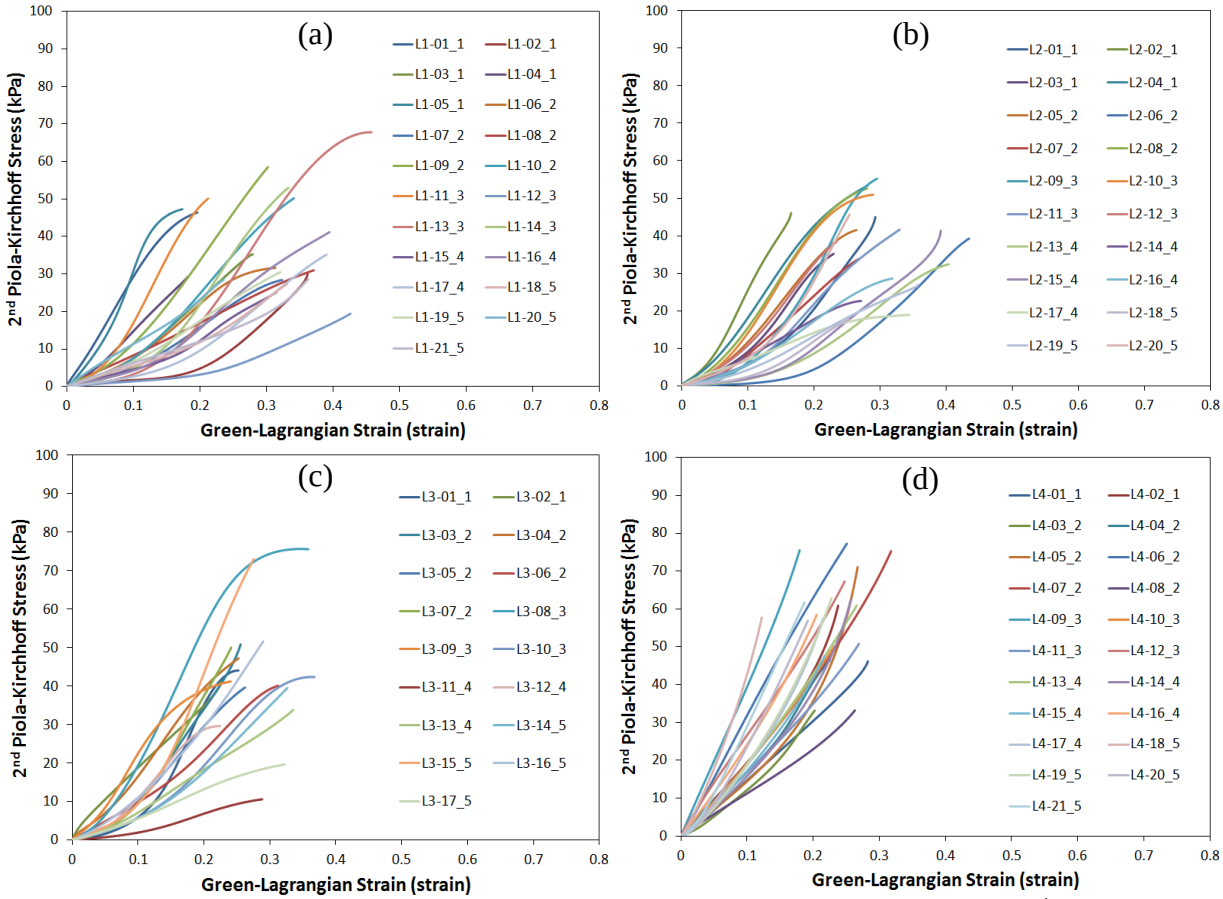

Figure 4.5. Stress vs. strain curves from marker data analysis (a) Rate 1: 0.01 s^{-1}; (b) Rate 2: 0.1 s^{-1}; (c) Rate 3: 1.0 s^{-1}; (d) Rate 4: 10.0 s^{-1}. The last digit of each specimen ID is the donor subject ID**.**

Table 4.3. Averages and standard deviations by loading rate.

Rate	# of samples	Desired Strain Rate (s^{-1})	Average Strain Rate (s^{-1})	Average Failure Strain (strain)	Average Failure Stress (kPa)
Rate 1	21	0.01	0.009 (±0.002)	0.32 (±0.08)	37.85 (±12.62)
Rate 2	20	0.1	0.083 (±0.015)	0.30 (±0.06)	38.36 (±11.24)
Rate 3	17	1.0	0.837 (±0.193)	0.28 (±0.05)	43.00 (±16.00)
Rate 4	21	10.0	9.541 (±2.249)	0.23 (±0.04)	57.78 (±12.32)

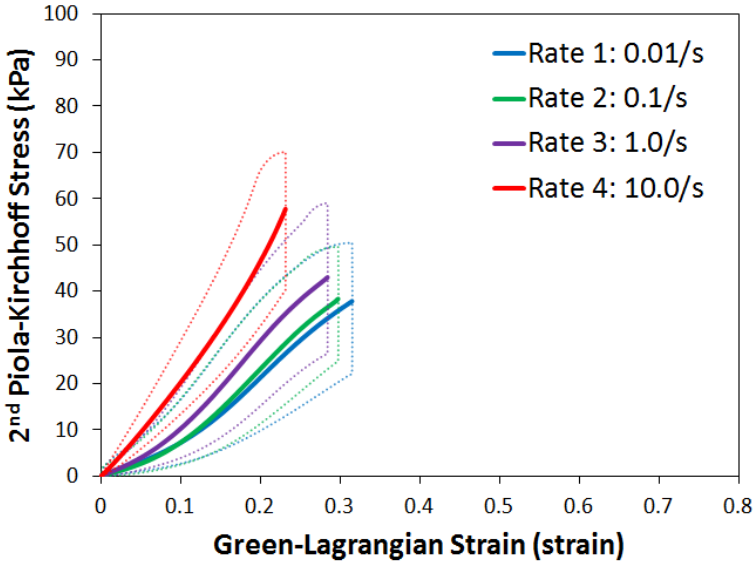

Figure 4.6. Characteristic averages and variation corridors by rates based on the marker data analysis.

The two-way ANOVA for testing the effects of strain rates and donors for marker data showed that the means of failure strain and failure stress were significantly different between strain rates ($p<0.01$ for both failure strain and failure stress), and were significantly different between donors ($p<0.01$ and $p=0.02$, correspondingly) (Table 4.4). No significant interaction effects were found between strain rates and donors ($p=0.22$ and $p=0.64$ for failure strain and failure stress, correspondingly). Multiple comparison tests showed that the mean failure strain of Rate 4 specimens was significantly lower than those from the other three rates ($p<0.05$) (Table 4.4). In addition, the mean failure stress of Rate 4 specimens was significantly higher than those from the other three rates ($p<0.05$). Furthermore, the mean failure strain of Donor #1 specimens was significantly lower than those from #4 ($p<0.05$), while the mean failure stress of Donor #3 specimens was significantly higher than the mean failure stress of Donor #4 ($p<0.05$).

Table 4.4. Two-way ANOVA for testing the effects of strain rates and donors on the mean of the failure strain and failure stress. Bold: p-value<0.05.

Failure Strain	F-value	p-value	Comparisons (**p<0.05**)
Strain Rate	10.94	**<0.01**	Rate 1,2,3 > Rate 4
Donor	4.13	**<0.01**	Donor 1 < Donor 4
Rate and Donor Interaction	1.34	0.22	
Failure Stress	F-value	p-value	Comparisons (**p<0.05**)
Strain Rate	11.82	**<0.01**	Rate 1,2,3 < Rate 4
Donor	3.04	**0.02**	Donor 3 > Donor 4
Rate and Donor Interaction	0.80	0.64	

The two-sample Mann–Whitney tests showed that no significant differences were found in terms of failure properties between data in the current study and the human data reported previously [2] for corresponding rate and stress/strain combinations (p>0.05) (Fig. 4.7). This validates the experimental testing protocols and procedures in the current study. In addition, the average values of failure GL strain and failure 2nd PK stress from the tensile tests on fresh bovine livers in Chapter 3, which were also reported by Lu et al. [5], were not significantly different from the corresponding marker data of human livers reported in the current study by using the Mann–Whitney tests (p>0.05). This similarity indicates that the fresh bovine liver can serve as a proper surrogate for investigating the failure properties of the fresh human liver. An increase in failure stress and a decrease in failure strain with the increase in strain rate were observed for all data sets.

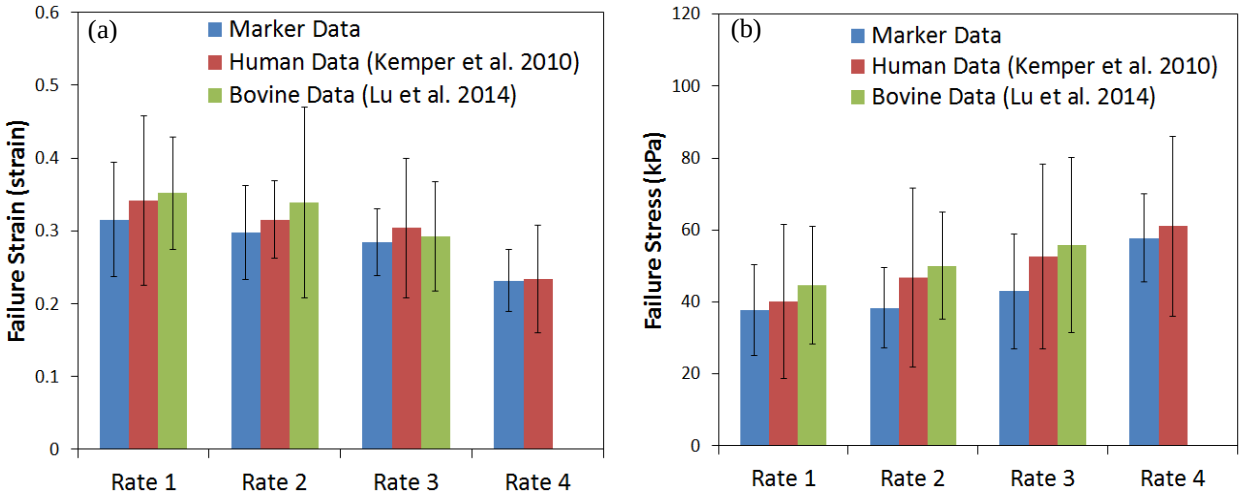

Figure 4.7. Comparisons of failure properties between current study, Kemper's study [2], and Lu's study [5]. (a) Failure Green-Lagrangian strain; (b) Failure 2nd Piola-Kirchhoff stress.

4.3.2. Specimen-specific FE Analysis

The average ground-state shear modulus μ ranged from 25.83 to 28.25 when the strain rate increased from 0.01 s^{-1} to 10.0 s^{-1}. The average of optimal material model parameter α_1 ranged from 8.47 to 12.52, and μ_1 ranged from 5.05 to 6.88 kPa (Table 4.5). Good correlations (R^2>0.99) were observed between the force time histories of the specimen-specific models with the material parameters obtained by the FE-based optimization approach and corresponding test data, indicating the good model fittings of the Ogden material model.

All specimens failed completely in the gauge length of the specimens. A failure criterion was not defined in the specimen-specific FE model, but the highest values of GL strain (along the loading direction) were always observed in the gauge length (Fig. 4.8).

Table 4.5. Ogden material model parameters.

Rate 1	α_1	μ_1	μ	Rate 2	α_1	μ_1	μ	Rate 3	α_1	μ_1	μ	Rate 4	α_1	μ_1	μ
L1-01_1	8.86	9.55	42.31	L2-01_1	9.73	7.90	38.43	L3-01_1	10.56	7.52	39.67	L4-01_1	8.12	10.49	42.57
L1-02_1	10.95	3.27	17.91	L2-02_1	8.24	12.35	50.89	L3-02_1	7.15	14.39	51.47	L4-02_1	10.12	12.71	64.33
L1-03_1	6.72	7.77	26.12	L2-03_1	10.86	6.97	37.87	L3-03_2	9.80	3.64	17.84	L4-03_2	10.82	5.02	27.15
L1-04_1	14.62	3.75	27.39	L2-04_1	9.90	9.74	48.19	L3-04_2	8.86	5.81	25.75	L4-04_2	11.40	6.44	36.71
L1-05_1	13.25	5.21	34.54	L2-05_2	7.56	6.68	25.25	L3-05_2	9.24	5.08	23.45	L4-05_2	10.19	4.79	24.41
L1-06_2	7.70	6.91	26.61	L2-06_2	9.82	5.06	24.86	L3-06_2	7.98	9.55	38.09	L4-06_2	11.53	5.77	33.26
L1-07_2	7.26	5.25	19.06	L2-07_2	9.54	3.71	17.69	L3-07_2	14.14	2.91	20.61	L4-07_2	9.95	7.56	37.62
L1-08_2	7.70	3.91	15.04	L2-08_2	8.33	7.44	30.98	L3-08_3	11.19	5.28	29.57	L4-08_2	8.83	4.66	20.57
L1-09_2	8.02	9.44	37.82	L2-09_3	9.96	4.77	23.75	L3-09_3	12.01	3.11	18.66	L4-09_3	9.38	6.87	32.24
L1-10_2	8.55	6.86	29.32	L2-10_3	9.83	4.63	22.75	L3-10_3	10.25	5.90	30.23	L4-10_3	11.29	4.50	25.39
L1-11_3	10.07	6.57	33.06	L2-11_3	9.75	4.44	21.68	L3-11_4	10.21	2.28	11.64	L4-11_3	10.41	4.41	22.97
L1-12_3	16.47	0.88	7.21	L2-12_3	13.90	2.21	15.38	L3-12_4	11.13	3.38	18.82	L4-12_3	10.82	7.83	42.37
L1-13_3	9.14	6.63	30.27	L2-13_4	9.30	5.31	24.70	L3-13_4	12.29	2.72	16.70	L4-13_4	12.07	3.24	19.53
L1-14_3	7.74	8.28	32.03	L2-14_4	7.01	7.25	25.41	L3-14_5	9.68	6.19	29.97	L4-14_4	12.86	3.11	20.01
L1-15_4	6.36	5.63	17.91	L2-15_4	10.09	4.17	21.05	L3-15_5	14.17	3.34	23.69	L4-15_4	10.34	3.80	19.66
L1-16_4	3.32	9.26	15.37	L2-16_4	8.23	5.40	22.22	L3-16_5	8.65	8.09	34.97	L4-16_4	12.78	3.24	20.70
L1-17_4	8.00	3.50	14.00	L2-17_4	4.32	13.10	28.32	L3-17_5	5.55	8.66	24.05	L4-17_4	12.82	3.13	20.04
L1-18_5	5.00	9.80	24.49	L2-18_5	11.14	2.08	11.59					L4-18_5	19.47	2.92	28.38
L1-19_5	7.62	6.17	23.51	L2-19_5	5.33	8.30	22.10					L4-19_5	18.92	2.09	19.75
L1-20_5	5.49	15.00	41.19	L2-20_5	12.88	2.93	18.87					L4-20_5	21.37	1.75	18.69
L1-21_5	5.00	10.95	27.37									L4-21_5	19.40	1.73	16.83
Mean	**8.47**	**6.88**	**25.83**	**Mean**	**9.29**	**6.22**	**26.60**	**Mean**	**10.17**	**5.76**	**26.78**	**Mean**	**12.52**	**5.05**	**28.25**
SD	**3.20**	**3.16**	**9.34**	**SD**	**2.23**	**3.02**	**10.16**	**SD**	**2.27**	**3.15**	**10.03**	**SD**	**3.84**	**2.83**	**11.52**

Note: Units: μ_1 (kPa) and μ (kPa). The last digit of each specimen ID is the donor subject ID.

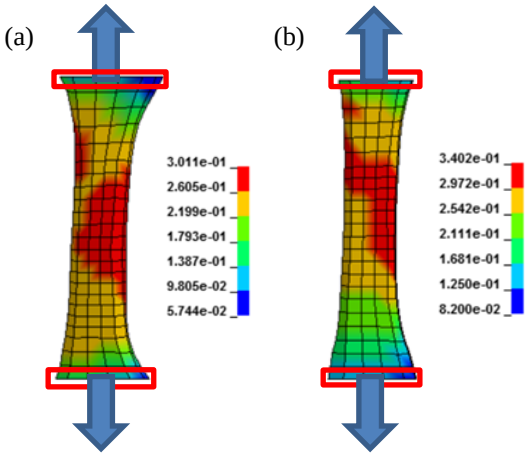

Figure 4.8. The distribution of Green-Lagrangian strain before failure for typical samples at high loading rate tensile tests. FE model with FE-based optimized material model parameters (a) Rate 4 (specimen L4_02_1); (b) Rate 3 (specimen L3_02_1). Red boxes represent the locations of boundary conditions.

The stress-strain curves by loading rate for all specimens obtained by the specimen-specific FE models with the optimized material parameters are shown in Fig. 4.9. The characteristic averages and the variation corridors of these stress-strain curves calculated for each loading rate are shown in Fig. 4.10. The slopes of the average curves became larger when increasing the strain rates, indicating the stiffer responses at higher strain rates.

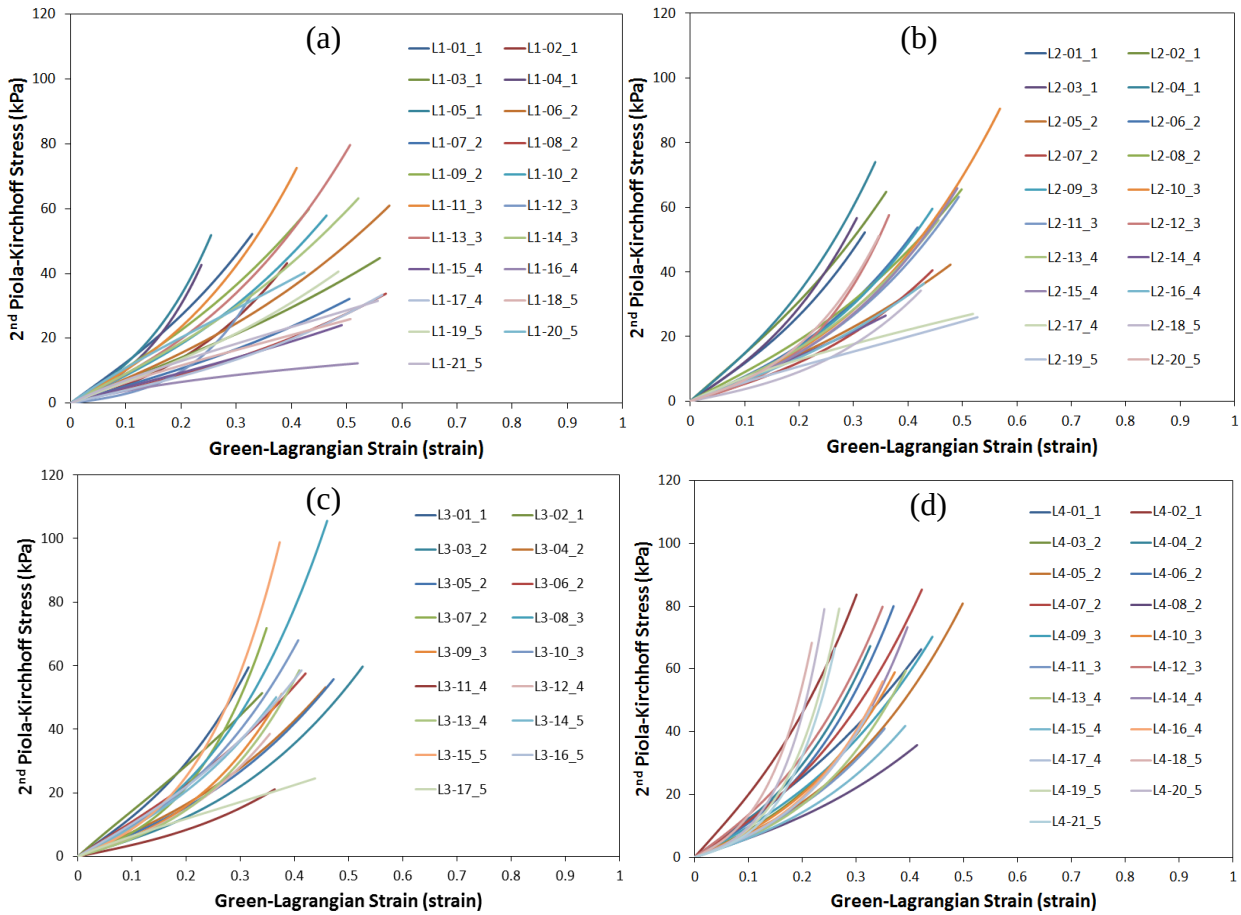

Figure 4.9. Stress vs. strain curves from FE-based optimization analysis (a) Rate 1: 0.01 s^{-1}; (b) Rate 2: 0.1 s^{-1}; (c) Rate 3: 1.0 s^{-1}; (d) Rate 4: 10 s^{-1}. The last digit of each specimen ID is the donor subject ID.

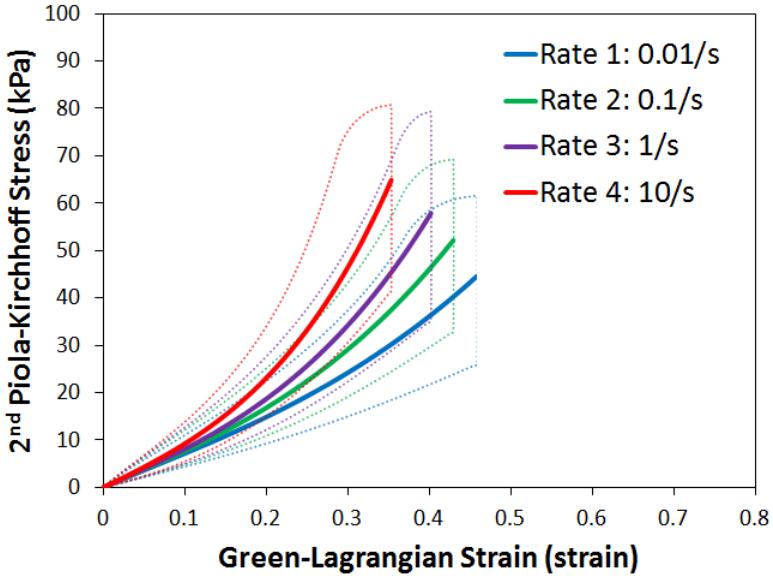

Figure 4.10. Characteristic averages and variation corridors by rates based on the Ogden material models from specimen-specific FE simulations.

The average strain rates determined from the grip displacements and the average failure strain and the average failure stress determined from the FE-based data are shown in the Table 4.6. The calculated average strain rates were 0.012 s^{-1}, 0.098 s^{-1}, 1.022 s^{-1}, and 9.567 s^{-1} for specimens tested at 0.01 s^{-1}, 0.1 s^{-1}, 1.0 s^{-1}, and 10.0 s^{-1}, correspondingly (Table 4.6). Again, the data showed that when the loading rate increased, the failure stress increased and the failure strain decreased.

The two-way ANOVA for testing the effects of strain rates and donors for FE-based data showed that the means of failure strain and failure stress were significantly different between strain rates ($p<0.05$ for both failure strain and failure stress), and were significantly different between donors ($p<0.05$ for both failure strain and failure stress) (Table 4.7). No significant interaction effects were found between strain rates and donors ($p=0.11$ and $p=0.46$ for failure strain and failure stress, correspondingly). Tukey-Kramer multiple comparison tests showed that the mean failure strain of Rate 1 specimens was significantly higher than those from Rate 3 and Rate 4, and the mean failure strain of Rate 2 specimens was significantly higher than those from Rate 4 ($p<0.05$) (Table 4.7). In addition, the mean failure stress of Rate 4 specimens was significantly higher than those from Rate 1 and Rate 2, while the mean failure stress of Rate 3 specimens was significantly higher than those from Rate 1 ($p<0.05$). Furthermore, the mean failure strain of Donor #1 specimens was significantly lower than those from the other three donors ($p<0.05$). On the other hand, the mean failure stress of Donor #4 specimens was significantly lower than the mean failure stress of the other three donors ($p<0.05$).

Table 4.6. Averages and standard deviations by loading rate.

Rate	# of samples	Desired Strain Rate (s^{-1})	Average Strain Rate (s^{-1})	Average Failure Strain (strain)	Average Failure Stress (kPa)
Rate 1	21	0.01	0.012 (±0.002)	0.46 (±0.10)	44.63 (±16.85)
Rate 2	20	0.1	0.098 (±0.012)	0.43 (±0.08)	52.17 (±17.01)
Rate 3	17	1.0	1.022 (±0.141)	0.40 (±0.06)	57.89 (±21.32)
Rate 4	21	10.0	9.567 (±0.282)	0.35 (±0.07)	64.88 (±15.77)

Table 4.7. Two-way ANOVA for testing the effects of strain rates and donors on the mean of the failure strain and failure stress. Bold: p-value<0.05.

Failure Strain	F-value	p-value	Comparisons (**p<0.05**)
Strain Rate	12.87	**<0.01**	Rate 1> Rate 3,4; Rate 2>Rate 4
Donor	8.02	**<0.01**	Donor 1 < Donor 2,3,4
Rate and Donor Interaction	1.61	0.11	
Failure Stress	F-value	p-value	Comparisons (**p<0.05**)
Strain Rate	7.05	**<0.01**	Rate 1< Rate 3,4; Rate 2<Rate 4
Donor	5.42	**<0.01**	Donor 1,2,3 > Donor 4
Rate and Donor Interaction	1.00	0.46	

Furthermore, the characteristic averages and variation corridors were plotted together for both marker data and FE-based data by loading rate (Fig. 4.11). Both average values of failure GL strain and failure 2nd PK stress of the FE-based data were significantly larger than the corresponding marker data by using the paired sample t-tests for all strain rates ($p<0.05$), as in a previous study using FE-based optimization analysis on fresh bovine livers [88]. It should also be mentioned that the average stress-strain curves obtained from marker data were usually stiffer than the curves from FE-based data.

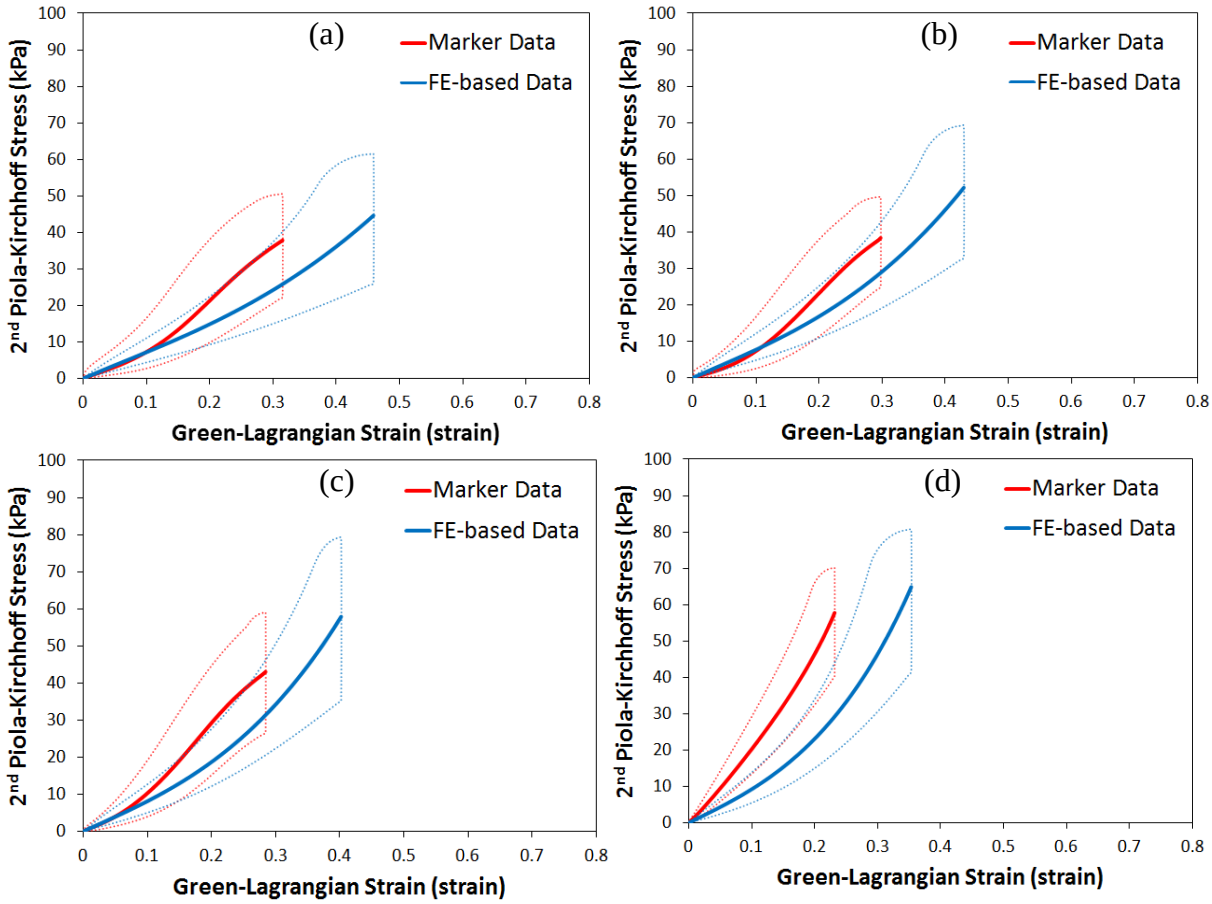

Figure 4.11. Comparisons of characteristic averages and variation corridors by rates between marker data and FE-based data (a) Rate 1: 0.01 s^{-1}; (b) Rate 2: 0.1 s^{-1}; (c) Rate 3: 1.0 s^{-1}; (d) Rate 4: 10.0 s^{-1}.

4.3.3 Stochastic Optimization

The SDs of the model parameters $(\mu_{1SD}^*, \alpha_{1SD}^*)$ obtained by the stochastic optimization process are presented together with the parameters of average curves (μ_1^*, α_1^*) in Table 4.8. α_1^* ranged from 8.3 to 12.0, and μ_1^* ranged from 4.5 to 5.8 kPa. The mean failure GL strain (ε_f^*) obtained by the specimen-specific FE analysis decreased from 0.46 to 0.35 as loading rate increased. The SD of the failure GL strain (ε_{fSD}^*) ranged from 0.05 to 0.09. The "test" and optimized "simulation" corridors, along with their characteristic averages, based on 1000 LHS samples, are plotted in Fig. 4.12.

Table 4.8. Stochastic optimization of Ogden material parameters and failure strain by strain rate.

Rate	Average			Standard Deviation		
	α_1^*	μ_1^* (kPa)	ε_f^*	α_{1SD}^*	μ_{1SD}^* (kPa)	ε_{fSD}^*
Rate 1	8.300	5.843	0.456	0.384	0.441	0.093
Rate 2	9.403	5.322	0.428	0.386	0.362	0.070
Rate 3	10.421	4.873	0.401	0.447	0.316	0.055
Rate 4	12.009	4.503	0.352	0.316	0.334	0.050

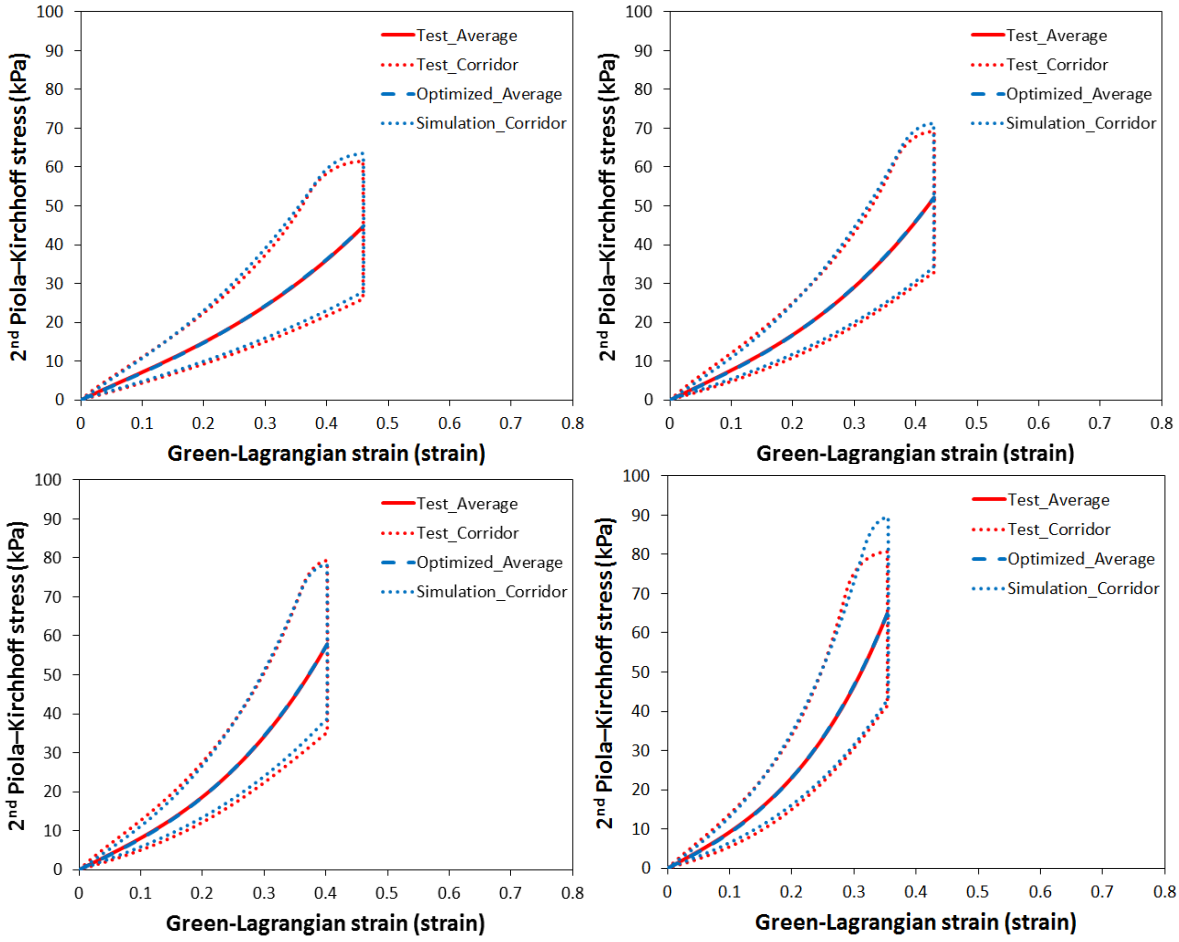

Figure 4.12. Stochastic optimization: comparisons between test and simulation corridors (a) Rate 1; (b) Rate 2; (c) Rate 3; (d) Rate 4.

4.4. Discussion

To investigate the variations of the material properties of liver parenchyma, uniaxial tensile tests were performed in *vitro* at four different loading rates (0.01 s^{-1}, 0.1 s^{-1}, 1.0 s^{-1} and 10.0 s^{-1}) on samples extracted from five fresh human livers. A typical non-linear behavior was

observed in the structural properties of human liver parenchyma with a convex toe region followed by an almost linear region. In addition to these regions, a concave shape close to the pre-failure region was observed especially for low rate tests (0.01 s^{-1}, 0.1 s^{-1}). All these curve features are similar to those tensile tests reported previously for porcine liver [163], bovine liver [88], and human liver [2]. A phenomenological hyperelastic model [133] with two parameters showed a good fit to experimental data before the peak force (failure point). While a better fit could hypothetically be obtained by increasing the complexity of the material model, a complex material model could also increase the number of unknown parameters and consequently the computational effort.

The marker data analysis determined the material and failure properties based on the material responses on the failure (tearing) site of the specimens [2, 88]. This method characterizes only the regional properties of the specimens by ignoring the displacement field of all the dots. A digital image correlation (DIC) and dense speckle patterns [161], could be used to better estimate the strain field in the whole specimen in future tests.

One of the main goals of employing the specimen-specific FE analysis and obtaining its material properties in this study was to obtain the material model parameters, which could be applied to liver parenchyma FE models in common commercial FE software packages such as LS-Dyna. A nearly incompressible material model of the liver parenchyma could be easily defined using MAT_181 in LS-Dyna v. 6.0, based on the average stress-strain curves reported in this study (See Chapter 5). This LS-Dyna material model uses a tabulated formulation of hyper-elasticity with rate effects and shows good capability in various numerical validations [174]. Compared to the classical hyper-viscoelastic formulations which include viscous terms that require complex and time consuming parameter identification methods [24, 175, 176], the tabulated stress-strain formulation is undoubtedly more computational efficient [174].

The region near the clamps could be a region of high overall stress (e.g. von Mises stress) during testing, due to the compressive stress added by clamps. The specimen-specific FE models in the current study did not simulate the upper and lower clamps; instead the two ends of the specimens were fixed and had prescribed motion conditions. Since the specimens failed in the middle of specimens due to tensile loading, it is expected that the clamp compressive stress perpendicular to loading direction may have a negligible effect on overall tensile response of specimen.

The stress-strain curves obtained based on marker data showed usually stiffer responses than the corresponding curves from FE-based data (Fig. 4.11). To further verify this discrepancy, a comparison between the local response (tear site and gage length) and global response was conducted using a Rate 2 (strain rate=0.1 s^{-1}) specimen (Fig. 4.13). The local responses were calculated based on the marker data analysis in Section 4.2.2.1, and the global response was calculated based on the specimen-specific FE analysis in Section 4.2.2.2. It was found that the stress-strain behaviors had a slight difference between the tear site and gage length, suggesting that the possible non-uniform strain field of the tissue and some inherent measurement errors of the markers. In contrast, the global response was largely different from the local responses (tear site and gage length), which showed that the FE model which included the fillet area between the gage length and grips could result in different stress-strain behaviors.

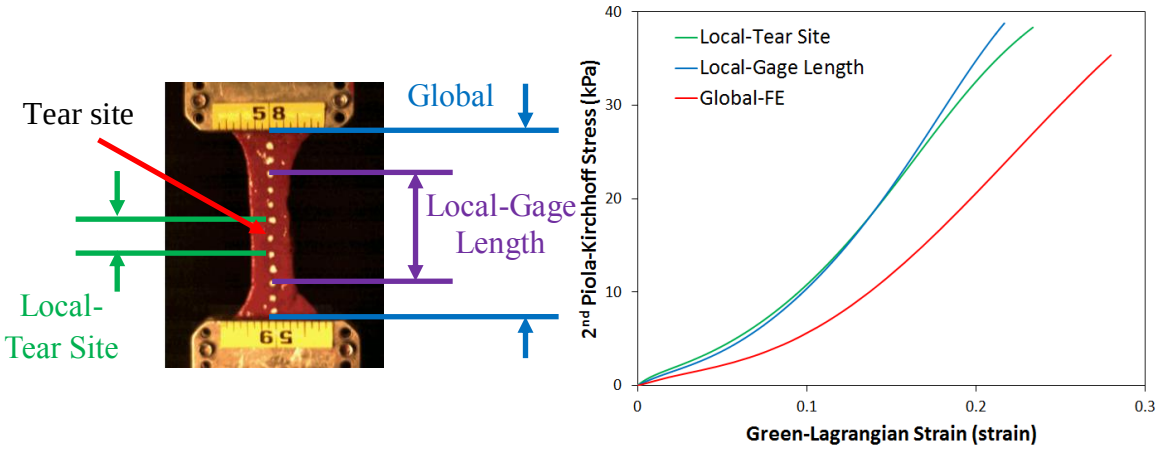

Figure 4.13. A comparison between local response (tear site and gage length) and global response of a typical example (Rate 2: 0.1 s^{-1}). (a) Definitions of local and global; (b) Stress-strain curves measured at the three locations.

As mentioned by previous studies [2, 161], one challenge of testing soft tissues is the determination of a consistent initial state of strain due to their extremely compliant nature. A procedure for estimating the zero-strain state in a specimen with the ends glued to the plates was proposed by Gao and Desai [161]. However, the specimens in their configuration fail at the glue interface, so the data could be used only for the non-failure domain. Using the test methodology presented by Kemper et al. [2], the specimens were allowed to hang under their own weight prior to the clamping of the bottom grip in this study. Based on the analysis of marker displacements during testing, a larger displacement was observed for the markers close to the lower clamp than similar markers close to the upper clamp. This observation may suggest a non-uniform initial strain field in the sample prior to the testing, with the upper region more loaded in tension than the lower region due to the tissue weight. A similar behavior was observed in test data reported by Gao and Desai [161] where the strain field was estimated using digital image correlation (DIC) and dense speckle patterns. In the current study, the displacements of markers were recorded using one camera. A possible motion of the markers perpendicular on the camera view plane due to an initial folding or specimen dynamics is inherently missed. Therefore, a better evaluation of the local strain could be obtained in future studies by using sophisticated optical systems, and spray painted pattern markers with DIC software.

The averages and SDs of the Ogden material model parameters determined by the stochastic optimization approach (Table 4.8) were different from those directly calculated from the material parameters of specimens (Table 4.5). This is because the stochastic optimization approach is used to obtain the averages and SDs from the "average stress-strain curves" and "corridors" (Table 4.8), rather than directly calculating the average and SDs of model parameters (Table 4.5). The averages and SDs in Table 4.5 could be sensitive to outliers, and the SDs could be overestimated. In addition, the model parameters are not independent, and the same stress-strain curve could be represented by various parameter sets. Therefore, it is suggested to determine the average curve and corridors first, and then implement the stochastic optimization.

The failure location in testing was generally in the middle region with high values of stress/strain observed in FE simulations, which may suggest that the stress/strain failure criteria could well predict the occurrence of tears. However, more validations against more complex impact tests, which will ideally include the whole liver, are suggested in the future. A modeling approach for the complex propagation of tears should be also investigated in the future. In addition to the traditional way of modeling failure (i.e. the element elimination) the application of new modeling approaches such as cohesive zone modeling [177, 178] and the extended FE method (XFEM) [179, 180] are recommended to be investigated as well.

In addition to the isotropy and incompressibility assumptions mentioned previously, this study also has several other limitations on the material modeling. The Ogden model, as all other hyperelastic models, allows an unrealistic continuous increase of strain energy with the increased strain. While the post-failure behavior was not investigated in this study, combining the continuum damage mechanics (CDM) with the existing hyperelastic models [181] in the future may help in better prediction of pre- and post-failure behavior of human soft tissues. The test data provided in this study were only obtained from five human livers. Performing additional tests on specimens obtained from more donors will provide a more accurate material characterization of human liver parenchyma.

A material model proposed in this study was based on data recorded in tensile tests. However, during crash events, the abdomen may also be subjected combined tension, compression and shear loading due to the contact with the belt system or other vehicle interior parts (e.g. steering wheel for both belted and unbelted occupants). This loading is transferred to the abdominal organs, and may result into complex stress distribution within the liver parenchyma. Therefore, the mechanical and failure properties of liver parenchyma under other loading conditions (e.g. compression and shear) can be combined with tensile properties reported in this chapter to develop deterministic and stochastic material models of parenchyma, which may be used in human FE models [26] to optimize the restraint systems in vehicles [182, 183]. For example, in Chapter 5, biomechanical properties of liver parenchyma from unconfined compression tests performed on human livers [2] were combined with the liver tensile properties to develop stochastic material models.

Under physiological conditions, the liver is perfused with blood, which may add some dilatation that is not present in the un-perfused liver parenchyma specimens. It was also reported that under quasi-static indentation loading, the un-perfused liver is stiffer and more viscous than the liver *in vivo* [184]. However, no *in vivo* data exist for dynamic loading conditions especially in failure, so the effects of perfusion on dynamic material properties of liver should be addressed in future studies.

It is well known that the amount of change in the material properties during sample preparation or excision cannot be quantified. Therefore, non-destructive experimental methods (e.g. indentation, aspiration ultrasonic tests) should be performed in the future for better *in vivo* characterization of liver and comparison with the classical tensile tests.

The hepatic capsule surrounding the liver is a tough fibrous and thin layer enriched with collagen and elastin. To develop a probabilistic FE model of human liver, the thickness and the material model of liver capsule should be also characterized statistically and then assigned to a

layer of shell elements surrounding the parenchyma solid elements. However, the fine layer of the liver capsule may not be easily reconstructed from medical image scans, so new methods should be developed for quantifying the variation in thickness of liver capsule. It is also known that the liver capsule has higher stiffness than liver parenchyma [2, 119]. Therefore, in Chapter 5, the statistical distributions of the liver capsule properties were also considered in order to develop probabilistic liver FE models (See Chapter 5).

Chapter 5

Probabilistic Finite Element Models of Human Liver

5.1. Introduction

Physical and biological systems, such as abdominal organs, contain inherent variability in geometry and material properties. In addition, some variability may exist in the loading conditions they are subjected to. The combined effects of the variations in inputs can dramatically affect output performance such as predicted stress/strain and probability of failure. However, traditional deterministic analysis does not consider this variability. In this study, an efficient probabilistic tool was developed to quantify the effect of uncertainty in the design variables on the biomechanical and injury responses of the human liver during impact events.

The main difference between the deterministic analysis and probabilistic analysis is the consideration of uncertainty in the input variables in the systems (Fig. 5.1). Probabilistic analysis considers the uncertainty of the input variables, so each variable is typically represented as a distribution, and a distribution of performance is predicted. In contrast, in deterministic study, a particular value is chosen for each input variable, and a single value is exported for each output variable.

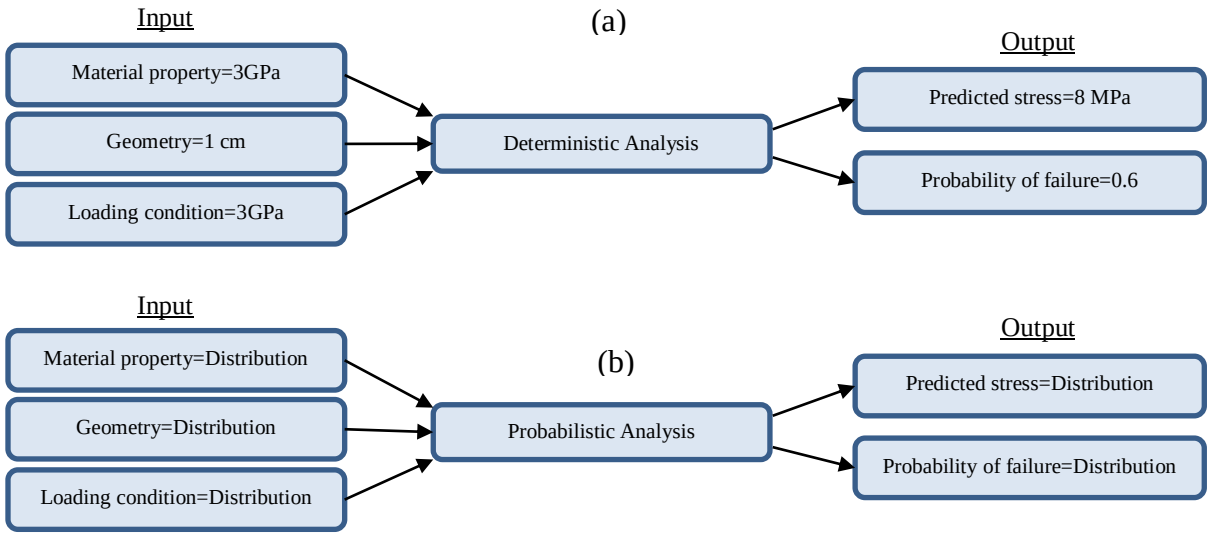

Figure 5.1. Illustrations of (a) deterministic analysis and (b) probabilistic analysis.

Probabilistic analysis is widely used in many areas, such as aeronautical [33, 34], automotive [35], orthopedic [32, 36-41] studies. However, due to high computational cost, two dimensional (2D) simplified FE models [36] or idealized geometry [38] are commonly used in these studies. Dar et al. [32] conducted probabilistic analysis to predict the maximum stress distribution on a cantilever beam FE model, representing an orthopaedic cervical fixation plate.

The authors mentioned that this probabilistic method was not very efficient, requiring about 1,000 numerical simulations to get a reasonably smooth distribution; therefore, they used a simplified FE model. Nicolella et al. [38] developed a 3D femur-implant model, in which variability of material properties and loading conditions were considered to predict the probability of failure. A simplified FE model for this femur-implant structure was used to avoid large computational time, but the geometry variations were not considered in this probabilistic study. In general, no probabilistic models were proposed for human internal organs or soft tissues, such as the human liver in current literature.

In order to conduct the probabilistic analysis on human body, a verified computational whole body human FE model should be utilized. Since 1997, Toyota Motor Corporation has been developing and improving the Total Human Model for Safety (THUMS), to analyze and simulate situations that are closer to the realistic automotive accidents. The model was designed to simulate the human body kinematics and injuries in response to automotive crash or impact events [185-187]. Thus, it was chosen for the probabilistic analysis in this study.

The liver model in THUMS model is surrounded by a group of solid organs, vessels, and membranes. The lateral and superior portion of the liver is covered by the diaphragm and pleura (serous membrane) (Fig. 5.2a). The structures outside of the pleura are the ribs #6-#10 and costal cartilage (Fig. 5.2a). The inferior and posterior portion of the liver is covered by the peritoneum (serous membrane) and abdominal fat (Fig. 5.2b). Between the posterior part of the liver and the peritoneum, there are a few solid organs and vessels (Fig. 5.2c, 5.2d). The solid organs include stomach, duodenum, gallbladder, kidney, and large intestine (Fig. 5.2c). The gallbladder is imbedded between the two lobes of the liver, creating a concave surface of the liver. There are three major vessels passing through the liver (Fig. 5.2d): thoracic aorta, inferior vena cava, and hepatic portal vein. These vessels are also located between the two lobes of the liver. These solid organs, vessels, and abdominal fat are supported by the spine and the ribs.

Most of the abdominal organs in THUMS were modelled as nonlinear elastic materials based on the material properties reported in the literature [162, 185]. Tetrahedron elements were used to model the liver parenchyma and a rubber like material (MAT_181) was assigned based on test data reported by Tamura et al. [7, 185] (Table 5.1). A single load curve, defining the force versus actual change in the gauge length, was defined in the original material model of THUMS liver parenchyma, so no strain rate dependency was considered (Fig. 5.3). The original liver capsule was modeled using triangular shell elements which were assigned a fabric material (MAT_034) (Table 5.1). Both material models of liver parenchyma and capsule were derived merely based on porcine liver data [7, 162]. However, it has been shown in the literature that the structures and injury tolerance of porcine and human livers are different [2], which suggest updating THUMS liver model based on human material data [1, 86, 159].

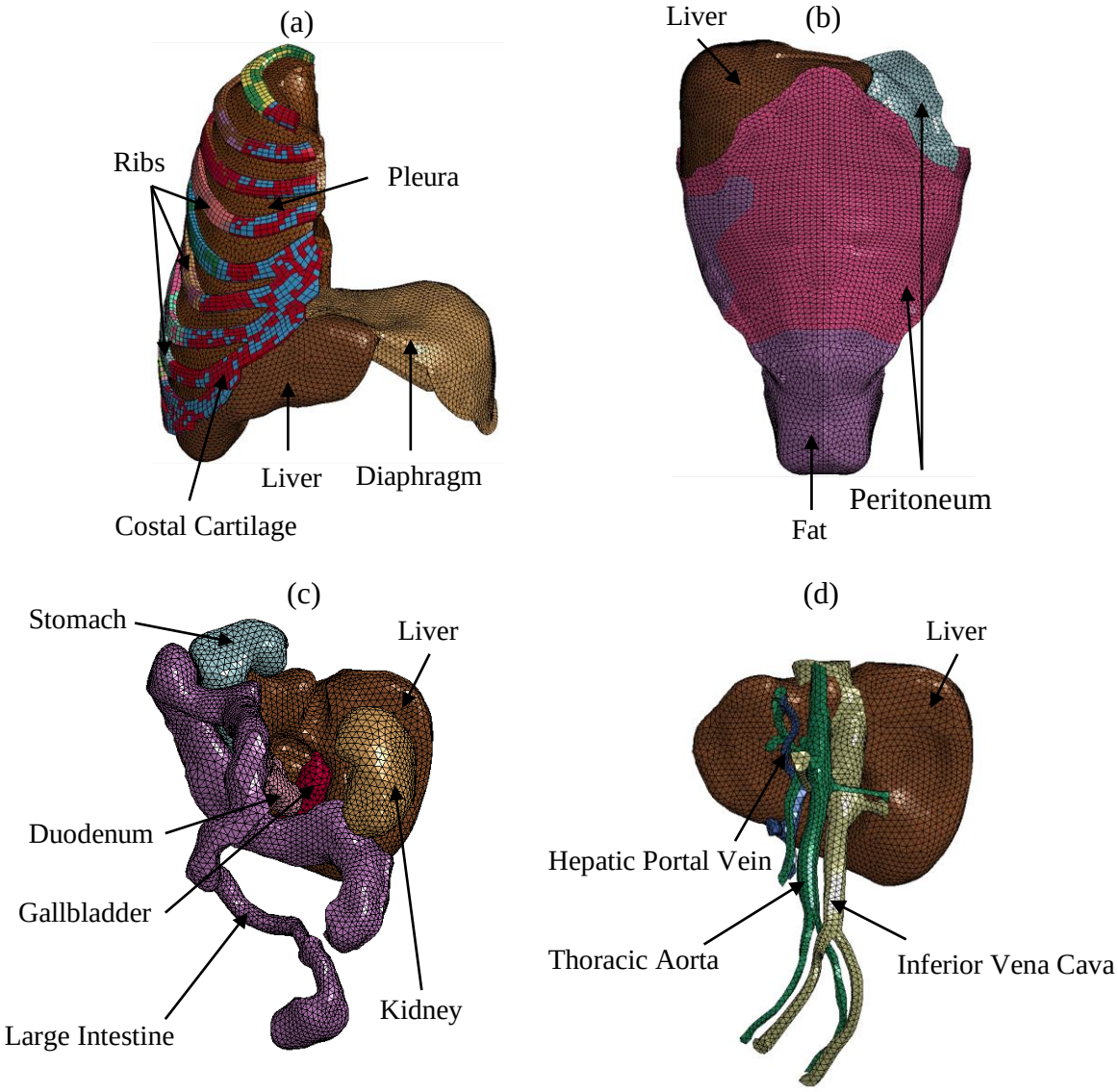

Figure 5.2. The structures surrounding the liver model in THUMS. (a) and (b): anterior view; (c) and (d): posterior view.

Table 5.1. Material models and element information for the default liver capsule and parenchyma in the THUMS AM50 Version4.

	Liver Capsule	Liver Parenchyma
Mesh	Triangular shell	Tetrahedron
# of Elements	6521	58557
LS-DYNA Material	Mat_Fabric (MAT_034)	Mat_Simplified_Rubber/Foam (MAT_181)

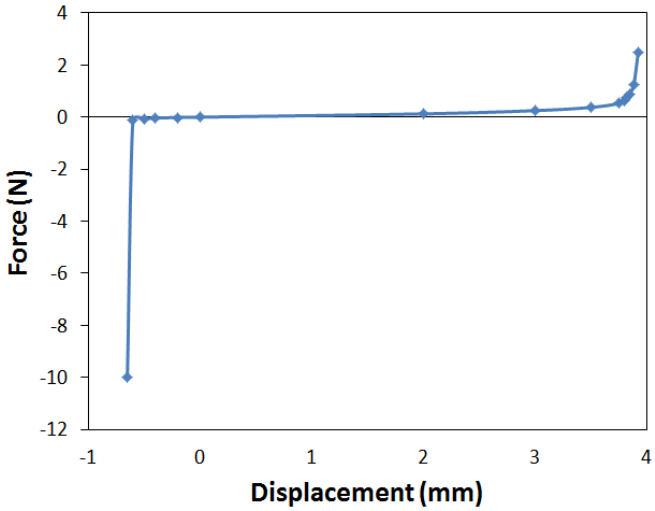

Figure 5.3. The force-displacement curve defined in the material model (MAT_181) of liver parenchyma in the THUMS AM50 Version4.

To investigate the differences of the biomechanical responses caused by the variations of the liver material properties and loading conditions, the impact scenarios reported by Viano et al. [3, 4] were simulated using the THUMS 50th percentile male (AM50) Version 4 model. In Viano's study, a 23.4 kg pendulum was freely suspended by guide wires and accelerated to impact speeds of approximately 4.5, 6.7, or 9.4 m/s (Fig. 5.4). The time-history of impact force was calculated based on the time history of pendulum acceleration and the pendulum mass. Each of the 14 PMHS tests was assigned to one of the three impact speeds. The rib fractures and organ injuries sustained by each subject were reported [3]. The Maximum Abbreviated Injury Scale (MAIS) of each subject was determined based on type of injury recorded (e.g. number of rib fractures, abdominal injuries, etc.). In addition, injury risks were predicted based on five injury criteria: viscous response, compression response, spinal acceleration response at T8 and T12, and impactor force. The logistic regression was applied to find the 50% probability of injury for both MAIS 3+ and MAIS 4+ critical injuries. They also found that the numbers of rib fractures were 0-4, 0-5, and 0-7 for tests with impact speeds of 4.5, 6.7, and 9.4 m/s, correspondingly. Lacerated livers were found only in the tests with impact speed of 9.4 m/s.

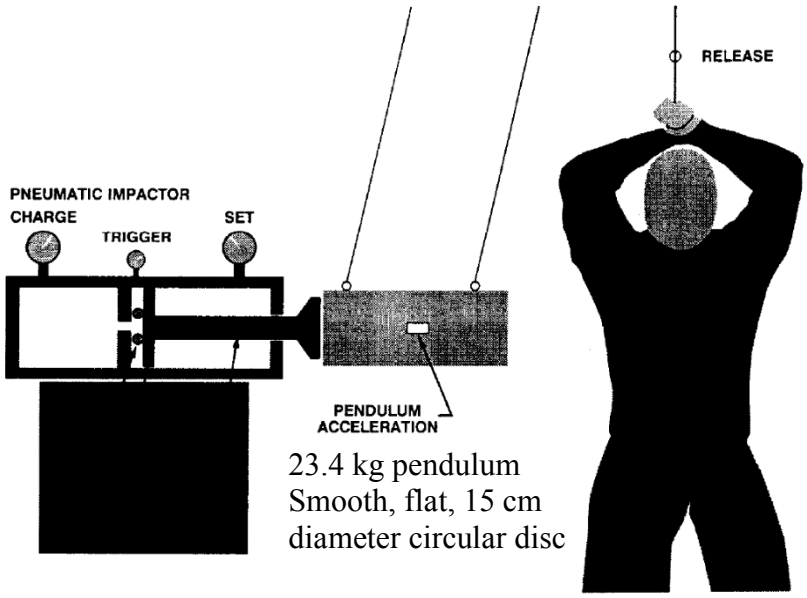

Figure 5.4. Lateral abdominal impact testing setup [3, 4].

The material variation of the human liver parenchyma tensile properties (Chapter 4) was combined with the variations of the human liver parenchyma compressive properties [159]. In addition, the variations of capsule tensile properties were considered as well [1]. The average material model was created together with 30 probabilistic liver material models, considering both liver capsule and parenchyma properties. Simulation results in terms of force-deflection and force-time curves were compared to the test corridors published by Viano [3]. Injuries of both liver and ribs were also investigated. The established probabilistic models in terms of liver material property variations could be combined with shape and location variations of the liver model to provide a better understanding of the injury variation observed in PMHS testing or field data.

5.2. Methodology

5.2.1. Liver Parenchyma Compressive Property

The material model for the liver parenchyma compressive property was derived based on the liver parenchyma compression testing study conducted by Kemper et al. [159]. In their study, a total of 36 uniaxial unconfined compression tests were performed on fresh human liver parenchyma from 6 subjects (1 male, 5 female) within 48 hours of death. Each specimen was tested once to failure at one of four imposed loading rates (0.01, 0.1, 1.0, 10.0 s^{-1}) in order to investigate the effects of loading rate on the compressive failure properties of human liver parenchyma. It was found that the failure true stress significantly increased with increased loading rate, while failure true strain significantly decreased with increased loading rate.

The reported true stress-true strain curves [159] were first converted to 2nd Piola-Kirchhoff (PK) stress-Green-Lagrangian (GL) strain curves. Then, each curve was fitted with a

5th degree polynomial with 5 parameters, which showed the best fit to the test data, where the constant term was set as zero (Eq. 5.1).

$$S_{1Comp} = P_{1Comp}\varepsilon_{1Comp}^5 + P_{2Comp}\varepsilon_{1Comp}^4 + P_{3Comp}\varepsilon_{1Comp}^3 + P_{4Comp}\varepsilon_{1Comp}^2 + P_{5Comp}\varepsilon_{1Comp} \quad \text{Eq. 5.1}$$

where S_{1Comp} is the 2nd PK stress, ε_{1Comp} is the GL strain, and P_{iComp}, $i = \overline{1,5}$ are the model parameters.

The optimized (average) model parameters for the parenchyma compression data, denoted as P_{iComp}^*, $i = \overline{1,5}$, were identified using the same analytical-based approach implemented in Chapter 4. The stochastic optimization proposed in Chapter 4 was applied to the parenchyma compression data to determine the standard deviation (SD) of the model parameters, $P_{iSDComp}^*$, $i = \overline{1,5}$. The differences between the "test" corridor and "simulation" corridor were minimized by the active-set optimization algorithm in MATLAB v. R2012b (The MathWorks, Inc., Natick, MA). Thus, the optimized SD values of the 5th degree polynomial parameters ($P_{iSDComp}^*$, $i = \overline{1,5}$) and the failure GL strain value ($\varepsilon_{fSDComp}^*$) were reported as statistical parameters of the material model of human liver parenchyma under compressive loading.

5.2.2. Liver Capsule Tensile Property

The material model for the liver capsule tensile property was derived based on the liver capsule tensile testing study conducted by Brunon et al. [1]. In their study, tensile quasi-static tests were run on fresh human liver capsule samples from 3 subjects (1 male, 2 female) until failure to characterize capsule failure. Digital image correlation (DIC) technique was used to measure the surface strain field on the capsule. Mean values of failure parameters for hepatic capsule were reported as 47±29% for the ultimate local strain and 0.3±0.3 N/mm for the ultimate load per width unit. It should be noted that all samples were loaded with a speed of 0.5 mm/s, which implied a range of longitudinal strain rate of 10^{-3}-10^{-2} s^{-1} depending on the sample initial length, remaining in quasi-static domain [1].

The material model used to describe the capsule tensile behavior was the Ogden material model. The reported load per width unit-GL strain curves were first converted to 2nd PK stress-GL strain curves. Eleven fresh human specimens were considered in this parameter identification process. Then, the curves were fitted with the Ogden material model with 2 parameters (Eq. 5.2).

$$S_{1Caps} = \frac{\mu_{1Caps}}{\lambda_{1Caps}}\left(\lambda_{1Caps}^{\alpha_{1Caps}-1} - \lambda_{1Caps}^{-\alpha_{1Caps}/2-1}\right) \quad \text{Eq. 5.2}$$

where S_{1Caps} is the 2nd PK stress, λ_{1Caps} is the stretch ratio, and α_{1Caps} and μ_{1Caps} are the two model parameters.

The optimized (average) model parameters for the capsule tensile data, denoted as α_{1Caps}^* and μ_{1Cap}^*, were identified using the same analytical-based approach implemented in Chapter 4. The stochastic optimization proposed in Chapter 4 could be applied to the capsule tensile testing data to determine the SD of the model parameters, $\alpha_{1SDCaps}^*$ and $\mu_{1SDCaps}^*$. The differences

between the "test" corridor and "simulation" corridor were minimized by the active-set optimization algorithm in MATLAB v. R2012b (The MathWorks, Inc., Natick, MA). Thus, the optimized SD values of the two Ogden model parameters (α^*_{1Caps} and μ^*_{1Caps}) and the failure GL strain value ($\varepsilon^*_{fSDCaps}$) were reported as statistical parameters of the material model of human liver capsule under tensile loading.

5.2.3. Average and Probabilistic Liver Material Models

The model parameters for liver capsule and parenchyma (Table 4.8, 5.3, and 5.4) were utilized to calculate average and probabilistic liver material models. The material and failure properties of liver parenchyma in tension were determined from uniaxial tensile tests presented in Chapter 4, and the material models of parenchyma in compression and capsule in tension were developed based on literature data (Section 5.2.1 and 5.2.2). The average material models were created based on the parameters of the average curves and failure strain values (Table 4.8, 5.3, and 5.4). The probabilistic liver material models were constructed based on the distributions of model parameters and failure strain values corresponding to various strain rates (Table 4.8, 5.3, and 5.4). To incorporate the strain rate dependency of the liver material property [86, 159], a scaling approach was developed to ensure that the stiffness of the liver parenchyma increases when strain rate increases. The details of this scaling approach are explained as follows.

For the liver parenchyma tensile properties, one set of the scaling factors for the two Ogden material parameters ($\mu_{1SFTens}$, $\alpha_{1SFTens}$) and for the failure GL strain $\varepsilon_{fSFTens}$ was randomly sampled from the standard normal distribution. This process is also called the "Monte Carlo method." The Monte Carlo method is a sampling method, which involves randomly generating values for each variable according to its distribution and then predicting the distribution of performance through repeated trials. Monte Carlo method will always converge to the correct solution with a large number of trials [188, 189].

These scaling factors were then applied to the four strain rates to obtain the probabilistic Ogden material parameters, i.e.

$$\mu^j_{1Tens} = \mu^{*j}_{1Tens} + \mu_{1SFTens} \times \mu^{*j}_{1SDTens}, j = \overline{1,4} \quad \text{Eq. 5.3}$$

$$\alpha^j_{1Tens} = \alpha^{*j}_{1Tens} + \alpha_{1SFTens} \times \alpha^{*j}_{1SDTens}, j = \overline{1,4} \quad \text{Eq. 5.4}$$

$$\varepsilon^j_{fTens} = \varepsilon^{*j}_{fTens} + \varepsilon_{fSFTens} \times \varepsilon^{*j}_{fSDTens}, j = \overline{1,4} \quad \text{Eq. 5.5}$$

By repeating this scaling approach, different sets of Ogden material model parameters and failure GL strain for the four strain rates could be generated.

This scaling approach can be similarly applied to the liver parenchyma compressive properties to generate probabilistic models (Eq. 5.6 and 5.7).

$$P^j_{iComp} = P^{*j}_{iComp} + P_{iSFComp} \times P^{*j}_{iSDComp} \quad \text{Eq. 5.6}$$

$$\varepsilon^j_{fComp} = \varepsilon^{*j}_{fComp} + \varepsilon_{fSFComp} \times \varepsilon^{*j}_{fSDComp} \quad \text{Eq. 5.7}$$

where $i = \overline{1,5}$ and $j = \overline{1,4}$.

For the liver capsule tensile properties, the probabilistic models can be expressed as:

$$\mu_{1Caps} = \mu^*_{1Caps} + \mu_{1SFCaps} \times \mu^*_{1SDCaps} \quad \text{Eq. 5.8}$$

$$\alpha_{1Caps} = \alpha^*_{1Caps} + \alpha_{1SFCaps} \times \alpha^*_{1SDCaps} \quad \text{Eq. 5.9}$$

$$\varepsilon_{fCaps} = \varepsilon^*_{fCaps} + \varepsilon_{fSFCaps} \times \varepsilon^*_{fSDCaps} \quad \text{Eq. 5.10}$$

A total of 30 sets of parameters were generated for liver parenchyma tensile and compressive properties, and liver capsule tensile property.

To implement these material models in LS-Dyna (MAT_181), the stress-strain curves were first calculated using Eq. 4.7, 5.1, and 5.2, and then they were transformed to force-displacement histories corresponding to a unit cubic (i.e. $1 \times 1 \times 1$ mm^3) using Eq. 4.4 for both liver capsule and parenchyma using the model parameters of the average and probabilistic material models. Then, the force-displacement curves of the liver parenchyma tensile and compressive behaviors were combined together for each strain rate (0.01, 0.1, 1.0, and 10.0 s^{-1}). In liver capsule material models, due to limited test data available, only tensile force-displacement curves were used (no strain rate dependent model).

5.2.4. Full-Body Behavior

Detailed descriptions of the postures of the PMHS at the time of the impact tests were not included in the literature [3, 4]; therefore, the postures of the THUMS models were simulated based on the figures in the literature (Fig. 5.4). Since THUMS pedestrian model was not available, the arms and legs of THUMS occupant model were arranged (using FE simulations) so that both arms were raised upwards and the legs were straight similar to a standing posture (Fig. 5.5).

The impactor was simulated as a 23.4 kg rigid cylinder, with a diameter of 15 cm. The impactor was adjusted to the 7.5 cm below the xiphoid and the axis of the impact force was aligned through the center of gravity of the torso [4]. The THUMS model was rotated 30° so the point of pendulum contact was lateral on the abdomen [3, 4]. Three averaged impact speeds obtained from the experimental testing were imposed to the impactor model: 4.79, 6.83, and 9.40 m/s. The simulations were terminated after 50 ms, which was determined to be the end of the major portion of the oblique impact event [190].

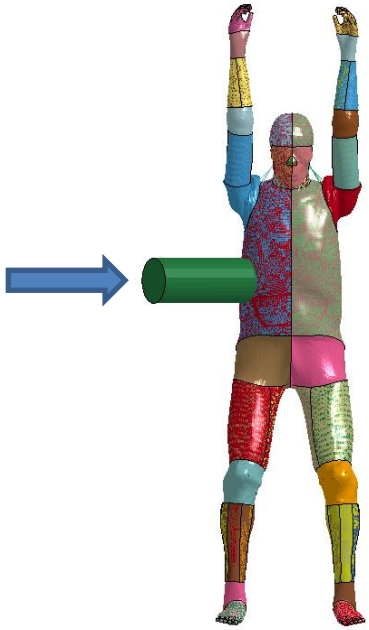

A total of 96 oblique impact simulations were employed using the THUMS FE model with various liver material properties (Table 5.2). First, the default THUMS model, which considers no strain rate dependency for the liver parenchyma, was run at 3 impact speeds (4.79, 6.83, 9.40 m/s). Next, the default THUMS model was updated using the average liver material models for capsule and parenchyma and impacted at 3 impact speeds (4.79, 6.83, 9.40 m/s). Finally, the THUMS models with the generated 30 probabilistic liver material models was impacted at the same 3 impact speeds (4.79, 6.83, 9.40 m/s). All 96 simulations were run on a cluster computer (Virginia Tech University Cluster) with 48 CPUs using LS-Dyna v. 6.1.1.

Table 5.2. List of simulation cases.

No.	# of Simulations	Liver Material Model	Impact Speeds
1-3	3	Default Materials	4.79, 6.83, 9.40 m/s
4-6	3	Updated Average Materials	4.79, 6.83, 9.40 m/s
7-36	30	30 Probabilistic Materials	4.79 m/s
37-66	30	30 Probabilistic Materials	6.83 m/s
67-96	30	30 Probabilistic Materials	9.40 m/s

The impact force and abdomen deflection were recorded in the FE simulations. The impact force was calculated at the impactor-THUMS contact surface. The time history of abdomen deflection was found as the displacement of the impactor during the contact between impactor and abdomen. The maximum force of each force-time curve was defined as "peak force" and its corresponding time was defined as the "time of peak force." The area under each force-deflection curve was defined as the amount of absorbed energy by body deformation [3, 190]. The force-deflection and force-time responses of THUMS were compared with corresponding data reported in literature [3].

In addition, the 1st principal GL strain-time histories and 3rd principal GL strain-time histories were determined directly from the simulation results using LS-PrePost Version 4.1 software. The maximum values of the 1st principal GL strain-time curves were defined as the "maximum tensile strain" for both liver capsule and liver parenchyma. Similarly, the minimum values of the 3rd principal GL strain-time responses were defined as the "maximum compressive strain," which were usually negative values representing compressive responses for liver parenchyma. These two indices were used to compare the simulations between default liver material model and updated average liver material model and between the probabilistic liver material properties at three impact speeds.

The predicted rib fractures were determined from the element failure reports from the simulations. The number of fractured ribs was compared with the test data reported by Viano et al. [3]. The contour maps of the 1st and 3rd principal GL strain were plotted to inspect the strain concentration locations on the liver capsule and parenchyma.

5.3. Results

5.3.1. Liver Parenchyma Compressive Property

The SD of the model parameters ($P^*_{iSDComp}$, $i = \overline{1,5}$) obtained by the stochastic optimization process based on test data [159] are listed together with the parameters of average curves (P^*_{iComp}, $i = \overline{1,5}$) in Table 5.3. The mean failure GL strain (ε^*_{fComp}) obtained by the experimental testing increases from -0.423 to -0.349 as loading rate increases. The SD of the failure GL strain ($\varepsilon^*_{fSDComp}$) ranged from 0.0089 to 0.0187. The "test" and optimized "simulation" corridors, along with their characteristic averages, based on 1000 Latin Hypercube Sampling (LHS) samples, are plotted in Fig. 5.6.

Table 5.3. Stochastic optimization of polynomial parameters by loading rate for liver compression testing. Unit for all "**P**" parameters: MPa.

Rate	$P^*_{1Comp}\pm P^*_{1SDComp}$	$P^*_{2Comp}\pm P^*_{2SDComp}$	$P^*_{3Comp}\pm P^*_{3SDComp}$	$P^*_{4Comp}\pm P^*_{4SDComp}$	$P^*_{5Comp}\pm P^*_{5SDComp}$	$\varepsilon^*_{fComp}\pm\varepsilon^*_{fSDComp}$
Rate 1	312.79±1.7734	217.86±1.7734	53.44±0.0001	5.24±0.0002	0.17±0.0001	-0.423±0.0187
Rate 2	140.41±3.2156	62.29±2.4975	11.04±0.0003	0.81±0.0004	0.02±0.0001	-0.384±0.0184
Rate 3	219.74±5.1905	82.15±5.6351	12.00±0.0040	0.72±0.0026	0.02±0.0001	-0.351±0.0161
Rate 4	182.68±0.0100	54.22±8.0134	6.16±0.0000	0.23±0.0087	0.01±0.0000	-0.349±0.0089

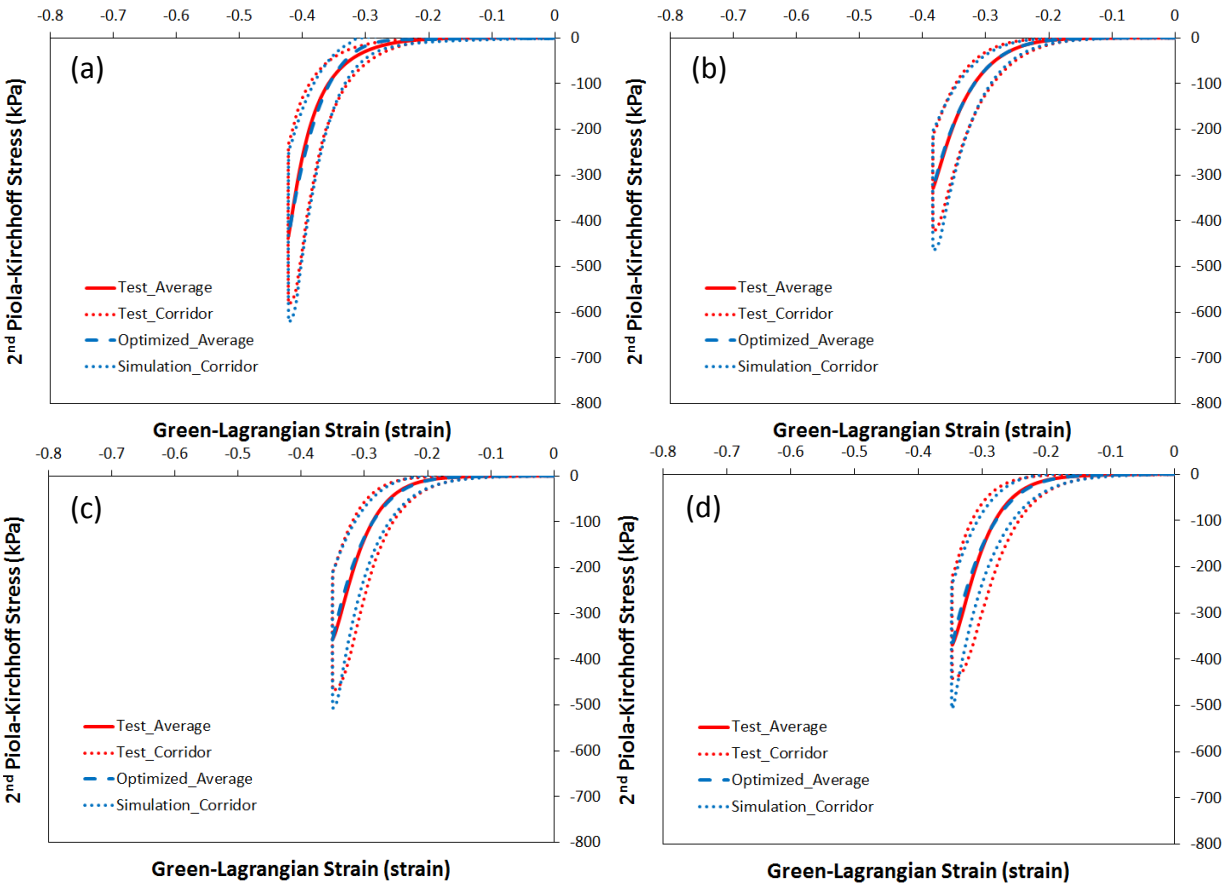

Figure 5.6. Stochastic optimization: comparison between test and simulation corridors for liver parenchyma compression testing (a) Rate 1; (b) Rate 2; (c) Rate 3; (d) Rate 4.

5.3.2. Liver Capsule Tensile Property

The SD of the Ogden model parameters, $\alpha^*_{1SDCaps}$ and $\mu^*_{1SDCaps}$, obtained by the stochastic optimization process based on test data [1] are 2.743 and 8.675 MPa, respectively (Table 5.4). The parameters of the average curve, α^*_{1Caps} and μ^*_{1Caps}, are 6.221 and 1.536, respectively. The average failure GL strain (ε^*_{fCaps}) obtained by the experimental testing is 0.145, and its SD ($\varepsilon^*_{fSDCaps}$) is 0.038. The "test" and optimized "simulation" corridors, along with the characteristic average, based on 1000 LHS samples, are plotted in Fig. 5.7.

Table 5.4. Stochastic optimization of Ogden material parameters and failure strain for liver capsule tensile testing.

$\alpha^*_{1Caps}\pm\alpha^*_{1SDCaps}$	$\mu^*_{1Caps}\pm\mu^*_{1SDCaps}$ (MPa)	$\varepsilon^*_{fCaps}\pm\varepsilon^*_{fSDCaps}$
6.221±2.743	1.536±8.675	0.145±0.038

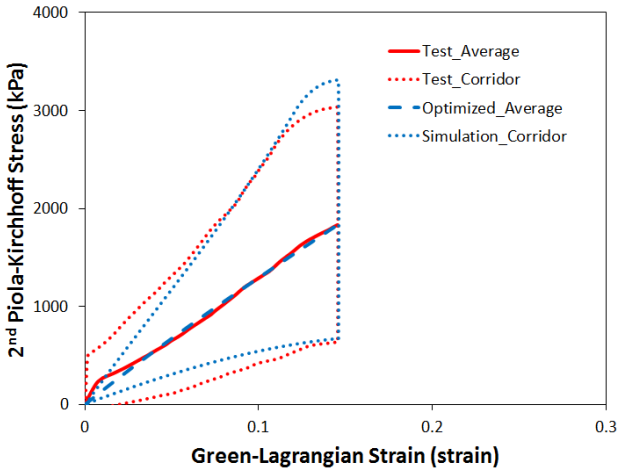

Figure 5.7. Stochastic optimization: comparison between test and simulation corridors for liver capsule tensile testing.

5.3.3. Average and Probabilistic Liver Material Models

The force-displacement responses implemented in LS-Dyna material model, MAT_181, of the average material models created based on the optimized parameters of the average curves (Table 4.8, 5.3, and 5.4) are shown in Fig. 5.8. In addition, thirty sets of scaling factors were generated based on the standard normal distribution (Table 5.5, 5.6, and 5.7), and the corresponding thirty probabilistic material models were created. Note that each set of the scaling factors for the liver parenchyma was applied to four strain rates (Eq. 5.3-5.7). Each material model of the parenchyma and the capsule contains data for four strain rates and one rate, respectively. The corresponding force-displacement responses determined from these thirty probabilistic material models are plotted in Fig. 5.9 and 5.10, together with the force-displacement curves of the average material models.

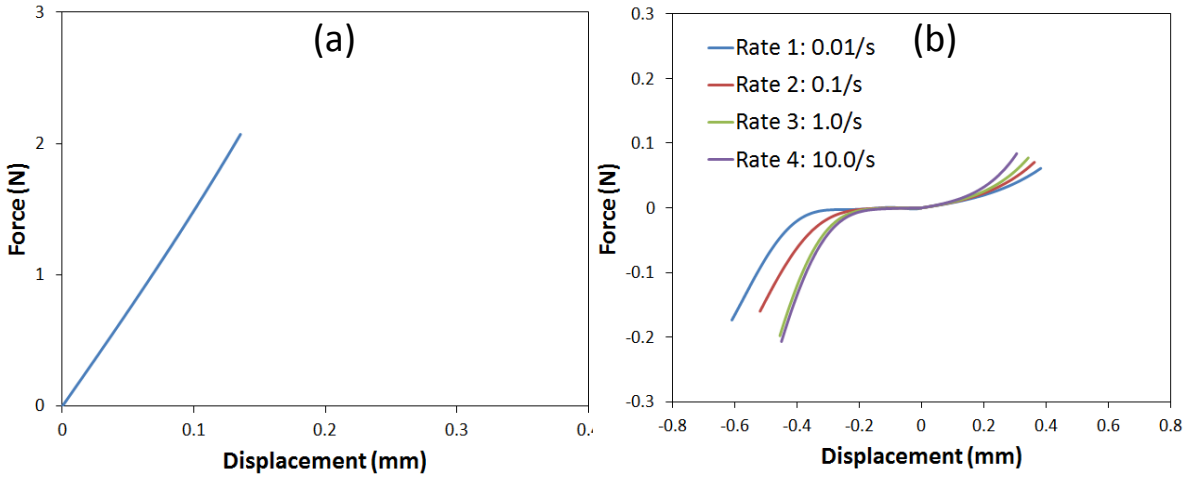

Figure 5.8. The average material model for human liver: (a) Capsule; (b) Parenchyma.

Table 5.5. Scaling factors for probabilistic human liver parenchyma tensile properties used in THUMS oblique impact simulations.

	$\alpha_{1SFTens}$	$\mu_{1SFTens}$	$\varepsilon_{fSFTens}$
Prob_Mat_01	-1.11	-0.01	1.53
Prob_Mat_02	-0.82	-1.58	0.51
Prob_Mat_03	1.35	-0.22	-0.59
Prob_Mat_04	-0.33	0.55	1.04
Prob_Mat_05	1.53	0.47	-0.21
Prob_Mat_06	-0.15	-0.53	1.68
Prob_Mat_07	1.01	-2.12	-0.50
Prob_Mat_08	-0.78	-1.81	1.86
Prob_Mat_09	0.31	-0.23	-1.06
Prob_Mat_10	-0.54	-0.31	-1.10
Prob_Mat_11	-0.13	0.60	1.05
Prob_Mat_12	-1.17	-1.85	-1.14
Prob_Mat_13	-0.87	-1.04	-0.27
Prob_Mat_14	1.75	0.16	-1.24
Prob_Mat_15	0.52	-0.01	-1.16
Prob_Mat_16	-0.42	1.22	-0.04
Prob_Mat_17	-0.04	0.96	1.74
Prob_Mat_18	0.05	-1.29	-0.37
Prob_Mat_19	0.08	1.32	-0.21
Prob_Mat_20	-0.23	-0.16	0.69
Prob_Mat_21	0.44	-0.09	1.02
Prob_Mat_22	-0.85	-0.17	-1.21
Prob_Mat_23	0.17	-0.51	-1.19
Prob_Mat_24	1.41	0.40	0.93
Prob_Mat_25	-0.36	-0.60	-0.59
Prob_Mat_26	-0.41	-0.71	0.06
Prob_Mat_27	0.64	-0.08	0.54
Prob_Mat_28	0.09	-1.12	0.31
Prob_Mat_29	1.23	0.61	0.06
Prob_Mat_30	1.30	-0.59	0.44

Table 5.6. Scaling factors for probabilistic human liver parenchyma compressive properties used in THUMS oblique impact simulations.

	$P_{1SFComp}$	$P_{2SFComp}$	$P_{3SFComp}$	$P_{4SFComp}$	$P_{5SFComp}$	$\varepsilon_{fSFComp}$
Prob_Mat_01	-0.77	0.37	-0.23	1.12	-1.09	0.03
Prob_Mat_02	0.28	0.03	-1.33	1.13	0.35	-0.30
Prob_Mat_03	-0.29	-0.85	-1.12	2.53	1.66	0.31
Prob_Mat_04	-1.12	1.26	0.66	-0.07	-0.20	-0.22
Prob_Mat_05	0.63	0.18	-1.03	0.95	0.31	0.14
Prob_Mat_06	-0.88	-0.48	-0.71	-1.17	-0.19	-0.27
Prob_Mat_07	-1.27	-0.38	0.65	0.83	-1.01	-0.47
Prob_Mat_08	-0.60	0.10	0.56	0.11	-0.90	-0.47
Prob_Mat_09	-0.28	-0.09	-1.47	0.19	-0.82	-0.09
Prob_Mat_10	-0.49	-0.18	0.05	-0.06	0.61	0.11
Prob_Mat_11	-0.20	0.33	-0.24	0.23	0.44	-0.62
Prob_Mat_12	-1.09	-0.43	-0.17	-0.22	0.54	0.39
Prob_Mat_13	-0.44	-0.41	0.98	-0.30	1.14	-0.53
Prob_Mat_14	-2.19	-0.33	0.71	0.32	0.41	-0.58
Prob_Mat_15	-0.01	-0.69	-0.67	0.86	0.11	0.40
Prob_Mat_16	0.58	-1.01	0.06	0.60	-1.36	0.35
Prob_Mat_17	-0.43	-1.63	0.17	0.38	-0.23	-1.15
Prob_Mat_18	-0.76	-0.56	0.56	-0.56	-0.90	-0.41
Prob_Mat_19	-0.13	-1.17	-1.39	0.31	-0.25	0.50
Prob_Mat_20	0.56	-1.12	-1.53	-1.10	-1.42	0.06
Prob_Mat_21	-0.87	0.41	0.35	0.35	-0.73	0.33
Prob_Mat_22	-0.30	-3.23	-1.09	-1.43	-1.01	-0.21
Prob_Mat_23	0.65	-0.35	0.05	-0.79	-1.55	0.17
Prob_Mat_24	-1.61	0.66	2.14	0.54	-1.54	-0.20
Prob_Mat_25	0.85	-1.85	-0.21	0.27	-0.65	0.48
Prob_Mat_26	-1.85	-0.40	-0.54	-0.91	0.65	-0.73
Prob_Mat_27	-1.26	1.11	-0.99	-1.83	1.38	-0.06
Prob_Mat_28	-1.17	-0.96	-0.65	-1.23	-0.27	-0.90
Prob_Mat_29	-1.47	-1.63	-1.96	2.61	0.97	0.26
Prob_Mat_30	-0.50	0.10	1.20	0.12	-1.04	-0.86

Table 5.7. Scaling factors for probabilistic human liver capsule tensile properties used in THUMS oblique impact simulations.

	$\alpha_{1SFCaps}$	$\mu_{1SFCaps}$	$\varepsilon_{fSFCaps}$
Prob_Mat_01	0.55	1.10	1.54
Prob_Mat_02	0.02	-0.26	-1.75
Prob_Mat_03	-1.26	-0.87	-0.18
Prob_Mat_04	-0.30	0.02	0.05
Prob_Mat_05	0.52	0.26	-0.94
Prob_Mat_06	1.53	-0.25	-1.06
Prob_Mat_07	0.14	-0.29	0.30
Prob_Mat_08	-0.12	1.48	-0.86
Prob_Mat_09	0.34	-0.90	-0.29
Prob_Mat_10	1.81	0.31	1.80
Prob_Mat_11	0.27	0.60	0.09
Prob_Mat_12	0.75	1.78	1.22
Prob_Mat_13	0.97	-0.52	0.18
Prob_Mat_14	0.14	-1.64	-0.76
Prob_Mat_15	0.88	0.18	0.55
Prob_Mat_16	-0.18	-0.94	-0.04
Prob_Mat_17	2.02	-2.36	-0.51
Prob_Mat_18	-0.16	0.41	-0.95
Prob_Mat_19	-0.89	1.91	0.12
Prob_Mat_20	-0.41	-0.37	-1.36
Prob_Mat_21	-0.51	-0.90	-1.20
Prob_Mat_22	-0.33	1.94	-0.57
Prob_Mat_23	-0.06	1.20	0.80
Prob_Mat_24	-0.50	0.38	0.41
Prob_Mat_25	-0.07	-0.94	0.16
Prob_Mat_26	0.54	0.98	-0.16
Prob_Mat_27	0.45	-0.36	-1.02
Prob_Mat_28	-0.29	-0.46	-0.41
Prob_Mat_29	-0.97	-1.15	0.55
Prob_Mat_30	-0.17	-0.19	-0.87

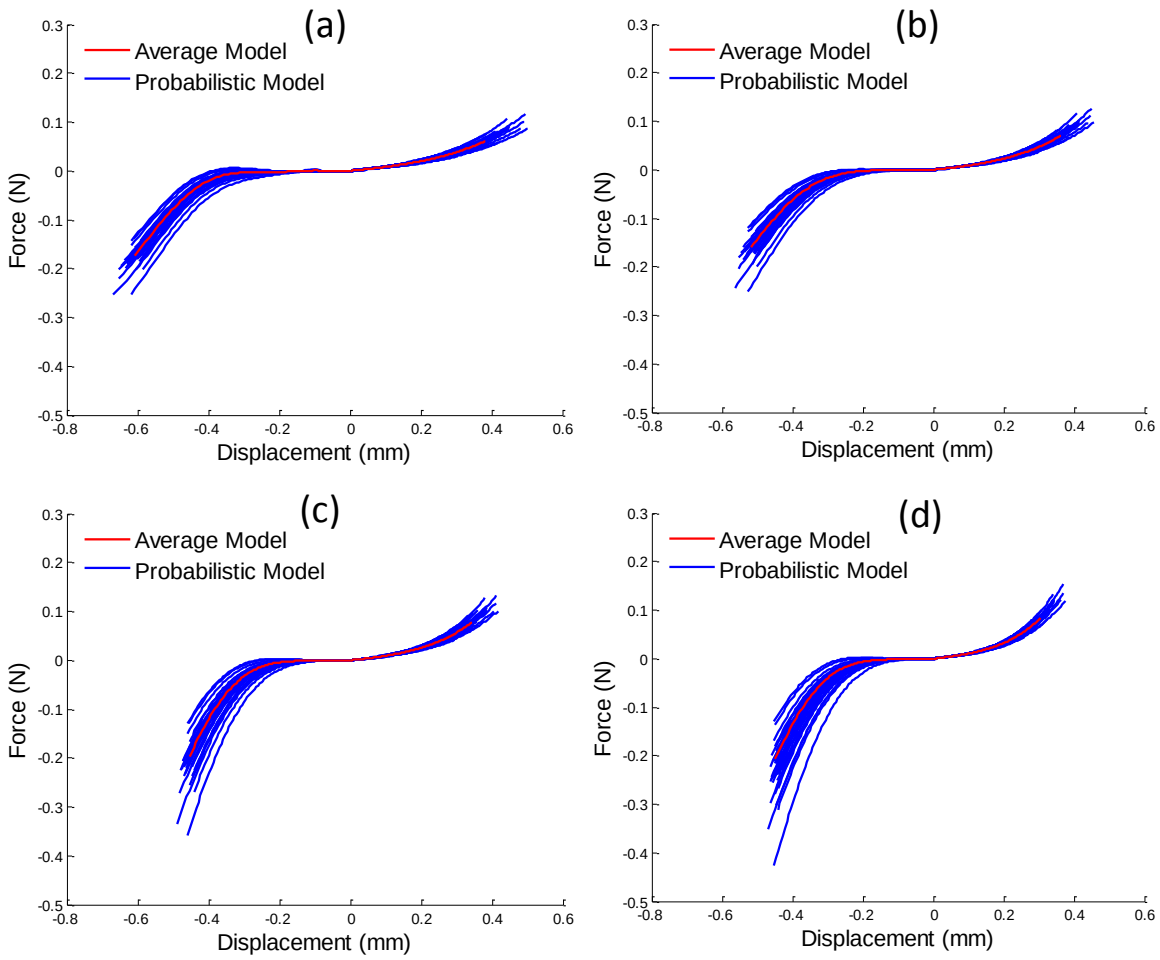

Figure 5.9. Tensile and compressive force-displacement input curves for the average and probabilistic human liver parenchyma material models used in THUMS oblique impact simulations: (a) Rate 1; (b) Rate 2; (c) Rate 3; (d) Rate 4.

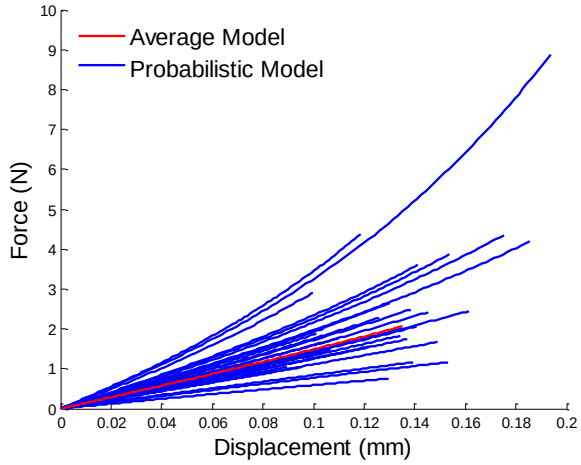

Figure 5.10. Tensile force vs. displacement input curves for the average and probabilistic human liver capsule material models used in THUMS oblique impact simulations.

5.3.4. Full-Body Behavior

The THUMS overall behavior during the oblique impacts at initial speeds of 4.79, 6.83, and 9.40 m/s are shown in Fig. 5.11, 5.12, and 5.13. In these three simulations, the updated average liver material models obtained from human test data were applied to the THUMS. The penetration of the abdomen increases from 15.20 cm to 24.61 cm when the impact speed increases from 4.79 m/s to 9.40 m/s.

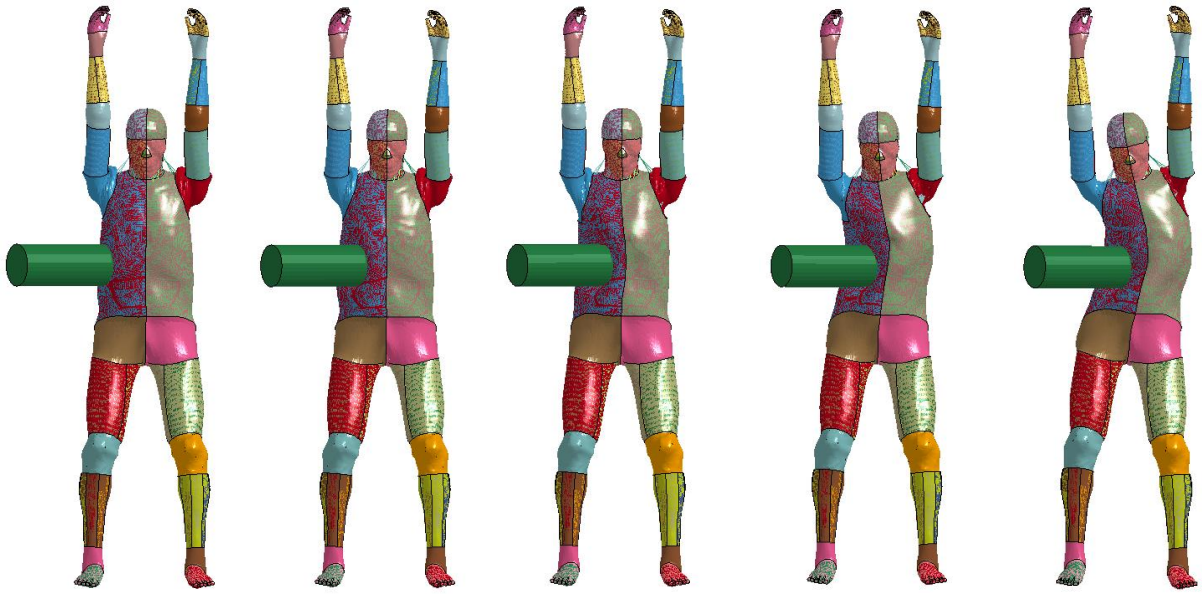

Figure 5.11. THUMS behavior at the impact speed of 4.79 m/s.

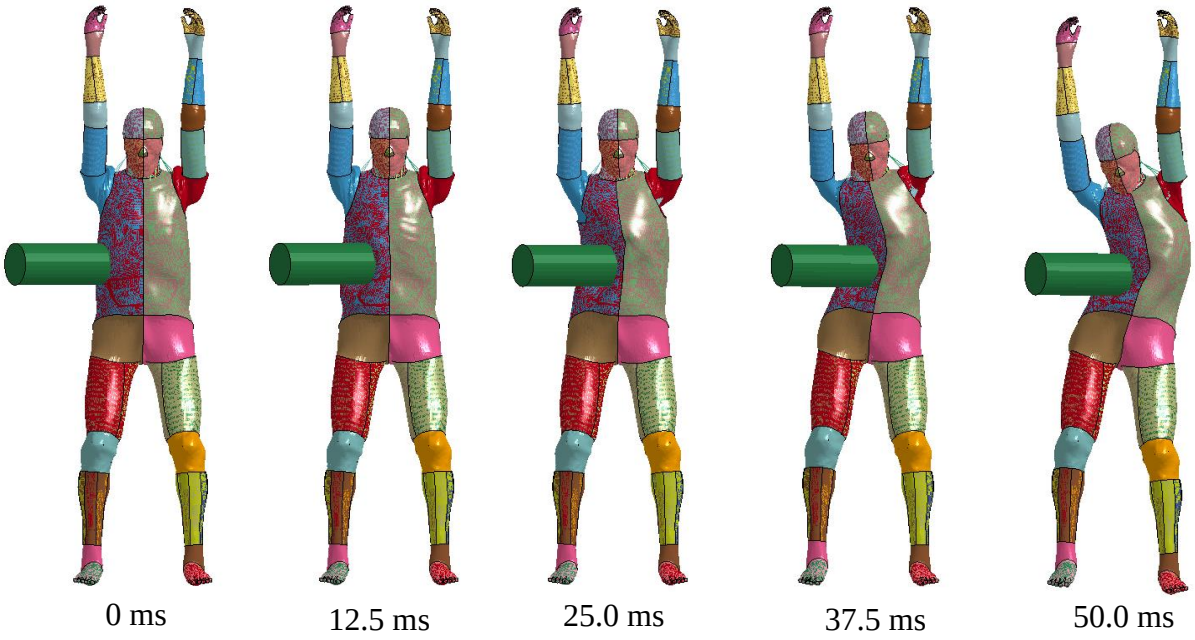

Figure 5.12. THUMS behavior at the impact speed of 6.83 m/s.

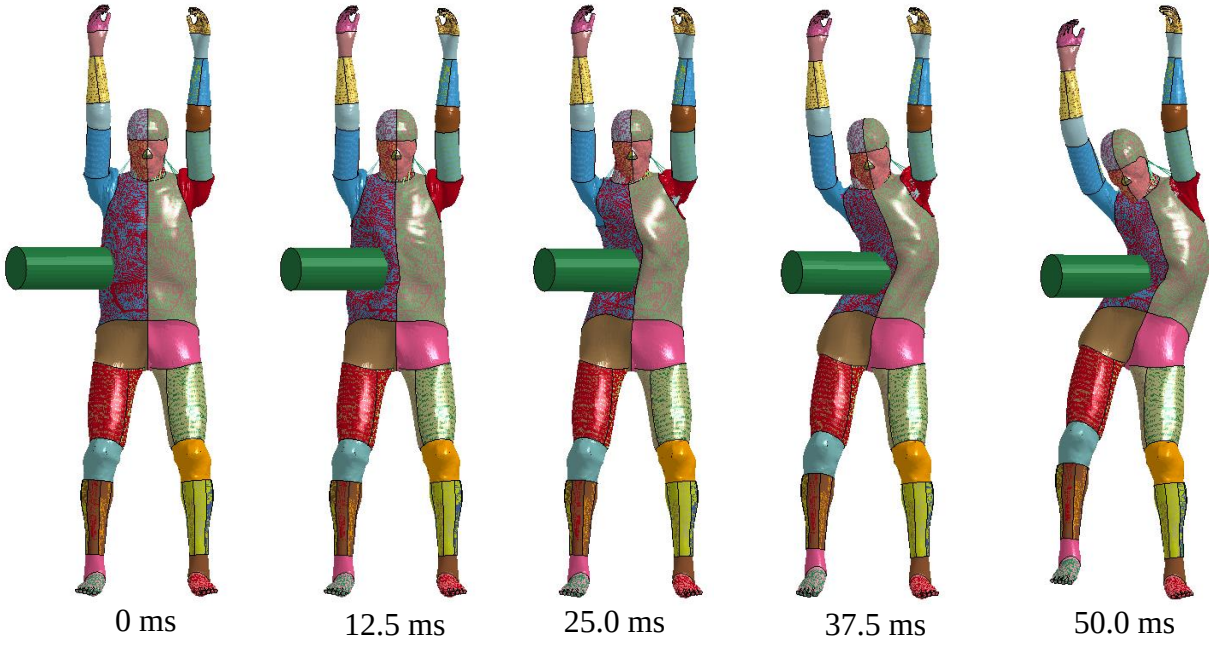

Figure 5.13. THUMS behavior at the impact speed of 9.40 m/s.

To compare the default THUMS liver material models and the updated average liver material models, the force-deflection histories and the force-time histories for the three impact speeds were plotted together with the test corridors published by Viano [3] (Fig. 5.14). The majority of the force-deflection and the force-time curves of both default and updated material models were within the test corridors.

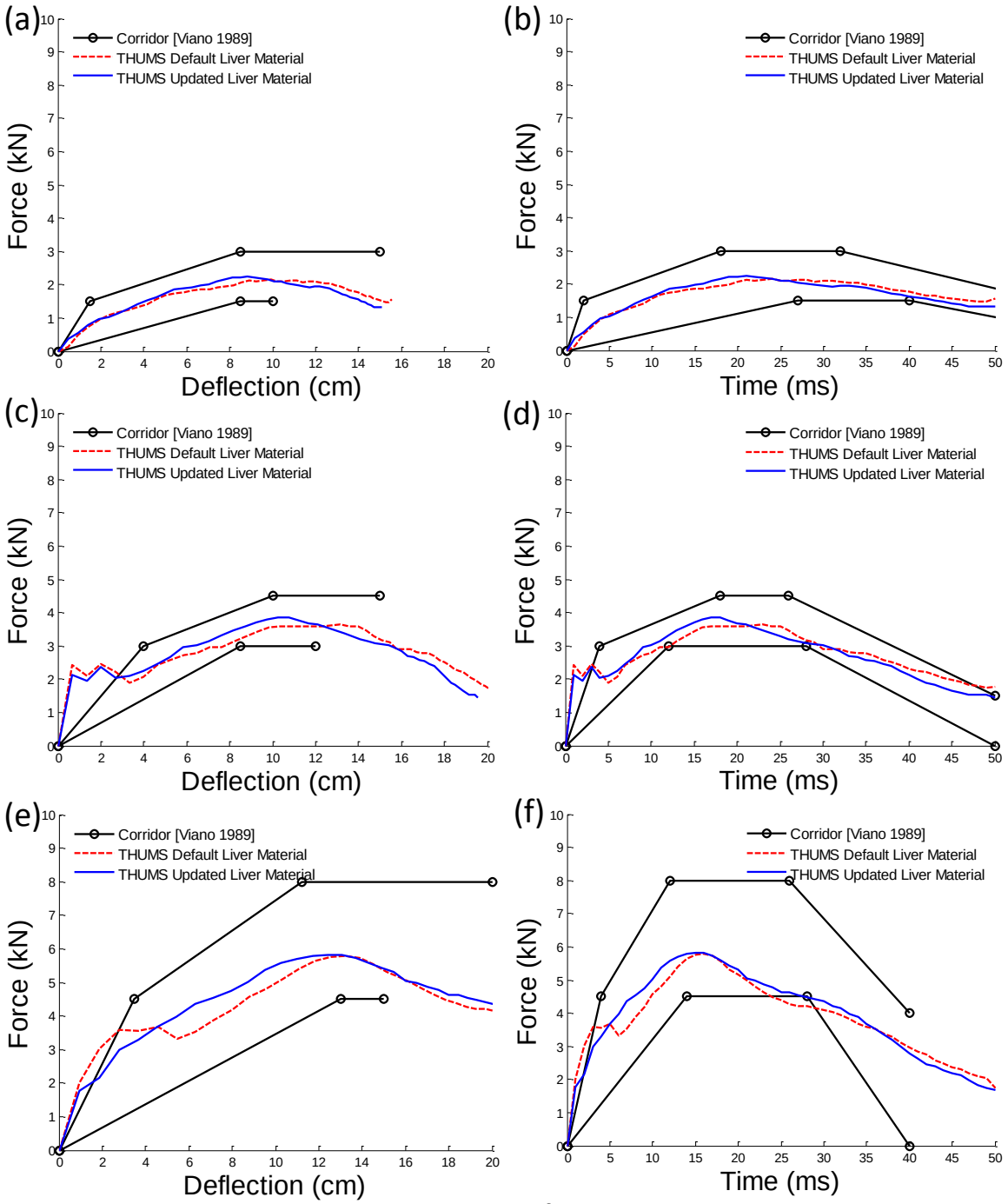

Figure 5.14. Comparisons between THUMS default and updated average liver materials in terms of force-deflection and force-time responses for lateral abdomen impacts at three test speeds. (a) and (b): 4.79 m/s; (c) and (d): 6.83 m/s; (e) and (f): 9.40 m/s.

The maximum tensile strain (Fig. 5.15a and 5.15b) and the maximum compressive strain (Fig. 5.15c) during the simulation time (50 ms) were determined from the simulation results. The default liver material models generated more than 70% higher maximum tensile strain than the updated liver material models in both capsule and parenchyma for all three impact speeds (Fig. 5.15a and 5.15b). In addition, the maximum tensile strain increased when the impact speed increased in all cases (Fig. 5.15a and 5.15b). In contrast, the updated liver material models generated slightly lower maximum compressive strain than the default liver material models for both capsule and parenchyma at all three impact speeds (Fig. 5.15c). However, these discrepancies of the maximum compressive strain between default and updated average material models were small (<5%) (Fig. 5.15c).

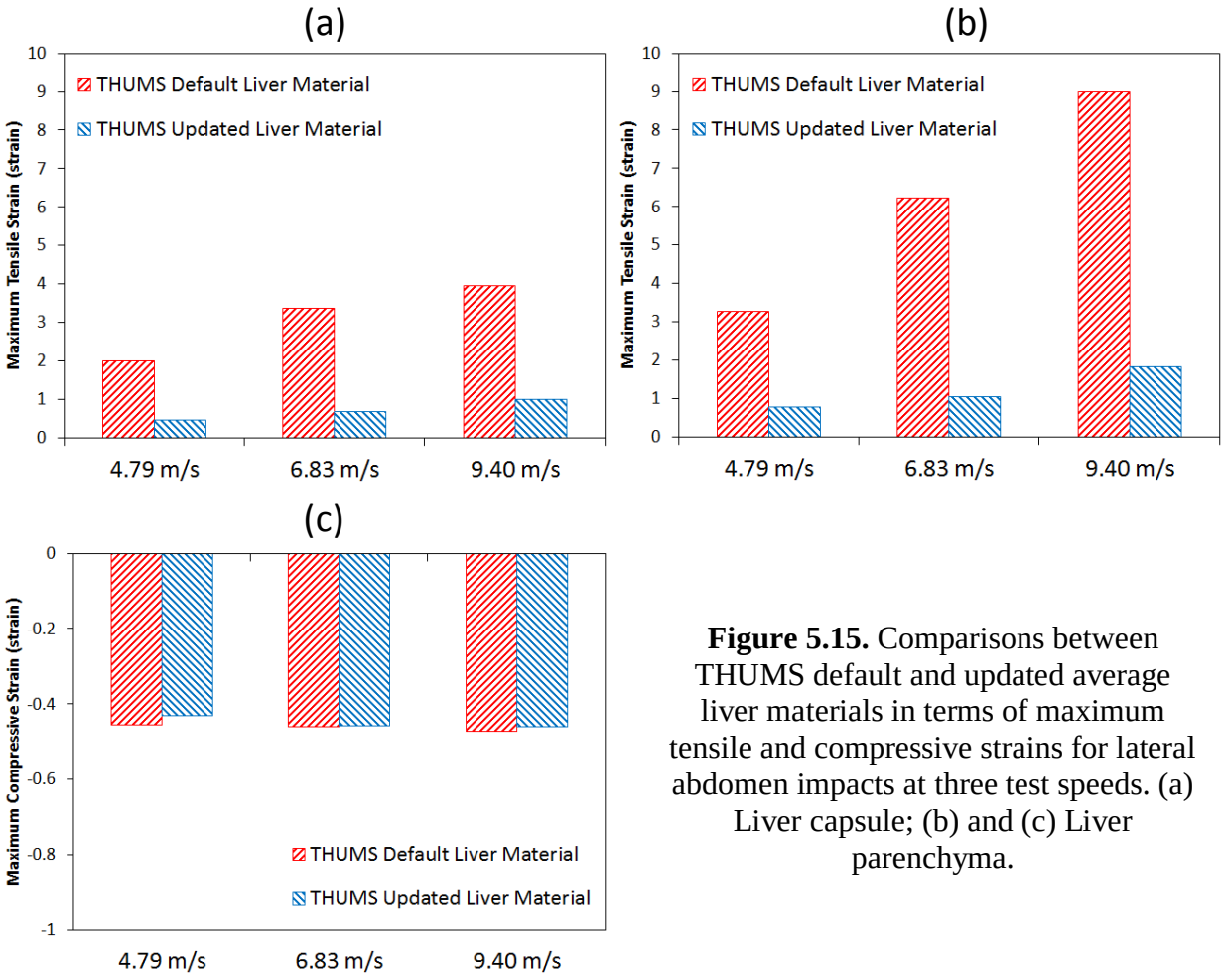

Figure 5.15. Comparisons between THUMS default and updated average liver materials in terms of maximum tensile and compressive strains for lateral abdomen impacts at three test speeds. (a) Liver capsule; (b) and (c) Liver parenchyma.

5.3.5. Probabilistic Liver Material Models

The thirty THUMS models created based on the probabilistic liver material models (Fig. 5.8, 5.9, 5.10) were simulated in three scenarios corresponding to three impact speeds: 4.79, 6.83, and 9.40 m/s. The corresponding force-deflection and force-time curves of the impactor from 90 THUMS oblique impact simulations were compared to the test corridors (Fig. 5.16). As can be

seen in Fig. 5.16, the majority of these force-deflection curves were well located within the test corridor [3].

Peak forces, times of the peak force, and absorbed energy values extracted from all simulations are shown in Fig. 5.17. The average peak forces were 2.28 kN, 3.78 kN and 5.82 kN and the average times of the peak forces were 20 ms, 17 ms, and 15 ms when the impact speeds were 4.79 m/s, 6.83 m/s, and 9.40 m/s, correspondingly. It was found that an increase in impact speed caused an increase in average peak force while a decrease in average time of peak force. Absorbed energy in each simulation was calculated as the integral of the force-deflection curve and is reported in Fig. 5.17c. The absorbed energy increases when the impact speed increases.

The maximum tensile and compressive strains in liver capsule and parenchyma for abdominal oblique impacts from the 30 probabilistic THUMS simulations are plotted in Fig. 5.18. As the impact speed increases, maximum tensile and compressive strains increase for both capsule and parenchyma. Paired two-sample t-test showed significant differences ($p<0.05$) of these strain values between every pair of two speeds.

While the ribs were modelled by the element elimination approach (i.e. deleting elements from the bone if they reached a prescribed threshold strain), the criteria for the liver injuries have not been defined in the THUMS Version 4 model yet [187]. However, the maximum tensile strain observed in simulations could be compared to the tolerance thresholds (i.e. failure GL strain) to predict abdominal injuries [187]. Using this approach, both the liver capsule and parenchyma in all our 30 probabilistic simulations and the simulation with the updated average liver material model were all suffered tensile/compressive injuries when comparing the maximum tensile/compressive strain values from the simulations with the corresponding liver failure GL strain values (strain rate: 10 s^{-1}).

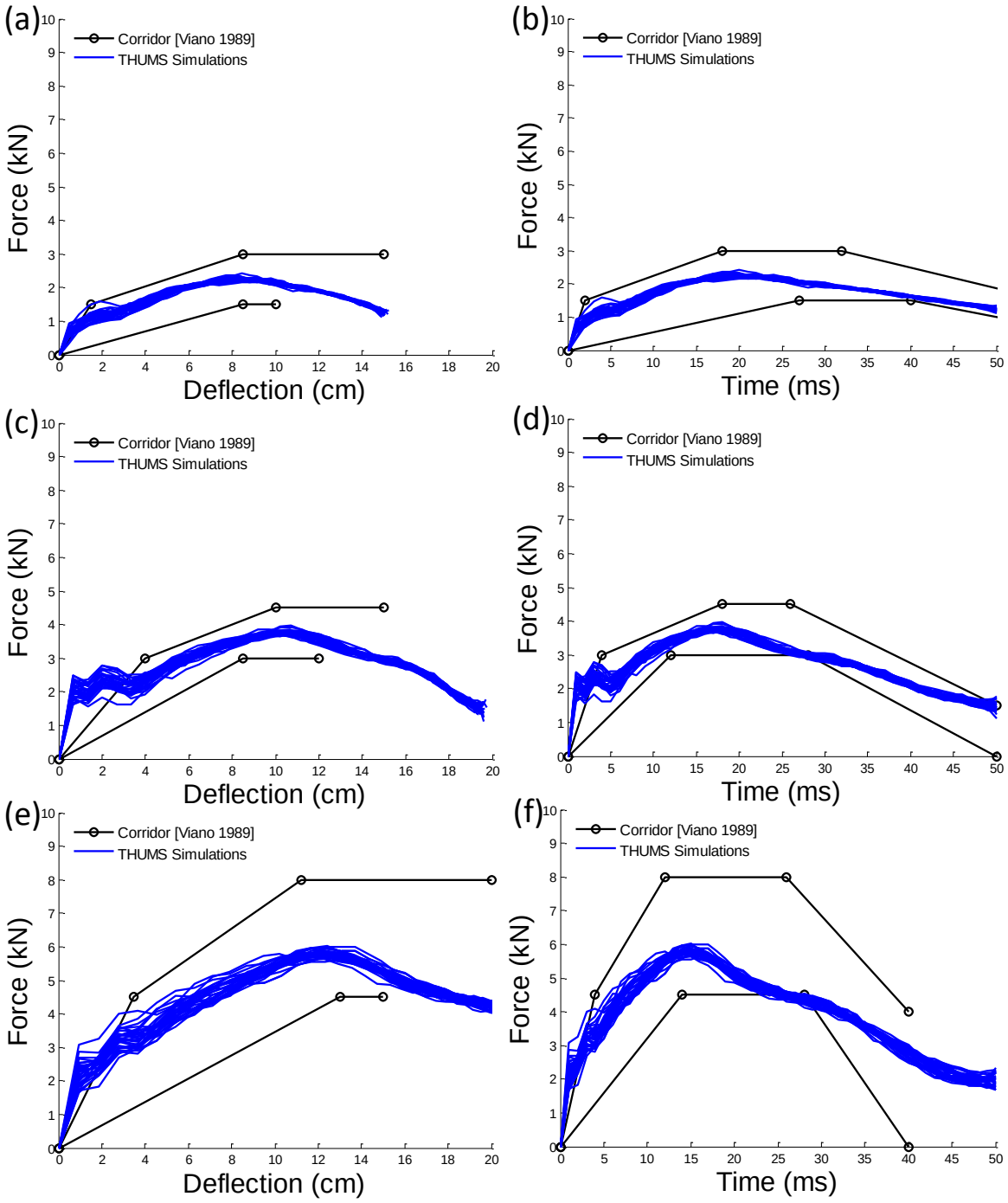

Figure 5.16. Force-deflection and force-time responses of 30 probabilistic THUMS simulations for lateral abdomen impacts at three test speeds. Each speed includes 30 simulations corresponding to 30 probabilistic liver materials. (a) and (b): 4.79 m/s; (c) and (d): 6.83 m/s; (e) and (f): 9.40 m/s.

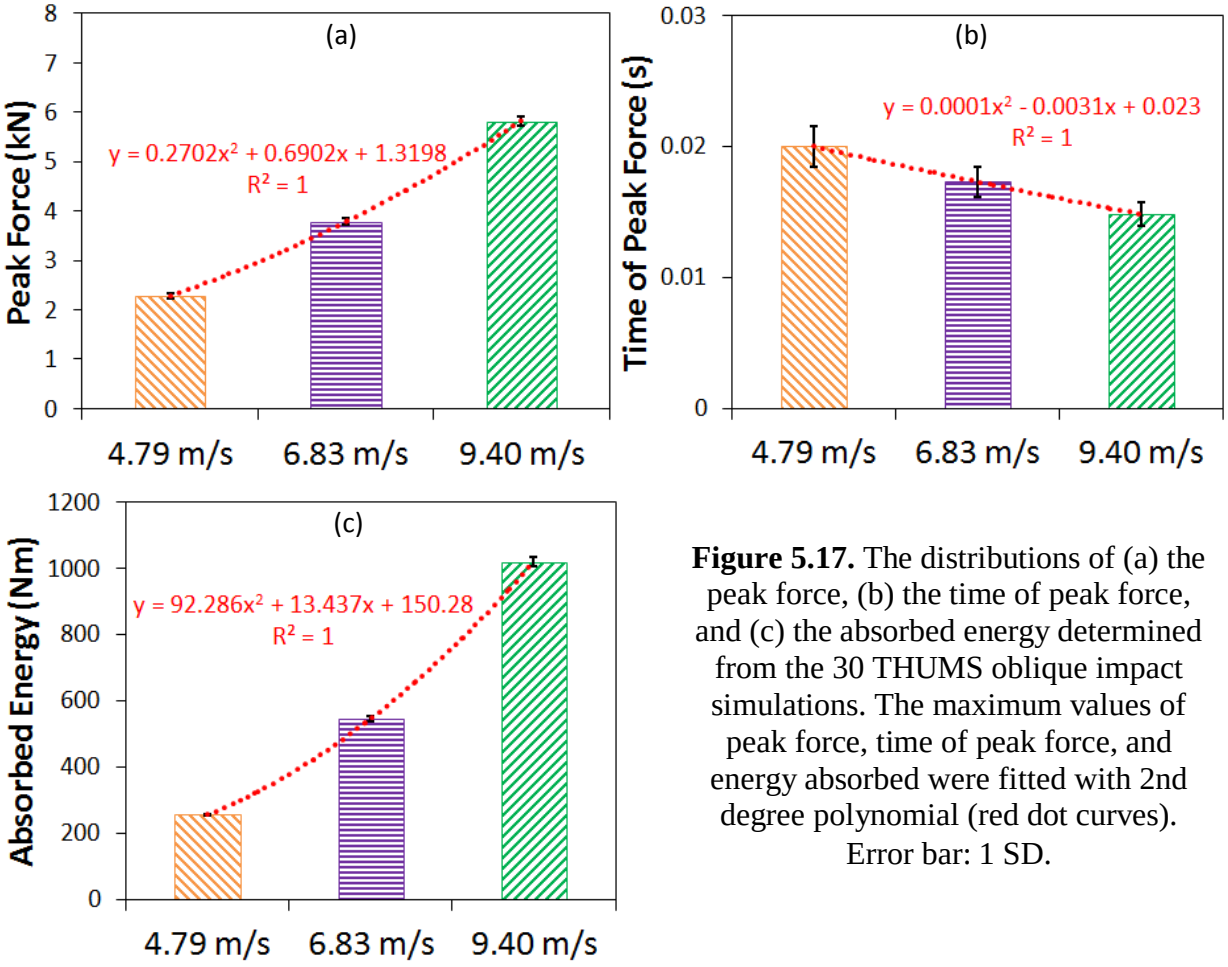

Figure 5.17. The distributions of (a) the peak force, (b) the time of peak force, and (c) the absorbed energy determined from the 30 THUMS oblique impact simulations. The maximum values of peak force, time of peak force, and energy absorbed were fitted with 2nd degree polynomial (red dot curves). Error bar: 1 SD.

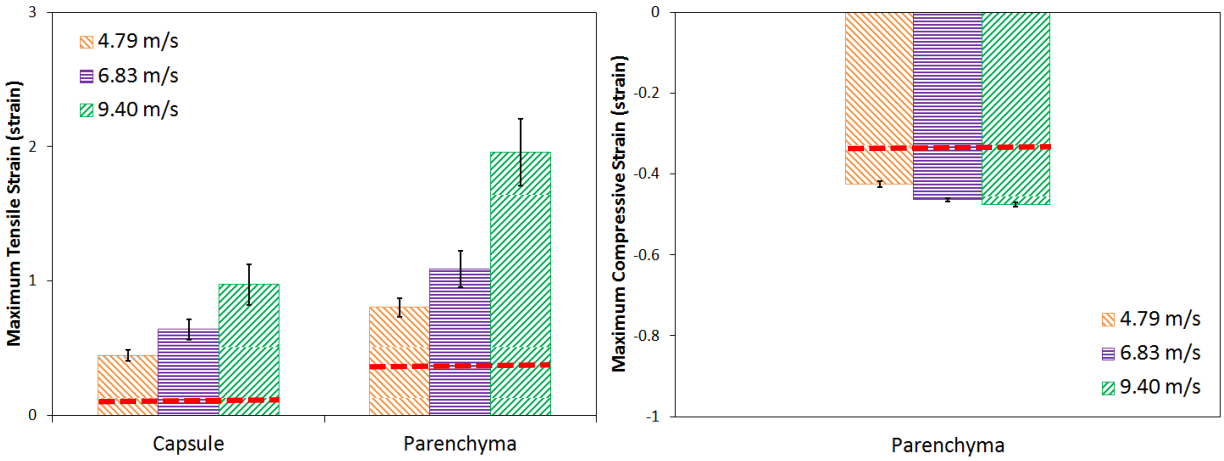

Figure 5.18. Comparisons between three test speeds in terms of (a) maximum tensile strain and (b) maximum compressive strain for oblique abdomen impacts for the 30 probabilistic THUMS simulations. Error bar: 1 SD. Red line: failure strain of the updated average material model.

5.3.6. Rib Injuries

Predicted rib fractures from the THUMS models using the average liver material models were noted and the locations of fractured ribs depending on the impact speeds are shown in Fig. 5.20. At the collision speed of 4.79 m/s, two rib fractures were observed (Rib #6 and #7). At the impact speed of 6.83 m/s, three ribs were fractured (Rib #6, #7, and #10) on the side of the body that collided with the impactor. At the impact speed of 9.40 m/s, a total of five ribs were fractured (Rib #6, #7, #8, #9, #10). All these predicted fractures occurred in ribs #6 through #10 on the strike side, with ribs #6 and #7 predicted to fracture in all three simulations (Fig. 5.19). Furthermore, it was found that the numbers of rib fractures predicted from THUMS simulations were within the test ranges [3] (Fig. 5.21).

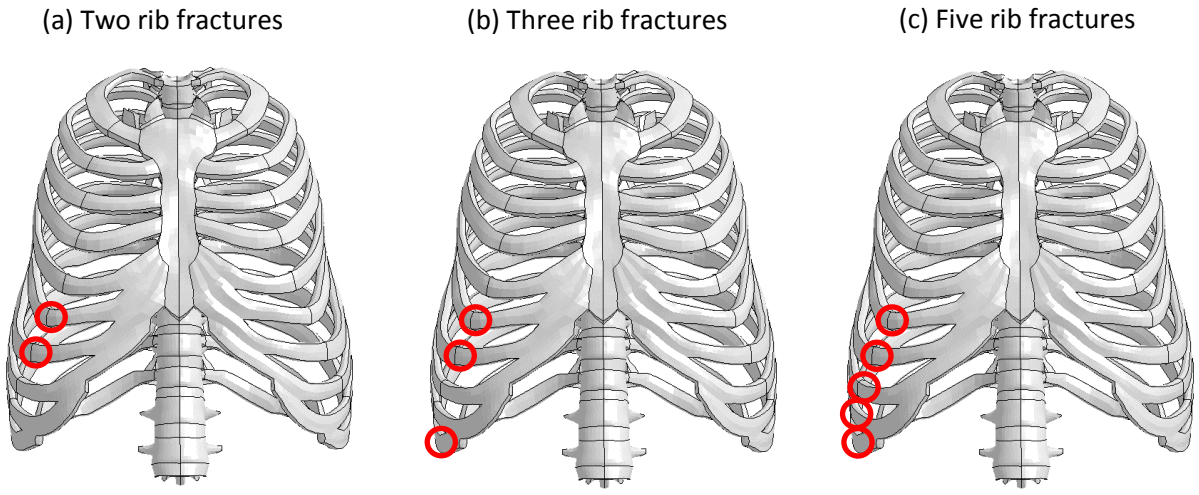

Figure 5.19. Location of rib fractures. (a) 4.79 m/s; (b) 6.83 m/s; (c) 9.40 m/s.

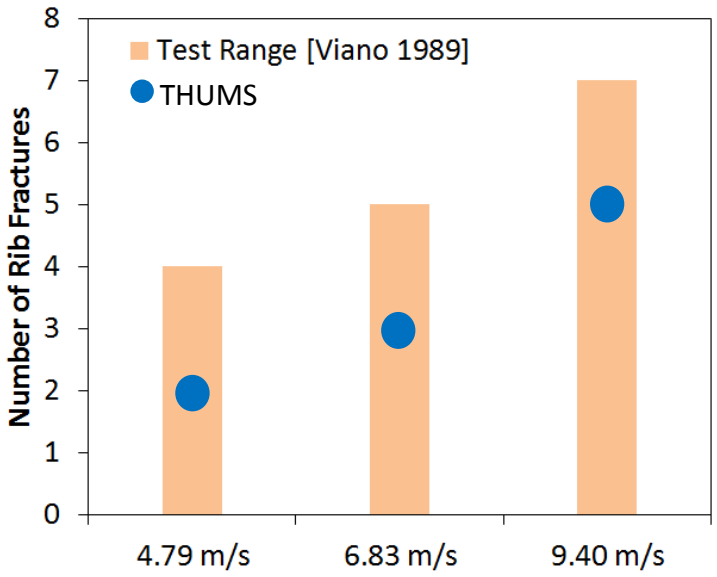

Figure 5.20. Number of rib fractures.

5.3.7. Liver Injuries

The contour maps of the 1st principal GL strain ("tensile strain") observed in liver capsule and liver parenchyma are shown in Fig. 5.21 and Fig. 5.22 correspondingly for the THUMS models with updated average liver material properties. The range of tensile strain that exceeded 40% [20] in the liver capsule at an impact speed of 4.79 m/s was localized (an area of less than 5% of the total area of the liver capsule). Similar trend was found in higher impact speeds with higher tensile strain values. The maximum tensile strain was located at the posterior region of the liver capsule where the two liver lobes connected for all impact speeds (red circle in Fig. 5.21). This is also the region where the gallbladder was embedded. Similarly, the high tensile strain concentrations were located in the posterior region of the liver parenchyma where the two liver lobes connected (red circle in Fig. 5.22). These high tensile strain locations are corresponding well to the areas reported by Watanabe et al. [187], who simulated automotive side impact scenarios with whole body THUMS pedestrian models.

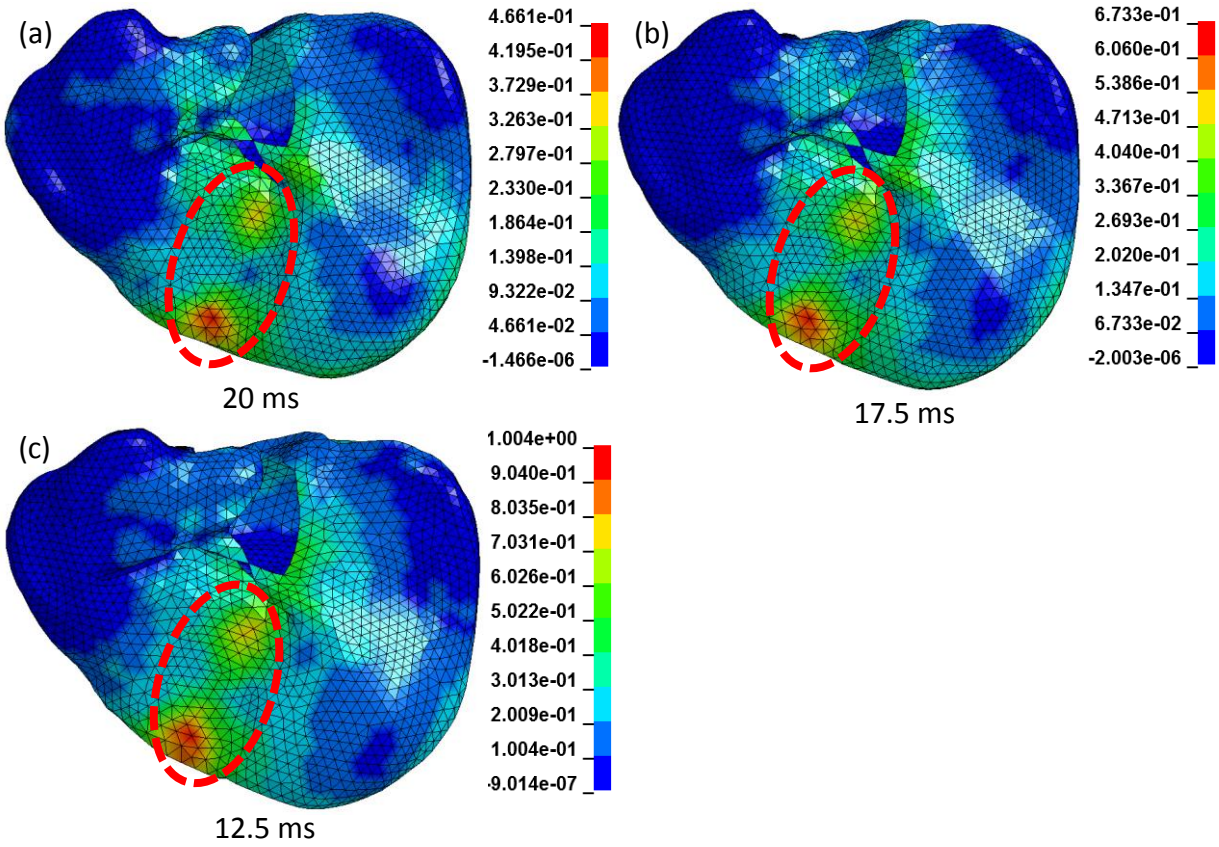

Figure 5.21. Posterior view of the contour maps of 1st principal Green-Lagrangian strain ("tensile strain") in liver capsule: (a) 4.79 m/s; (b) 6.83 m/s; (c) 9.40 m/s. Red circle: the location of gallbladder.

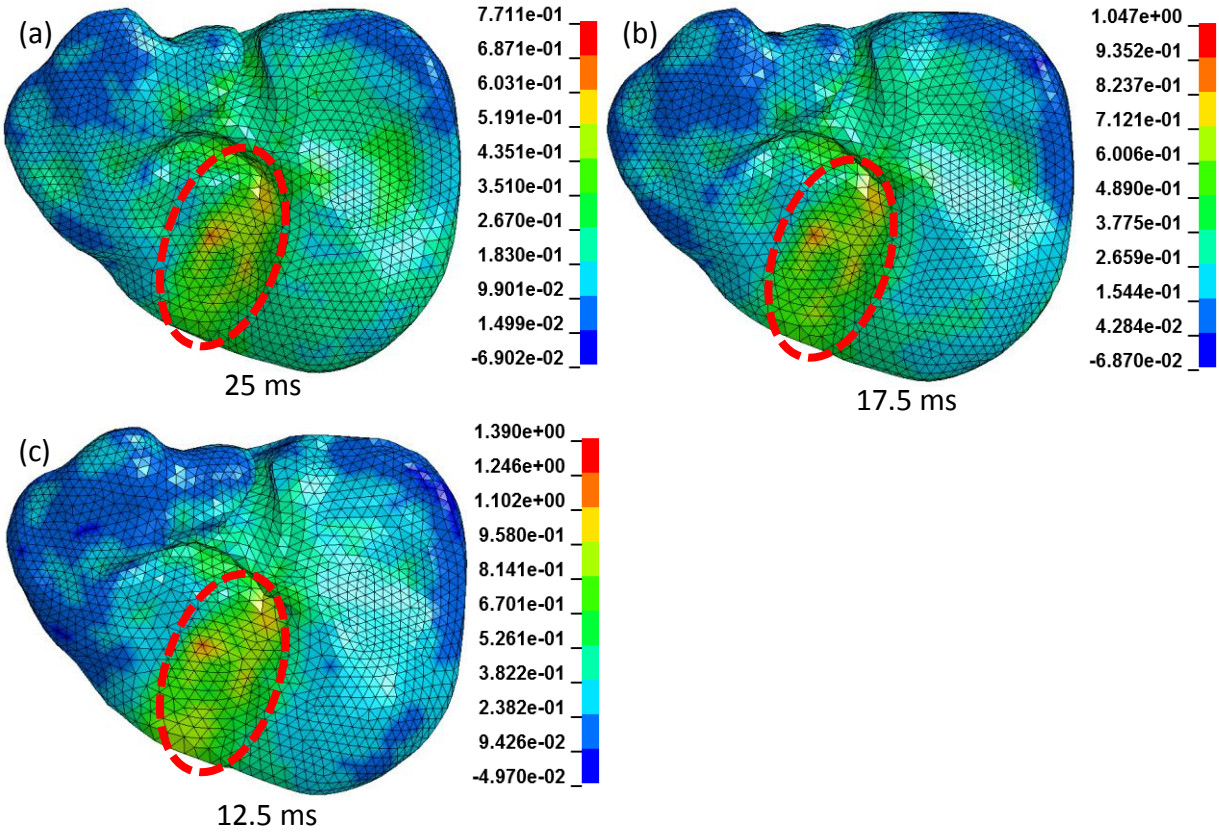

Figure 5.22. Posterior view of the contour maps of 1st principal Green-Lagrangian strain ("tensile strain") in liver parenchyma: (a) 4.79 m/s; (b) 6.83 m/s; (c) 9.40 m/s. Red circle: the location of gallbladder.

The contour maps of the 3rd principal GL strain ("compressive strain") observed in liver parenchyma are shown in Fig. 5.23 for the THUMS models with updated average liver material properties. The minimum compressive strain values were lower than -0.48 for capsule at all three test speeds. High compressive strain areas were found at the posterior of the liver where the two lobes were connected (blue areas in Fig. 5.23). In addition, these high compressive strain areas increased when the impact speed increased (red circle in Fig. 5.23).

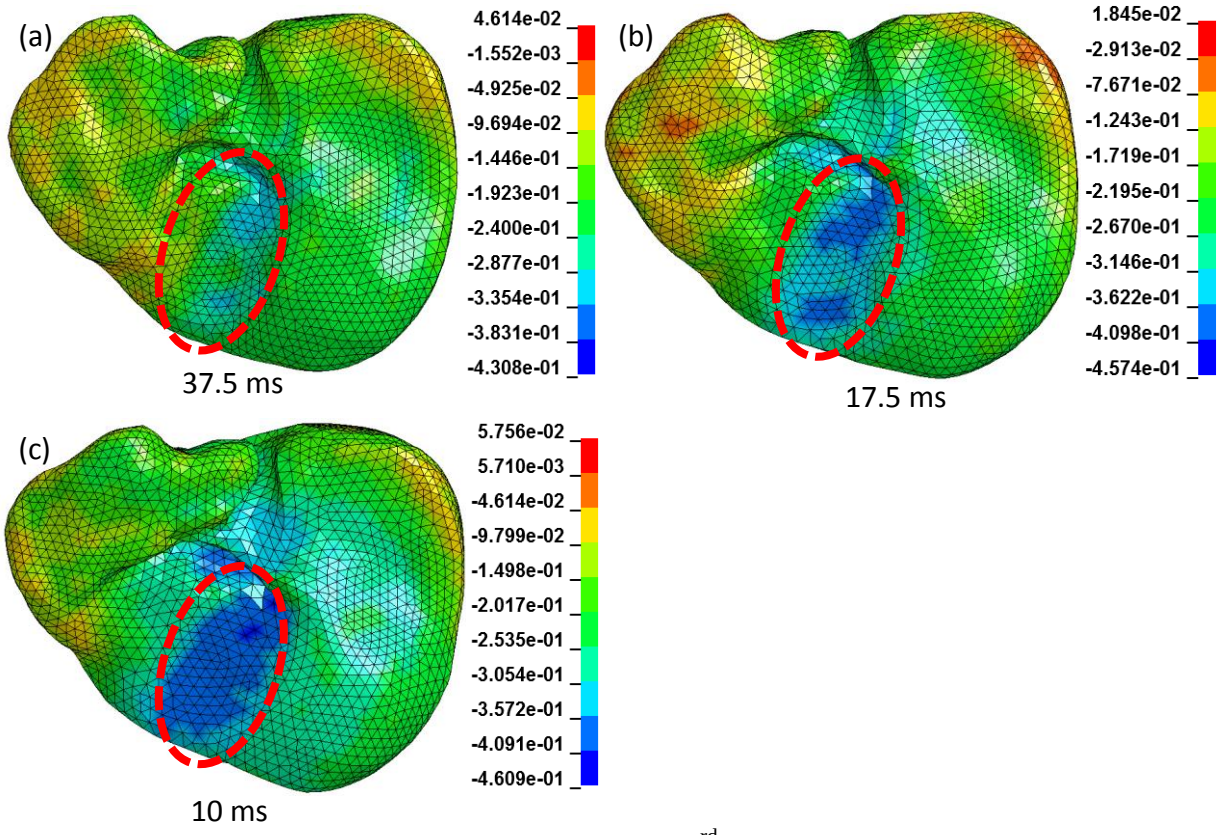

Figure 5.23. Posterior view of the contour maps of 3rd principal Green-Lagrangian strain in liver parenchyma: (a) 4.79 m/s; (b) 6.83 m/s; (c) 9.40 m/s. Red circle: the location of gallbladder.

5.4. Discussion

This is the first study to conduct the probabilistic investigation of the influence of liver material property variations on the liver mechanical and injury responses under blunt impact. While there is small discrepancy between the default and updated average liver material models in terms of the force-deflection and force-time curves, the corresponding curves of both models were within the test corridors [3] for all three impact speeds [185-187]. However, significant differences were observed when comparing the 1st and 3rd principal GL strain values between the default and updated average material models. The maximum 1st principal GL strain values from the updated models were less than the strain values from the default model due to the higher stiffness values from the updated average liver models (Fig. 5.3 and 5.8). The default liver material models in THUMS contains only one strain rate, which was obtained from low strain rate testing using porcine liver specimens (0.05 s^{-1}) [7]. Thus, the current study provides probably more biofidelic material properties derived from fresh human liver specimens.

High 1st principal GL strain values were observed in the posterior of the liver between the two lobes, which could be the potential locations of liver tensile injuries predicted by the model (Fig. 5.21, 5.22). These high strain concentration locations could be explained by the contact interaction between surrounding organs/bones and the liver. The gallbladder is located at the

lower posterior portion of the liver, creating a concave surface on the liver (Fig. 5.2c), and it is supported by the duodenum, large intestine, thoracic aorta, and inferior vena cava. During the impact event, the impactor caused the ribs and costal cartilage to hit the anterior part of liver, and it was resisted on the back of the liver by the gallbladder and its supporting solid organs and vessels, squeezing the liver at this concave area. In addition, the original shape of the liver model in THUMS is curved from the superior view, and during the impact event, the liver was pressed to become "flatter." Therefore, the liver encountered a large tensile strain deformation in the posterior area between the two lobes where the bladder is located.

The anterior liver parenchyma was sustained the compressive effect caused by the impactor at the early stage of the impact event, but the maximum compressive strain values were actually observed in the posterior part of the liver parenchyma between the two lobes (Fig. 5.23). This could also be explained by the strong posterior support of the concave areas where the gallbladder is located and the surrounding organs/vessels, so the liver parenchyma reached a significant compressive effect in this region. In addition, the shear effect was also observed on the liver in the oblique impact. The maximum 1st principal stress ("maximum tensile stress"), minimum 3rd principal stress ("maximum compressive stress"), and maximum shear stress were calculated from the simulation results (Fig. 5.24). It was shown that the relative magnitude of shear stress was close to the tensile stress for both liver capsule and parenchyma. The maximum compressive stress, however, showed higher magnitude than the maximum tensile stress for liver parenchyma. This demonstrated that the dominant mode of loading in an impacted liver is compression. In the current study, only the experimental tensile testing of human liver tissues were conducted due to the immediate availability of the tensile testing facility in the lab (Chapter 4), and it was used as our first step to demonstrate the development of the probabilistic models using FE optimization and stochastic optimization. More experimental shear and compression tests along with FE optimization are suggested in future studies to obtain better shear or compression material models, for the validation of the impacted liver in the oblique impact simulations.

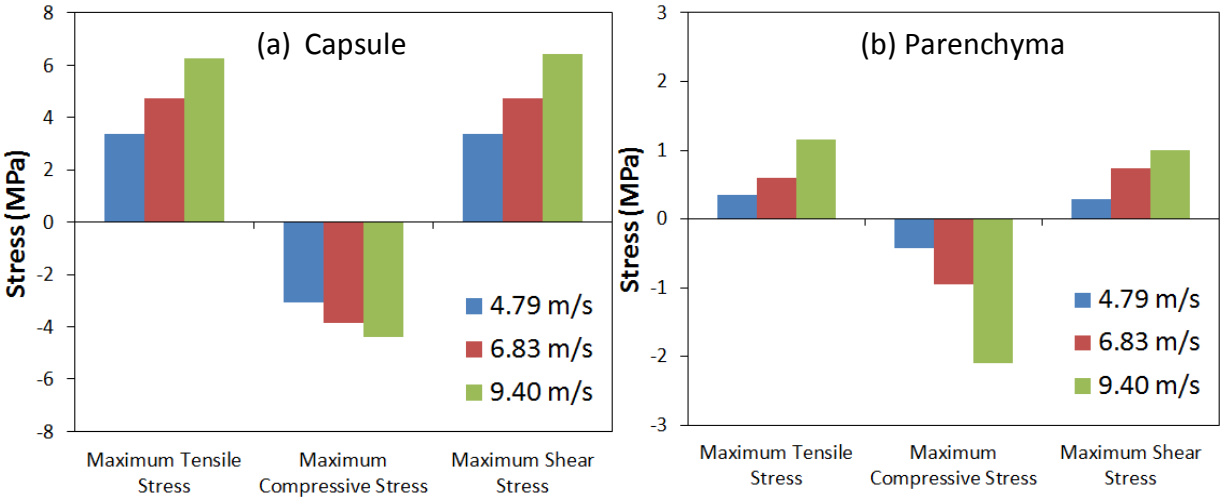

Figure 5.24. The maximum tensile stress, maximum compressive stress, and maximum shear stress of the liver capsule and liver parenchyma for the three testing speeds (4.79 m/s, 6.83 m/s, and 9.40 m/s).

In Viano's studies [3, 4], only the livers tested at high oblique impact speed (9.40 m/s) were injured. However, the livers were found injured in all THUMS FE simulations when comparing the maximum tensile/compressive strain with the tolerance thresholds (i.e. failure GL strain). These maximum tensile/compressive strain values were due to the direct contact between the liver and its surrounding organs/vessels such as the gallbladder and thoracic aorta. In addition, the relative locations between the liver and surrounding organs/vessels may vary due to subject-to-subject variations in experimental testing. While not all of the livers were found injured in the experimental testing, further validation of the liver and surrounding organs/vessels should be conducted in future studies.

The locations and number of rib fractures are common indices for the evaluation of the human computational models [26, 187]. Watanabe et al. conducted lateral chest impact tests using THUMS at two loading speeds, 4.5 and 6.5 m/s, and they found that the predicted numbers of rib fractures were within the test range [3, 187]. Similarly, Vavalle et al. simulated oblique impacts on Global Human Body Models Consortium (GHBMC) 50th percentile male abdomen and compared the number of rib fractures under several impactor locations [26]. In the current study, the numbers of rib fracture were also found to be within the test range for all three impact speeds, where higher speed could cause more rib fractures. In addition, rib #6 and #7 were two most commonly injured ribs for all impact speeds in simulations, and rib #6-#10 were all injured in high speed testing (9.40 m/s). These observations correspond well to the experimental findings [3]. Therefore, based on the results, it was shown that the THUMS Version 4 model with the updated average liver material model could predict well the number and location of rib fractures.

The current study investigated only effects of the variations of material properties on the biomechanical responses of the human body. However, as can be seen in Fig. 5.16, variations of the force-deflection and force-time curves were small comparing to the test corridor. To have a full scope of probabilistic models, more statistical factors would be suggested to consider in future studies to account for more variations to match the test corridor width. For example, the

external loading or impactor boundary conditions could also be considered as probabilistic input factors [188, 191]. A recent study conducted by Vavalle et al. [190] investigated four more impactor locations in addition to the nominal location and also investigated three impactor speeds (6.4, 6.7, and 7.0 m/s) using GHBMC 50^{th} percentile male model to simulate oblique impacts [3, 4]. They found that within a small range of variations of the impactor locations and speeds, the peak force, absorbed energy, and the number of fractured rib could vary. While the input variations were not distributions, their study observed that these impact responses could be altered when changing the loading and boundary conditions. It is also interesting to investigate other variations such as the size, shape, and mass of organs/whole body, mesh density, contact algorithms, and the posture of the model. All of these other input factors may potentially improve the match between computational and experimental results further.

The peak force and the absorbed energy of the 30 probabilistic simulations were found to be dependent on the impactor velocity. In Fig. 5.17, it is seen that for each impact speed, the variations of these values were small, and these values increased when impact speed increased. These small variations caused by the liver material properties on the whole body reaction could be explained by the location of the liver in the abdomen. The liver is covered by the ribs and fat layers, which could reduce the effect of the material properties of the liver on the overall abdomen response (e.g. the peak force and absorbed energy). In addition, the force-deflection and force-time curves of the probabilistic models (Fig. 5.16) demonstrated a smaller corridor than the test corridor, which may suggest that the anthropometry variation in subjects may play a significant role as well. On the other hand, larger variations were observed in terms of the principal GL strain between subjects in each impact speed (Fig. 5.18). Thus, the probabilistic liver material properties do have influence on its reaction to the external loading. To cover a wider range of variability, the material and shape properties of other organs or bones should also be incorporated in future studies.

Some limitations are discussed here. First, the strain rate dependency was not considered for liver capsule in this study. The fresh human liver capsule testing referred in this study was conducted under a low strain rate (10^{-3}-10^{-2} s^{-1}), and there is no available strain rate dependent data for human liver capsule yet. In most automotive crash events, the liver may encounter a wide range of strain rate [2, 86]; therefore, this strain rate dependency for liver capsule should be further examined and then implemented in liver models. In addition, the current study utilized the oblique impact simulations to verify the updated material model and probabilistic models. While the oblique impact testing was one of the best ways to perceive the effect of the probabilistic liver material properties on biomechanical responses because of the contact of the impactor and the abdomen region, more testing data such as whole body impact/belt loading tests with more instrumentation/imagining equipment (e.g. high-speed, dynamic x-ray tests [25] and liver pressure sensors) focused on the responses of the liver (e.g. the deformation of internal organs or the contacts between organs) for validating the FE models of abdominal organs will be desired. These types of experimental tests could be used to validate the responses of the liver in the body. In addition, the material models of liver parenchyma compressive property and liver capsule tensile property were derived from previous experimental studies [1, 159]. These studies, however, assumed constant thickness along the specimens to calculate stress-strain behaviors. Therefore, the FE optimization approach using the actual specimen geometries utilized in Chapter 4 should be implemented in future studies to obtain more accurate material models.

Chapter 6

Conclusion

6.1. Contribution

The current study provides an insight of the shape and material property variations of the human liver. Results from the statistical shape models and material models could be applied to the probabilistic analysis on the human liver. Several specific achievements are listed as follows.

(1) Development of the statistical size and shape models of the human liver. Mean and boundary models of these organs were proposed and then constructed.

(2) Investigation of the storage effects (cooling and freezing) on the material properties of porcine and bovine livers. Two different tests, indentation and tensile tests, were conducted in this investigation.

(3) Development of the distributions of material model parameters of the human liver using tensile tests with four loading rates (0.01, 0.1, 1.0, and 10.0 s^{-1}). Two approaches were conducted: marker data analysis and specimen-specific FE analysis.

(4) Development of probabilistic FE models of the human liver. These probabilistic models were implemented in a commercial full-body human FE model, THUMS, and tested under impact loading.

The novelty of this study includes:

(1) Conducted statistical size and shape analysis on human liver, considering both the size and shape variations in seated posture. This is also the first study to propose the "boundary shape models" for the construction of variation shapes using the statistical shape analysis.

(2) Provided optimized material model parameters and their SD at various loading rates for human liver capsule and parenchyma.

(3) Implemented a FE probabilistic analysis for impact simulations, considering the variations of the liver material properties. This is also the first study to conduct the probabilistic analysis on a human internal solid organ.

This study contributed significant scientific values to several aspects of injury biomechanics. First, this study established a standard procedure for constructing the "boundary shape models," which could be used for future studies for investigating the injury of the human liver due to the shape variations. Second, this study found that the preservation could significantly change the biomechanical properties of the liver under freezing preservation and therefore suggested that the material models for the FE models should be obtained from fresh tissue experimental testing data. Third, new material models for the human liver were proposed based on fresh human liver testing data. The developed material model, along with the distributions of the model parameters, can be used for the improvement of material properties of future full-body human FE models. Lastly, this study conducted the first probabilistic analysis on

internal organs of human FE models in biomechanics research. This study also proposed a procedure for conducting the probabilistic analysis on the human liver, and this established procedure can be used for future human body probabilistic models.

Overall, this study provided a novel investigation on the human liver using a probabilistic approach rather than traditional deterministic approaches. The results from this study can contribute to the fields of biomechanical studies and probabilistic analysis for injury investigations, and the approaches utilized in this study can be applied to other human abdominal tissues.

6.2. Future Work

Due to the limited number of subjects recruited in the current liver statistical shape analysis, more volunteers would be desired to obtain more robust results. In addition, gender and age effects could have influences on size, shape, and location of the human abdominal organs [71, 78, 192]; therefore, the gender and age effects should be considered in future statistical shape analysis by recruiting a wider range of subjects. The established statistical shape analysis procedure could be applied to other abdominal organs and body segments to attain a full scope of the size and shape variations of the human body.

Different loading types could be observed in the automotive crash events. The current study conducted tensile experimental testing on fresh human livers as our first step in the probabilistic analysis. Other types of loading should be conducted on tissue specimens, such as the compression [159] and shear loading [193], and the corresponding FE material models could be obtained by applying the FE optimization techniques proposed in this study. In addition, the material model developed from the liver capsule tensile testing experimental data without FE optimization techniques involved. Therefore, the capsule tensile testing data should also be improved in future studies. Furthermore, human liver parenchyma exhibits clearly the strain rate dependency for both tensile and compressive properties, and the liver capsule should be further examined for this phenomenon and corresponding material models with strain rate dependency should be developed if necessary.

It has been shown that the biomechanical properties of soft tissues could change in most preservation scenarios; however, most of previous studies conducted these evaluations based on the animal tissues (mostly bovine and porcine). While some histology studies have shown the structural similarity between the fresh animal and human abdominal organs, there is a need to extend these preservation investigations to human abdominal organs at various loading types and loading speeds. In addition, more effort should be placed on the investigation of the *in vivo* liver properties to obtain better liver material models.. This study conducted a pioneer comparison between the cooling and freezing effects using the indentation testing and longitudinal data analysis to statistically compare the changes of the tissues under different preservation temperature. These effects could be further examined for human abdominal tissues in a wider range of preservation temperature and period or extreme environmental conditions, and these examinations could be used as references for future material model development.

The Ogden material model was selected to simulate the tissue responses in tensile testing in the current study but not used for the compression testing data. It was observed that the liver parenchyma compression data contain a long period of “closely zero strain” in each stress-strain

curve, and the 5th degree polynomial showed the best fit to the compression data. However, there were still some discrepancies between the compression experimental data and fitted polynomial curves, especially in the "closely zero strain" regions. Therefore, more complex material models such as higher degree Ogden material models with more parameters should also be examined and compared to determine the best material model of the compression data in future studies.

The current probabilistic study focused on the variations of the liver material properties as the input variable, and considered three different loading speeds. The developed liver average and boundary shape models from Chapter 1 was not used in the probabilistic FE analysis in Chapter 5 because the liver shape models could not be fitted in THUMS abdomen when surrounding organ/vessel sizes and locations were fixed. Therefore, the proposed statistical shape analysis can be applied to other organs to investigate their shape variations and their relative locations in abdomen in future probabilistic studies considering the shape variations.

Several probabilistic models have been proposed in the literature. The current study utilized the most commonly applied and most reliable probabilistic model, the Monte Carlo method. While the Monte Carlo method can always converge to the correct solution with a large number of trials, it is usually computationally expensive and time consuming because of the large number of trials required for an accurate estimation of the output [188, 189]. The Monte Carlo method can be coupled with the Latin Hypercube sampling method to speed up the process; however, a large number of trials may be needed in the case of more than five input variables [189]. Another common approach called "most probable point" (MPP) has also been used in several studies [188, 194, 195], and it can combine with different approximated performance functions to reduce the computational effort, such as advanced mean-value with iterations (AMV+) method [188]. Therefore, these advanced probabilistic methods can be examined and compared to the Monte Carlo method for the impact simulations.

Reference

1. Brunon, A., K. Bruyere-Garnier, and M. Coret, *Mechanical characterization of liver capsule through uniaxial quasi-static tensile tests until failure.* J Biomech, 2010. **43**(11): p. 2221-7.
2. Kemper, A.R., et al., *Biomechanical response of human liver in tensile loading.* Ann Adv Automot Med, 2010. **54**: p. 15-26.
3. Viano, D.C. *Biomechanical responses and injuries in blunt lateral impact*. in *SAE Technical Paper*. 1989.
4. Viano, D.C., et al., *Biomechanics of the human chest, abdomen, and pelvis in lateral impact.* Accident Analysis & Prevention, 1989. **21**(6): p. 553-574.
5. Lu, Y.-C., A.R. Kemper, and C.D. Untaroiu, *Effect of storage on tensile material properties of bovine liver.* Journal of the Mechanical Behavior of Biomedical Materials, 2014. **29**(0): p. 339-349.
6. Nguyen, N.H., et al., *Influence of a freeze-thaw cycle on the stress-stretch curves of tissues of porcine abdominal organs.* J Biomech, 2012. **45**(14): p. 2382-6.
7. Tamura, A., et al., *Mechanical characterization of porcine abdominal organs.* Stapp Car Crash J, 2002. **46**: p. 55-69.
8. Ocal, S., et al., *Effect of preservation period on the viscoelastic material properties of soft tissues with implications for liver transplantation.* J Biomech Eng, 2010. **132**(10): p. 101007.
9. Weaver, J.K., *The microscopic hardness of bone.* J Bone Joint Surg Am, 1966. **48**(2): p. 273-88.
10. Santago, A.C., et al., *Freezing affects the mechanical properties of bovine liver.* Biomed Sci Instrum, 2009. **45**: p. 24-9.
11. Arajarvi, E., S. Santavirta, and J. Tolonen, *Abdominal injuries sustained in severe traffic accidents by seatbelt wearers.* J Trauma, 1987. **27**(4): p. 393-7.
12. Cheynel, N., et al., *Abdominal and pelvic injuries caused by road traffic accidents: characteristics and outcomes in a French cohort of 2,009 casualties.* World J Surg, 2011. **35**(7): p. 1621-5.
13. Greingor, J.L. and S. Lazarus, *Chest and abdominal injuries caused by seat belt wearing.* South Med J, 2006. **99**(5): p. 534-5.
14. Klinich, K.D., et al., *Abdominal injury in motor-vehicle crashes*, in *University of Michigan Transportation Research Institute Technical Report*. 2008.
15. Brammer, R.D., et al., *A 10-year experience of complex liver trauma.* Br J Surg, 2002. **89**(12): p. 1532-7.
16. Elhagediab, A. and S. Rouhana, *Patterns of abdominal injury in frontal automotive crashes*, in *16th International Technical Conference on the Enhanced Safety of Vehicles*. 1998: Windsor, Ontario, Canada.
17. Cooper, A., et al., *Mortality and truncal injury: the pediatric perspective.* J Pediatr Surg, 1994. **29**(1): p. 33-8.
18. Bean, J.D., et al., *Fatalities in frontal crashes despite seat belts and air bags review of all CDS cases model and calendar years 2000-2007 122 fatalities*. 2009.
19. Lamielle, S., et al., *Abdominal injury patterns in real frontal crashes: influence of crash conditions, occupant seat and restraint systems.* Annu Proc Assoc Adv Automot Med, 2006. **50**: p. 109-24.
20. Melvin, J., et al., *Impact injury mechanisms in abdominal organs.* SAE Technical Paper, 1973. **730968**.
21. Oniscu, G.C., R.W. Parks, and O.J. Garden, *Classification of liver and pancreatic trauma.* HPB (Oxford), 2006. **8**(1): p. 4-9.
22. Nahum, A.M. and J.W. Melvin, *Accidental injury: biomechanics and prevention*. 2nd Edition ed. 2002: Springer.

23. Jin, W., et al., *Mechanisms of blunt liver trauma patterns: An analysis of 53 cases.* Exp Ther Med, 2013. **5**(2): p. 395-398.
24. Ahmed, I. and I.J. Beckingham, *Liver trauma.* Trauma, 2007. **9**(3): p. 171-180.
25. Howes, M.K., et al., *Kinematics of the thoracoabdominal contents under various loading scenarios.* Stapp car crash journal, 2012. **56**: p. 1-48.
26. Vavalle, N.A., et al., *Lateral impact validation of a geometrically accurate full body finite element model for blunt injury prediction.* Annals of Biomedical Engineering, 2013. **41**(3): p. 497-512.
27. Shin, J., N. Yue, and C.D. Untaroiu, *A finite element model of the foot and ankle for automotive impact applications.* Ann Biomed Eng, 2012. **40**(12): p. 2519-31.
28. Shin, J. and C. Untaroiu, *Biomechanical and Injury Response of Human Foot and Ankle under Complex Loading.* J Biomech Eng, 2013.
29. Mao, H., et al., *Development of a Finite Element Human Head Model Validated With Forty Nine Loading Cases From Experimental and Real World Impacts.* J Biomech Eng, 2013.
30. DeWit, J.A. and D.S. Cronin, *Cervical spine segment finite element model for traumatic injury prediction.* J Mech Behav Biomed Mater, 2012. **10**: p. 138-50.
31. Li, Z., et al., *Rib fractures under anterior-posterior dynamic loads: experimental and finite-element study.* J Biomech, 2010. **43**(2): p. 228-34.
32. Dar, F.H., J.R. Meakin, and R.M. Aspden, *Statistical methods in finite element analysis.* J Biomech, 2002. **35**(9): p. 1155-61.
33. Palmberg, B., A.F. Blom, and S. Eggwertz, *Probabilistic damage tolerance analysis of aircraft structures*, in *Probabilistic fracture mechanics and reliability*, J. Provan, Editor. 1987, Springer Netherlands. p. 47-130.
34. Melis, M.E., E.V. Zaretsky, and R. August, *Probabilistic analysis of aircraft gas turbine disk life and reliability.* J. Propul. Power, 1999. **15**(5): p. 658–666.
35. Zhang, Y. and Q. Liu, *Reliability-based design of automobile components.* Proc. Inst. Mech. Eng. Part D: J. Automob. Eng., 2002. **216**(6): p. 455–471.
36. Browne, M., R.S. Langley, and P.J. Gregson, *Reliability theory for load bearing biomedical implants.* Biomaterials, 1999. **20**(14): p. 1285-92.
37. Ng, H.W. and E.C. Teo, *Probabilistic design analysis of the influence of material property on the human cervical spine.* J Spinal Disord Tech, 2004. **17**(2): p. 123-33.
38. Nicolella, D.P., et al., *Probabilistic risk analysis of a cemented hip implant.* ASME Bioeng. Div., 2001. **50**: p. 427–428.
39. Nicolella, D.P., et al., *The effect of three-dimensional shape optimization on the probabilistic response of a cemented femoral hip prosthesis.* J Biomech, 2006. **39**(7): p. 1265-78.
40. Bah, M.T. and M. Browne, *Failure of the cement mantle in hip implants: a probabilistic approach*, in *Transactions of the 50th Annual Meeting of the Orthopaedic Research Society*. 2004. p. 1430.
41. Mehrez, L., M.T. Bah, and M. Browne, *The application of probabilistic methods for assessment of hip replacement integrity*, in *Transactions of the 51st Annual Meeting of the Orthopaedic Research Society*. 2005. p. 163.
42. Davies, R.H., C.J. Twining, and C.J. Taylor, *Statistical models of shape: optimisation and evaluation*. 2008: Springer Publishing Company, Incorporated.
43. Chen, J.-H. and L.G. Shapiro. *3D point correspondence by minimum description length with 2DPCA*. in *Engineering in Medicine and Biology Society, 2009. EMBC 2009. Annual International Conference of the IEEE*. 2009.
44. Barratt, D.C., et al., *Instantiation and registration of statistical shape models of the femur and pelvis using 3D ultrasound imaging.* Med Image Anal, 2008. **12**(3): p. 358-74.

45. Bredbenner, T.L., et al., *Statistical shape modeling describes variation in tibia and femur surface geometry between Control and Incidence groups from the osteoarthritis initiative database.* J Biomech, 2010. **43**(9): p. 1780-6.
46. van de Giessen, M., et al., *Statistical descriptions of scaphoid and lunate bone shapes.* J Biomech, 2010. **43**(8): p. 1463-9.
47. Okada, T., et al., *Automated Segmentation of the Liver from 3D CT Images Using Probabilistic Atlas and Multi-level Statistical Shape Model*, in *Medical Image Computing and Computer-Assisted Intervention – MICCAI 2007*, N. Ayache, S. Ourselin, and A. Maeder, Editors. 2007, Springer Berlin Heidelberg. p. 86-93.
48. Reyes, M., et al., *Hierarchical patch generation for multilevel statistical shape analysis by principal factor analysis decomposition.* 2010: p. 762617-762617.
49. Untaroiu, C.D., et al., *Effect of seat belt pretensioners on human abdomen and thorax: biomechanical response and risk of injuries.* J Trauma Acute Care Surg, 2012. **72**(5): p. 1304-15.
50. Lu, Y.-C. and C.D. Untaroiu, *Statistical shape analysis of clavicular cortical bone.* Computer Methods and Programs in Biomedicine, 2013. **111**(3): p. 613-28.
51. Davies, R.H., et al., *Building 3-D statistical shape models by direct optimization.* Medical Imaging, IEEE Transactions on, 2010. **29**(4): p. 961-981.
52. Lamecker, H., T. Lange, and M. Seebass, *A statistical shape model for the liver*, in *Proceedings of the 5th International Conference on Medical Image Computing and Computer-Assisted Intervention-Part II* 2002. p. 421-427.
53. Dryden, I.L. and K.V. Mardia, *Statistical shape analysis*. 1 ed. 1998: John Wiley & Sons, Inc.
54. Fink, W.L. and M.L. Zelditch, *Shape analysis and taxonomic status of Pygocentrus piranhas (Ostariophysi, Characiformes) from the Paraguay and Paraná river basins of South America.* Copeia 1997. **1**: p. 179-182.
55. Bhatia, K.K., et al. *Consistent groupwise non-rigid registration for atlas construction*. in *Biomedical Imaging: Nano to Macro, 2004. IEEE International Symposium on*. 2004.
56. Lamecker, H., T.H. Wenckebach, and H.C. Hege. *Atlas-based 3D-shape reconstruction from X-ray images*. in *Pattern Recognition, 2006. ICPR 2006. 18th International Conference on*. 2006.
57. Brett, A.D. and C.J. Taylor, *A method of automated landmark generation for automated 3D PDM construction.* Image and Vision Computing, 2000. **18**(9): p. 739-748.
58. Davies, R.H., *Learning shape: optimal models for analysing natural variability*. 2002, University ofManchester.
59. Fleute, M., S. Lavallée, and R. Julliard, *Incorporating a statistically based shape model into a system for computer-assisted anterior cruciate ligament surgery.* Medical Image Analysis, 1999. **3**(3): p. 209-222.
60. Hufnagel, H., et al., *Computation of a probabilistic statistical shape model in a maximum-a-posteriori framework.* Methods Inf Med, 2009. **48**(4): p. 314-9.
61. Marai, G.E., C.M. Grimm, and D.H. Laidlaw, *Arthrodial Joint Markerless Cross-Parameterization and Biomechanical Visualization.* Visualization and Computer Graphics, IEEE Transactions on, 2007. **13**(5): p. 1095-1104.
62. Rajamani, K.T., et al., *Statistical deformable bone models for robust 3D surface extrapolation from sparse data.* Med Image Anal, 2007. **11**(2): p. 99-109.
63. Heimann, T. and H.-P. Meinzer, *Statistical shape models for 3D medical image segmentation: a review.* Medical Image Analysis, 2009. **13**(4): p. 543-563.
64. Chen, J.-H., K.C. Zheng, and L.G. Shapiro, *3D point correspondence by minimum description length in feature space*, in *Proceedings of the 11th European conference on computer vision*

conference on Computer vision: Part III. 2010, Springer-Verlag: Heraklion, Crete, Greece. p. 621-634.
65. Fripp, J., et al., *3D Statistical shape models to embed spatial relationship information*, in *Proceedings of the 1st International Workshop on Computer Vision for Biomedical Image Applications*. 2005. p. 51-60.
66. Lorenz, C. and N. Krahnstover. *3D statistical shape models for medical image segmentation*. in *3-D Digital Imaging and Modeling, 1999. Proceedings. Second International Conference on*. 1999.
67. Azouz, Z.B., et al., *Characterizing human shape variation using 3D anthropometric data.* Vis. Comput., 2006. **22**(5): p. 302-314.
68. Xi, P., W.-S. Lee, and C. Shu, *Analysis of segmented human body scans*, in *Proceedings of Graphics Interface 2007*. 2007, ACM: Montreal, Canada. p. 19-26.
69. Dalal, P., et al. *A fast 3D correspondence method for statistical shape modeling*. in *Computer Vision and Pattern Recognition, 2007. CVPR '07. IEEE Conference on*. 2007.
70. Beillas, P., Y. Lafon, and F.W. Smith, *The effects of posture and subject-to-subject variations on the position, shape and volume of abdominal and thoracic organs.* Stapp Car Crash J, 2009. **53**: p. 127-54.
71. Hayes, A.R., et al., *Comparison of organ location, morphology, and rib coverage of a midsized male in the supine and seated positions.* Comput Math Methods Med, 2013. **2013**: p. 419821.
72. Styner, M.A., et al., *Evaluation of 3D correspondence methods for model building.* Information processing in medical imaging : proceedings of the ... conference, 2003. **18**: p. 63-75.
73. He, Q., et al., *Detecting 3D corpus callosum abnormalities in phenylketonuria.* Int J Comput Biol Drug Des, 2009. **2**(4): p. 289-301.
74. He, Q., et al., *Detecting corpus callosum abnormalities in autism based on anatomical landmarks.* Psychiatry Res, 2010. **183**(2): p. 126-32.
75. van de Giessen, M., et al. *A statistical description of the articulating ulna surface for prosthesis design*. in *Biomedical Imaging: From Nano to Macro, 2009. ISBI '09. IEEE International Symposium on*. 2009.
76. Belongie, S., J. Malik, and J. Puzicha, *Shape matching and object recognition using shape contexts.* Pattern Analysis and Machine Intelligence, IEEE Transactions on, 2002. **24**(4): p. 509-522.
77. Bookstein, F.L., *Principal warps: thin-plate splines and the decomposition of deformations.* Pattern Analysis and Machine Intelligence, IEEE Transactions on, 1989. **11**(6): p. 567-585.
78. Hayes, A.R., et al., *Abdominal organ location, morphology, and rib coverage for the 5th, 50th, and 95th percentile males and females in the supine and seated posture using multi-modality imaging*, in *Ann Avd Automot Med.* 2013: Quebec City, Canada.
79. Besl, P.J. and H.D. McKay, *A method for registration of 3-D shapes.* Pattern Analysis and Machine Intelligence, IEEE Transactions on, 1992. **14**(2): p. 239-256.
80. Zhang, Z.Y. *On Local Matching of Free-Form Curves*. 1992.
81. Fitzgibbon, A.W., *Robust registration of 2D and 3D point sets.* Image and Vision Computing, 2003. **21**(13–14): p. 1145-1153.
82. Zheng, G., et al., *A 2D/3D correspondence building method for reconstruction of a patient-specific 3D bone surface model using point distribution models and calibrated X-ray images.* Med Image Anal, 2009. **13**(6): p. 883-99.
83. Munsell, B.C., P. Dalal, and W. Song, *Evaluating shape correspondence for statistical shape analysis: a benchmark study.* IEEE Transactions on Pattern Analysis and Machine Intelligence, 2008. **30**(11): p. 2023-2039.

84. Daruwalla, Z.J., et al., *Anatomic variation of the clavicle: a novel three-dimensional study.* Clin Anat, 2010. **23**(2): p. 199-209.
85. Untaroiu, C.D., et al., *A study of the pedestrian impact kinematics using finite element dummy models: the corridors and dimensional analysis scaling of upper-body trajectories.* International Journal of Crashworthiness, 2008. **13**(5): p. 469-478.
86. Lu, Y.-C., et al., *Statistical modeling of human liver incorporating the variations in shape, size, and material properties.* Stapp Car Crash J, 2013. **57**: p. 285-311.
87. Reed, M.P., et al., *Anthropometric specification of child crash dummy pelves through statistical analysis of skeletal geometry.* Journal of Biomechanics, 2009. **42**(8): p. 1143-1145.
88. Untaroiu, C.D. and Y.-C. Lu, *Material characterization of liver parenchyma using specimen-specific finite element models.* Journal of the Mechanical Behavior of Biomedical Materials, 2013. **26**: p. 11-22.
89. Lessley, D., et al., *A normalization technique for developing corridors from individual subject responses.* SAE Technical Paper, 2004. **2004-01-0288**.
90. Kohara, S., et al. *Application of statistical shape model to diagnosis of liver disease*. in *Software Engineering and Data Mining (SEDM), 2010 2nd International Conference on*. 2010.
91. Choukèr, A., et al., *Estimation of liver size for liver transplantation: the impact of age and gender.* Liver Transpl Surg, 2004. **10**(5): p. 678-85.
92. Heinemann, A., et al., *Standard liver volume in the Caucasian population.* Liver Transpl Surg, 1999. **5**(5): p. 366-8.
93. Vauthey, J.N., et al., *Body surface area and body weight predict total liver volume in Western adults.* Liver Transpl Surg, 2002. **8**(3): p. 233-40.
94. Vezin, P. and J.P. Verriest, *Development of a set of numerical human models for safety*, in *Proceedings of the 19th International Technical Conference on the Enhanced Safety of Vehicles*. 2005.
95. Gayzik, F.S., et al., *Development of a full body CAD dataset for computational modeling: a multi-modality approach.* Ann Biomed Eng, 2011. **39**(10): p. 2568-83.
96. Untaroiu, C.D., et al., *Experimental and computational investigation of human clavicle response in anterior-posterior bending loading - biomed 2009.* Biomed Sci Instrum, 2009. **45**: p. 6-11.
97. Untaroiu, C.D., N. Yue, and J. Shin, *A finite element model of the lower limb for simulating automotive impacts.* Ann Biomed Eng, 2013. **41**(3): p. 513-26.
98. Wuhrer, S., C. Shu, and P. Xi, *Landmark-free posture invariant human shape correspondence.* Vis. Comput., 2011. **27**(9): p. 843-852.
99. Laz, P.J. and M. Browne, *A review of probabilistic analysis in orthopaedic biomechanics.* Proc Inst Mech Eng H, 2010. **224**(8): p. 927-43.
100. Untaroiu, C.D., *A numerical investigation of mid-femoral injury tolerance in axial compression and bending loading.* Int. J. Crashworthiness 2010. **15**(1): p. 83-92.
101. Rouhana, S.W., R.E. El-Jawahri, and T.R. Laituri, *Biomechanical considerations for abdominal loading by seat belt pretensioners.* Stapp Car Crash Journal, 2010. **54**: p. 381-406.
102. Crandall, J.R., et al., *Human surrogates for injury biomechanics research.* Clinical Anatomy, 2011. **24**(3): p. 362-371.
103. Chui, C., et al., *Transversely isotropic properties of porcine liver tissue: experiments and constitutive modelling.* Med Biol Eng Comput, 2007. **45**(1): p. 99-106.
104. Kemper, A.R., et al., *Biomechanical response of human spleen in tensile loading.* J Biomech, 2012. **45**(2): p. 348-55.
105. Snedeker, J.G., et al., *Strain-rate dependent material properties of the porcine and human kidney capsule.* J Biomech, 2005. **38**(5): p. 1011-21.

106. Snedeker, J.G., et al., *Strain energy density as a rupture criterion for the kidney: impact tests on porcine organs, finite element simulation, and a baseline comparison between human and porcine tissues.* J Biomech, 2005. **38**(5): p. 993-1001.
107. Crandall, J.R., et al., *A review of human surrogates for injury biomechanics research.* Clinical Anatomy, 2011. **24**(3): p. 362-371.
108. Eichberger, A., et al., *Pressure measurements in the spinal canal of post-mortem human subjects during rear-end impact and correlation of results to the neck injury criterion.* Accid Anal Prev, 2000. **32**(2): p. 251-60.
109. McIntosh, A.S., D. Kallieris, and B. Frechede, *Neck injury tolerance under inertial loads in side impacts.* Accid Anal Prev, 2007. **39**(2): p. 326-33.
110. Salzar, R.S., et al., *Viscoelastic Response of the Thorax under Dynamic Belt Loading.* Traffic Injury Prevention, 2009. **10**(3): p. 290-296.
111. Crandall, J.R., *Preservation of human surrogates for impact studies*, in *Mechanical and Aerospace Engineering*. 1994, University of Virginia.
112. Griffon, D.F., L.F. Wallace, and J.E. Bechtold, *Biomechanical properties of canine corticocancellous bone frozen in normal saline solution.* Am J Vet Res., 1995. **56**(6): p. 822-5.
113. Sedlin, E.D., *A rheological model for cortical bone.* Acta Orthop. Scand., 1965. **83**(1).
114. Linde, F. and H.C. Sorensen, *The effect of different storage methods on the mechanical properties of trabecular bone.* J Biomech, 1993. **26**(10): p. 1249-52.
115. Frankel, V.H., *The Femoral Neck; Function, Fracture Mechanism, Internal Fixation: An Experimental Study*. 1960: Thomas.
116. Hamer, A.J., et al., *Biomechanical properties of cortical allograft bone using a new method of bone strength measurement: a comparison of fresh, fresh-frozen and irradiated bone.* Journal of Bone & Joint Surgery, British Volume, 1996. **78-B**(3): p. 363-368.
117. Smeathers, J.E. and D.N. Joanes, *Dynamic compressive properties of human lumbar intervertebral joints: A comparison between fresh and thawed specimens.* Journal of Biomechanics, 1988. **21**(5): p. 425-433.
118. Woo, S.L., et al., *Effects of postmortem storage by freezing on ligament tensile behavior.* J Biomech, 1986. **19**(5): p. 399-404.
119. Hollenstein, M., et al., *Mechanical characterization of the liver capsule and parenchyma*, in *Biomedical Simulation*, M. Harders and G. Székely, Editors. 2006, Springer Berlin Heidelberg. p. 150-158.
120. Mattice, J., et al., *Spherical indentation load-relaxation of soft biological tissues.* Journal of Materials Research, 2006. **21**(8): p. 2003-2010.
121. Davies, P.J., et al., *Mathematical modelling for keyhole surgery simulations: spleen capsule as an elastic membrabe.* Journal of Theoretical Medicine, 1999. **1**(4): p. 247-262.
122. Shafieian, M., K.K. Darvish, and J.R. Stone, *Changes to the viscoelastic properties of brain tissue after traumatic axonal injury.* Journal of Biomechanics, 2009. **42**(13): p. 2136-2142.
123. Fung, Y.C., *Biomechanics: mechanical properties of living tissues*. 2nd edition ed. 1993: Springer.
124. Troyer, K.L., D.J. Estep, and C.M. Puttlitz, *Viscoelastic effects during loading play an integral role in soft tissue mechanics.* Acta Biomaterialia, 2012. **8**(1): p. 234-243.
125. Coleman, T., *MATLAB Optimization Toolbox User's Guide*. R2011b ed. 2011, Natick, MA: The MathWorks, Inc.
126. Milton, J.S. and J. Arnold, *Introduction to Probability and Statistics: Principles and Applications for Engineering and the Computing Sciences*. 4th Edition ed. 2002: McGraw-Hill Science/Engineering/Math.

127. Fitzmaurice, G.M., N.M. Laird, and J.H. Ware, *Applied longitudinal analysis*. 2nd Edition ed. 2004: John Wiley and Sons.
128. Lu, Y.-C. and C.D. Untaroiu, *Effect of storage methods on indentation-based material properties of abdominal organs.* Proceedings of the Institution of Mechanical Engineers, Part H: Journal of Engineering in Medicine, 2013. **227**(3): p. 293-301.
129. Hu, J., et al., *Quantifying dynamic mechanical properties of human placenta tissue using optimization techniques with specimen-specific finite-element models.* J Biomech, 2009. **42**(15): p. 2528-34.
130. Hu, J., et al., *A stochastic visco-hyperelastic model of human placenta tissue for finite element crash simulations.* Ann Biomed Eng, 2011. **39**(3): p. 1074-83.
131. Nava, A., et al., *In vivo mechanical characterization of human liver.* Med Image Anal, 2008. **12**(2): p. 203-16.
132. Holzapfel, G.A., *Nonlinear solid mechanics: a continuum approach for engineering*. 1st Edition ed. 2000, Chichester, UK: Wiley.
133. Ogden, R.W., *Non-linear elastic deformations*. 1997, Mineola, NY: Dover Publications.
134. Klinich, K.D., et al., *Characterization of ovine utero-placental interface tensile failure.* Placenta, 2012. **33**(10): p. 776-81.
135. Gill, W. and J. Fraser, *A look at cryosurgery.* Scott Med J, 1968. **13**(8): p. 268-73.
136. Whittaker, D.K., *Mechanisms of tissue destruction following cryosurgery.* Ann R Coll Surg Engl, 1984. **66**(5): p. 313-8.
137. Mazur, P., *The role of intracellular freezing in the death of cells cooled at supraoptimal rates.* Cryobiology, 1977. **14**(3): p. 251-272.
138. Farrant, J. and C.A. Walter, *The cryobiological basis for cryosurgery.* J Dermatol Surg Oncol, 1977. **3**(4): p. 403-7.
139. Jacob, G., M.N. Kurzer, and B.J. Fuller, *An assessment of tumor cell viability after in vitro freezing.* Cryobiology, 1985. **22**(5): p. 417-26.
140. Shier, W.T., *Studies on the mechanisms of mammalian cell killing by a freeze-thaw cycle: conditions that prevent cell killing using nucleated freezing.* Cryobiology, 1988. **25**(2): p. 110-20.
141. Ahn, B. and J. Kim. *An efficient soft tissue characterization method for haptic rendering of soft tissue deformation in medical simulation*. in *Frontiers in the Convergence of Bioscience and Information Technologies, 2007. FBIT 2007*. 2007.
142. Carter, F., et al., *Restructured animal tissue model for training in laparoscopic anti-reflux surgery.* Minim Invasiv Ther, 1994. **3**(2): p. 77-80.
143. Vodicka, P., et al., *The Miniature Pig as an Animal Model in Biomedical Research.* Annals of the New York Academy of Sciences, 2005. **1049**(1): p. 161-171.
144. Farshad, M., et al., *Material characterization of the pig kidney in relation with the biomechanical analysis of renal trauma.* J Biomech, 1999. **32**(4): p. 417-25.
145. Bass, C.R., et al., *The temperature-dependent viscoelasticity of porcine lumbar spine ligaments.* Spine (Phila Pa 1976), 2007. **32**(16): p. E436-42.
146. Gao, Z., K. Lister, and J.P. Desai, *Constitutive modeling of liver tissue: experiment and theory.* Ann Biomed Eng, 2010. **38**(2): p. 505-16.
147. Seki, S. and H. Iwamoto, *Disruptive forces for swine heart, liver, and spleen: their breaking stresses.* The Journal of Trauma and Acute Care Surgery, 1998. **45**(6): p. 1079-1083.
148. Ross, M.H. and W. Pawlina, *Histology: A Text and Atlas: With Correlated Cell and Molecular Biology*. 5th Edition ed. 2006, Baltimore: Lippincott Williams and Wilkins.
149. Zhang, S.-X., *An Atlas of Histology*. 1999, New York: Springer.
150. Matthews, J., *Atlas of human histology and ultrastructure*. 1971, Philadelphia: Lea and Febiger.

151. Eurell, J.A. and B.L. Frappier, *Dellmann's Textbook of Veterinary Histology*. 6th Edition ed. 2006, Publishing: Wiley-Blackwell.
152. Pervin, F., W.W. Chen, and T. Weerasooriya, *Dynamic compressive response of bovine liver tissues.* J Mech Behav Biomed Mater, 2011. **4**(1): p. 76-84.
153. Manoogian, S.J., et al., *Effect of strain rate on the tensile material properties of human placenta.* J Biomech Eng, 2009. **131**(9): p. 091008.
154. Hallquist, J.O., *LS-DYNA keyword user's manual*. 2007: Livermore, California.
155. Huwart, L., et al., *Liver fibrosis: non-invasive assessment with MR elastography.* NMR in Biomedicine, 2006. **19**(2): p. 173-179.
156. Rouvière, O., et al., *MR elastography of the liver: preliminary results.* Radiology, 2006. **240**(2): p. 440-8.
157. Bercoff, J., M. Tanter, and M. Fink, *Supersonic shear imaging: a new technique for soft tissue elasticity mapping.* IEEE Trans Ultrason Ferroelectr Freq Control, 2004. **51**(4): p. 396-409.
158. Rosen, J., et al., *Biomechanical properties of abdominal organs in vivo and postmortem under compression loads.* J Biomech Eng, 2008. **130**(2): p. 021020.
159. Kemper, A.R., et al., *Effect of strain rate on the material properties of human liver parenchyma in unconfined compression.* J Biomech Eng, 2013.
160. Yeh, W.-C., et al., *Elastic modulus measurements of human liver and correlation with pathology.* Ultrasound in Medicine & Biology, 2002. **28**(4): p. 467-474.
161. Gao, Z. and J.P. Desai, *Estimating zero-strain states of very soft tissue under gravity loading using digital image correlation.* Medical Image Analysis, 2010. **14**(2): p. 126-137.
162. Yamada, H., *Strength of biological materials*. 1970, Huntingdon, NY: Williams and Wilkins.
163. Uehara, H., *A study on the mechanical properties of the kidney, liver, and spleen, by means of tensile stress test with variable strain velocity.* Journal of Kyoto Prefectural University of Medicine, 1995. **104**(1): p. 439-451.
164. Santago, A.C., et al., *The effect of temperature on the mechanical properties of bovine liver.* Biomed Sci Instrum, 2009. **45**: p. 376-81.
165. Liu, Z. and L. Bilston, *On the viscoelastic character of liver tissue: experiments and modelling of the linear behaviour.* Biorheology, 2000. **37**(3): p. 191-201.
166. Valtorta, D. and E. Mazza, *Dynamic measurement of soft tissue viscoelastic properties with a torsional resonator device.* Med Image Anal, 2005. **9**(5): p. 481-90.
167. Klatt, D., et al., *Viscoelastic properties of liver measured by oscillatory rheometry and multifrequency magnetic resonance elastography.* Biorheology, 2010. **47**(2): p. 133-41.
168. Nicolle, S., P. Vezin, and J.F. Palierne, *A strain-hardening bi-power law for the nonlinear behaviour of biological soft tissues.* J Biomech, 2010. **43**(5): p. 927-32.
169. Umut Ozcan, M., et al., *Characterization of frequency-dependent material properties of human liver and its pathologies using an impact hammer.* Med Image Anal, 2011. **15**(1): p. 45-52.
170. Ottensmeyer, M.P., *Minimally invasive instrument for in vivo measurement of solid organ mechanical impedance*, in *Department of Mechanical Engineering*. 2001, Massachusetts Institute of Technology: Cambridge, MA.
171. Samur, E., et al., *A robotic indenter for minimally invasive measurement and characterization of soft tissue response.* Med Image Anal, 2007. **11**(4): p. 361-73.
172. Tallarida, R.J. and R.B. Murray, *Mann-Whitney Test*, in *Manual of Pharmacologic Calculations*. 1986, Springer New York. p. 149-153.
173. Rainsberger, R., *TrueGrid User's Manual*. 2006.
174. Kolling, S., et al., *A tabulated formulation of hyperelasticity with rate effects and damage.* Computational Mechanics, 2007. **40**(5): p. 885-899.

175. Untaroiu, C.D., *The influence of the specimen shape and loading conditions on the parameter identification of a viscoelastic brain model.* Computational and Mathematical Methods in Medicine, 2013. **2013**.
176. Untaroiu, C.D., *Development and validation of a finite element model of human lower limb: including detailed geometry, physical material properties, and component validations for pedestrian injuries*. 2005, University of Virginia.
177. Geißler, G., C. Netzker, and M. Kaliske, *Discrete crack path prediction by an adaptive cohesive crack model.* Engineering Fracture Mechanics, 2010. **77**(18): p. 3541-3557.
178. Gokgol, C., C. Basdogan, and D. Canadinc, *Estimation of fracture toughness of liver tissue: Experiments and validation.* Medical Engineering & Physics, 2012. **34**(7): p. 882-891.
179. Menk, A. and S.P.A. Bordas, *Numerically determined enrichment functions for the extended finite element method and applications to bi-material anisotropic fracture and polycrystals.* International Journal for Numerical Methods in Engineering, 2010. **83**(7): p. 805-828.
180. Pannachet, T., L.J. Sluys, and H. Askes, *Error estimation and adaptivity for discontinuous failure.* International Journal for Numerical Methods in Engineering, 2009. **78**(5): p. 528-563.
181. Volokh, K.Y., *On modeling failure of rubber-like materials.* Mechanics Research Communications, 2010. **37**(8): p. 684-689.
182. Adam, T. and C.D. Untaroiu, *Identification of occupant posture using a Bayesian classification methodology to reduce the risk of injury in a collision.* Transportation Research Part C: Emerging Technologies, 2011. **19**(6): p. 1078-1094.
183. Untaroiu, C.D. and T.J. Adam, *Performance-Based Classification of Occupant Posture to Reduce the Risk of Injury in a Collision.* Intelligent Transportation Systems, IEEE Transactions on, 2013. **14**(2): p. 565-573.
184. Kerdok, A.E., M.P. Ottensmeyer, and R.D. Howe, *Effects of perfusion on the viscoelastic characteristics of liver.* Journal of Biomechanics, 2006. **39**(12): p. 2221-2231.
185. Iwamoto, M., et al., *Development of Advanced Human Models in THUMS*, in *6th European LS-DYNA Users' Conference*. 2010. p. 47-56.
186. Maeno, T. and J. Hasegawa, *Development of a Finite Element Model of the Total Human Model for Safety (THUMS) and Application to Car-Pedestrian Impacts.* SAE Technical Paper, 2001. **2001-06-0054**.
187. Watanabe, R., et al., *Research of collision speed dependency of pedestrian head and chest injuries using human FE model (THUMS version 4).* Accident Reconstruction Journal, 2012. **22**(1): p. 31-40.
188. Easley, S.K., et al., *Finite element-based probabilistic analysis tool for orthopaedic applications.* Comput Methods Programs Biomed, 2007. **85**(1): p. 32-40.
189. Stander, N., et al., *LS-OPT user's manual*, in *A design optimization and probabilistic analysis tool for the engineering analyst*. 2012: Livermore, California.
190. Vavalle, N.A., et al., *The effect of impactor location and velocity variation on validation of an advanced human body finite element model.* Biomed Sci Instrum, 2012. **48**: p. 454-61.
191. Lu, Y.-C. and C.D. Untaroiu, *A bootstrap approach for lower injury levels of the risk curves.* Computer Methods and Programs in Biomedicine, 2012. **106**(3): p. 274-286.
192. Harbrecht, B.G., et al., *Contribution of age and gender to outcome of blunt splenic injury in adults: multicenter study of the eastern association for the surgery of trauma.* J Trauma, 2001. **51**(5): p. 887-95.
193. Nasseri, S., L.E. Bilston, and N. Phan-Thien, *Viscoelastic properties of pig kidney in shear, experimental results and modelling.* Rheologica Acta, 2002. **41**(1): p. 180-192.
194. Melchers, R.E., *Structural Reliability Analysis and Prediction*. 2nd edition ed. 1999: Wiley.

195. Wu, Y.-T., H.R. Millwater, and T.A. Cruse, *An advanced probabilistic structural analysis method for implicit performance functions.* AiAA J., 1989. **28**(9): p. 1663-1669.